BRITISH GEOLOGICAL SURVEY

TECHNICAL REPORT WM/89/15

Geomagnetism Series

TECHNICAL REPORT WM/89/15

TECHNICAL REPORT WM/89/15

AN AUDIOMAGNETOTELLURIC SURVEY OF THE CARNMENELLIS GRANITE

D. Beamish and J.C. Riddick

Subject index

Geoelectric, geothermal, hot dry rock, granite.

British Geological Survey, Edinburgh, 1989

WR/89/15

9/2/96 1 LIO

CONTENTS

1. EXECUTIVE SUMMARY.

The electrical resistivity of competent/unfractured rock depends mainly on porosity and the conductivity of the pore fluid. In fractured/jointed rocks a further degree of dependence on the degree of fluid saturation and permeability is observed. The audiomagnetotelluric survey described in this report is primarily concerned with mapping resistivity variations (i.e. rock/fluid properties) through the critical depth range (2 to 8 km) of geothermal energy extraction within and across the Carnmenellis granite.

This report describes the audiomagnetotelluric experiment that was carried out during 1988. Two field surveys were performed. A main survey to assess the presence of a refractor (a wide-angle reflector) at about 7 to 8 km (Brooks et al., 1984) and a secondary survey to assess the depth extent of a surface lineament. The principal results of the field experiment are now summarised.

A seven-site investigation of a NW-SE surface lineament was carried out at spacings of 50m. To our knowledge, this is the first audiomagnetotelluric experiment involving such small spacings. The survey data were partially marred by an additive noise component in one of the electric field channels. Subsequent detailed analysis of these data revealed electric fence noise as the cause. Although such hindsight detection is unfortunate, the uncontaminated data offer valid constraints in relation to the detection of a fluid-filled fracture zone. The results presented indicate that it is highly unlikely that the target lineament can be associated with a conductive zone possessing a reasonable resistivity contrast which intersects the surface or near-surface. The results of the main experiment extend this null interpretation to the majority of surface lineaments as described below.

The main granite survey consisted of 17 soundings in total. An E-W profile across the granite outcrop comprised 12 soundings and two further soundings were conducted off the outcrop for control. The two off-granite soundings provided very different 'dimensional' characteristics to soundings on the granite. They therefore confirm the broad homogeneity of the geoelectric anisotropy on the granite. The two off-granite soundings also provided information on the resistivities of the Devonian cover rocks and the depth to granite. A further 3 soundings were performed in the vicinity of the Hot Dry Rock (HDR) reservoir at Rosemanowes quarry.

Overall the Carnmenellis granite, as defined by its broad resistivity characteristics, appears predominantly homogeneous. A very consistent set of resistivity values are found for the whole granite structure below depths of 2 km. The majority of resistivity values are in the range 1000 to 10,000 ohm.m. When laboratory analyses of thermal and pressure dependence are taken into account the granite is found to correspond to a 'wet' granite saturated with several weight-percent of free water down to at least 10 km. The consistency of the resistivity values below 2 km across a major portion of the granite indicates that lateral geoelectric effects are likely to be confined to the near-surface (i.e. < 2 km). An examination of the lateral anisotropic behaviour

across the granite confirms this general conclusion. We conclude that with the exception of one location the surface lineations, within the area surveyed, do not appear to represent deep vertical or sub-vertical zones with rock/fluid properties that would distinguish them from 'background' properties.

Judging by the hydrogeological models for the near-surface granite, a spatially-complex hydrothermal circulation system can be considered to operate at depth (Gregory and Durrance 1987). The spatial distribution of such a system is likely to be closely tied to the distribution of major water-conducting fractures. Although the scale and degree of resistivity contrasts should be considered, the main survey profile has detected only *one* such near-surface feature. Significantly this conductive zone is spatially localised and is directed NE-SW. The zone appears to be correlated with a lineament and a main arterial alluvial fan of the survey region. The E-W survey profile intersects the NE-SW trending zone 0.5 km directly south of the village of Porkellis. There is an indication of a conductive layer at a depth of 1 km in the vicinity of this lineament.

The sites defining the SE portion of the granite display anisotropic features which are different from those to the west. It is suggested that the cause is associated with boundary or off-granite variations rather than with variations across the outcrop although this cannot be ruled out. The features observed in the SE appear to define a broad, large-scale effect. Resistivity values through the granite also appear slightly larger in this region of the outcrop.

The lateral geoelectric anisotropy transfers (i.e. azimuths rotate) from local and near-surface penetrations (e.g. 1 to 2 km) to a regional scale anisotropy at large-volume penetrations (e.g. in excess of 25 km). The rotation pattern is consistent at the majority of survey locations beginning NE/ENE at depths of about 1 km to N/NE at depths of 6 to 10 km and thence to NW/N at depths in excess of 25 km. The information on geoelectric anisotropy has been compared with the principal joint and stress directions of the granite in order to identify the mechanism controlling the resistivity variations. The main conclusion is that the directions of resistivity anisotropy do not display any persistent alignment with the principal horizontal stress directions. Such a conclusion assumes that the present indicators of stress directions are representative of the *in situ* stress at depths in excess of 2.5 km. On this basis then the mechanism of aligned microcracks does not appear to control the observed geoelectric anisotropy. The results indicate that within the upper 1.5 km (at least), resistivity is controlled by one of the two principal joint systems of the granite. The results identify the fracture system parallel to the NW-SE master joints as being preferentially 'open' and containing enhanced concentrations of fluids. A definitive interpretation (from geoelectric anisotropy) at greater depths appears to be restricted by the observed 'intermediate' rotations as other larger-scale (regional) effects become more dominant. The vertical field is, however, influenced by a major resistivity contrast striking NW-SE beyond, and to the SW, of the Carnmenellis outcrop.

Below a depth of 2 km resistivity values increase slowly with depth attaining maximum values by

about 6 km. The anticipated linear *decrease* of resistivity with increasing temperature is not observed and a more dominant pressure/stress dependence must control the spatially-consistent, depth dependence observed. Laboratory measurements on a wide range of granitic rocks indicate that transfer from crack-dominated behaviour to pore-dominated behaviour will be complete by an applied pressure of 200 MPa. The extrapolated overburden and stress magnitudes, from the HDR borehole measurements, suggest that this will be achieved within the Carnmenellis by about 6 km. The resistivity profiles are therefore consistent with the completion of crack closure by a depth of 6 km and a transfer to a pore-dominated resistivity mechanism below this depth. Thus, in simple terms, if a 'joint' can be defined as a feature that is capable of 'closing' (and closed here means an inability to support ionic conduction of interstitial fluids) the observations suggest the absence of such joints below 6 km.

A comparison of the vertical geoelectric profiles across the granite with the boundary reflector (R1) of the deep low-velocity zone modelled by Brooks et al. (1984) is possible. The resistivity profiles however do not reveal any spatially-consistent major discontinuities in the upper 12 km. The depth interval of the low-velocity zone appears merely to be associated with an interval of approximately constant and maximum resistivity. We conclude that no detectable geoelectric variations in rock/fluid properties can be identified at a depth associated with the R1 reflector. Thus R1 does not appear to represent the upper surface of a fractured zone with an associated enhancement of conducting fluids.

The three sounding sites above and around the HDR reservoir provide interesting results in the upper 5 km. The identical resistivity profiles at two of the sites display a more conductive profile when compared with a third site some 1.1 km away. The two sites, 500 m apart, appear to define a 'reservoir-influenced' section down to depths of 4 to 5 km. This depth appears consistent with the termination depth of the microseismic zone defined during hydrofracturing. The finite lateral extent of the low-resistivity reservoir volume is also apparent in the azimuthal (anisotropic) behaviour across the three locations. Thus the zone of enhanced fluid concentration (i.e. the reservoir) has been shown to have finite dimensions both laterally and vertically.

2. INTRODUCTION.

Although there is considerable geological and geophysical background to consider in relation to the Carnmenellis granite, no attempt is made here to review the literature. Only brief references are made in the text to related findings. The summary plot of the depth to granite, provided by Camborne School of Mines (CSM), is shown for reference in Figure 2.1. The summary geophysical N-S section through the granite, again provided by CSM, is shown in Figure 2.2. It should be noted that when the text refers to 'on-granite', we simply refer to surface outcrop as defined in these two figures.

The three broad objectives of the project were (a) to provide information on the extent to which

the granite can be considered homogeneous in terms of its rock/fluid properties with depth and, in particular, to identify the nature of the seismic refractor (R1) at a depth of 7 to 8 km. (b) to investigate the behaviour of the prevailing geoelectric anisotropy at points along an E-W profile and with depth and (c) to provide a detailed investigation of a target surface lineament to test the hypothesis that such a feature represents a thin conductive zone that persists to deeper crustal levels.

Two-dimensional modelling was carried out on a number of 'type' structures prior to and following the field experiment. The primary concern was to identify the magnetotelluric response of vertical and sub-vertical 'thin' conducting zones. The results are described in Appendix B. A more limited 2-D model study of the whole Carnmenellis structure is described in Appendix C. It should be noted that no attempt has been made to provide 2-D models for the *results* obtained. Interpretation in the text is by way of reference to 'type' behaviour.

Descriptions of both the main, E-W granite survey (17 full-bandwidth soundings) and the lineament survey (7 high-frequency soundings) are provided in section 3. Three sets of site codes, prefixed with 1, 2 and 3, have been introduced to simplify spatial identification. Data quality is also considered and because electric fence noise was a feature of the field experiment this aspect of data quality is addressed as a special topic in Appendix A.

The results of the lineament survey are considered separately in section 4. The main set of results for the granite survey are considered in section 5. To assist in the interpretation of the results we have transformed frequency (the conventional display parameter) to an equivalent, 'one-dimensional' depth scale. Because of the 3-D nature of the sounding technique section 5 attempts to separate results related to one-dimensionality (the vertical resistivity profile) from the two-dimensional azimuthal information related to lateral geoelectric anisotropy. The lateral interpretation parameters largely consist of azimuths, although magnitudes must also be considered. The azimuths are presented spatially and as functions of the penetration radius (frequency). Both magnetotelluric and vertical magnetic field parameters are considered. An important aspect of the results related to the vertical resistivity profile is the consideration given to two types of parameter space. Much conventional wave geophysics embodies the concept of interfaces and data processing/interpretation tends to exclude all other possibilities. If we assume that gradational properties can exist then it seems important to explore both interface and smooth behaviour in the interpretational models.

The interpretation of the results relies to some extent on the crustal mechanisms that generate resistivity variations. This is a large subject but a brief background, with special reference to granitic rocks, is provided in section 6.

The interpretation of the lateral geoelectric anisotropy takes place in section 7. Shallow and spatially-limited anisotropy is considered in relation to the surface joint/fracture system. The regional anisotropy is also described and, since the data are spatially limited, a tentative

interpretation is provided.

The interpretation of the vertical crustal section is considered in section 8. The interpretation concentrates on the upper 10 km of immediate interest and comments concerning likely mechanisms are included. The geoelectric results are also compared with the results of the deep seismic refraction experiment described by Brooks et al. (1984).

Since the subject of the nature of jointing and stress at depth within a granite is of considerable importance to geothermal development, the extent to which the geoelectric results can provide useful information is examined in section 9.

3. THE FIELD EXPERIMENT.

The field experiment took place between June 15 and August 13 1988. The equipment was operational for 7 weeks. The field-system used was the 1988 version of the BGS Audiomagnetotelluric (AMT) system (Beamish 1987). Staff allocations precluded the use of a radio-linked remote-reference installation. The two reference magnetic sensors were used in a local (same field) reference mode and this proved satisfactory.

The computer-based (DEC 11/73) AMT system collects and analyses 7-channels of natural electromagnetic (EM) fields across a bandwidth from 100 to 0.01 Hz. Components are referred to as Ex (north electric), Ey (east electric), H (north magnetic), D (east magnetic), Z (vertical magnetic), Href (north magnetic reference) and Dref (east magnetic reference). The system provides a composite bandwidth using four decade ranges. The ranges will be referred to as Decade 1 (100 to 10 Hz), Decade 2 (10 to 1 Hz), Decade 3 (1 to 0.1 Hz) and Decade 4 (0.1 to 0.01 Hz). System enhancements used during the field survey consisted of new 'tunable' 50 and 150 Hz notch filters and interactive graphics software for in-field data processing. The methods of data processing are not described here. The main element of tensor estimation from the spectral matrix is based on the established procedures of remote-reference techniques described by Gamble et al. (1979) and by Travassos and Beamish (1988).

The two concurrent field experiments to be described consist of the main E-W survey profile across the granite outcrop and the survey profile across a target lineament.

3.1 The granite survey.

The target traverse required 10 soundings along an E-W profile (32 to 33 Northing) with an additional two, off-set soundings for control. The sounding locations of the main experiment are shown in Figure 3.1. Twelve soundings were obtained along an E-W profile across the granite (site locations 101-112) and a group of three soundings were obtained above and to the NW of

the HDR reservoir at Rosemanowes quarry (site locations 301-303). The detailed locations of these three sites in relation to the microseismic cloud associated with the reservoir are shown in Figure 3.2. Two soundings were obtained off the main granite outcrop (site locations 201-202). Site locations and elevations are given in Table 1. The site designation codes are grouped in the three 'sets' indicated above and these three sets will be used for presentation purposes. As can be seen in Figure 3.1, site numbers increase easterly within the three sets.

During the acquisition of the 12 profile soundings, installations at 6 other locations gave rise to data contaminated by electric-fence noise (EFN). The six locations (a to f) are shown in Figure 3.3 and listed in Table 1. This particular form of noise is discussed in Appendix A. Across the profile survey coverage was most difficult between 72.5 and 74.5 Easting (see Figure 3.1). This arose due to unfavourable combinations of EFN, topography and land access.

3.2 The lineament survey.

In addition to the main traverse of the granite, a detailed investigation of a target surface lineament was carried out. This survey was intended to test the hypothesis that such a feature provides a 'thin' fluid-permeated zone. The forward modelling of type structures, described in Appendix B, indicated that only high-frequency ($f > 1$ Hz) soundings would be required. For a typical symmetrical structure the traverse length could be limited to less than 500 m. The map of major fractures derived from geological and topological maps together with Landsat photographs (Gregory and Durrance 1987, Fig.8) was used as a reference; it is shown in Figure 3.4.

For logistic reasons it seemed appropriate to conduct the lineament survey in the vicinity of the main E-W profile. It also seemed appropriate to choose a NW-SE trending lineament as a type example as this is a predominant trend of lineaments (cross-courses) which display enhanced permeability in local mines. The nature of the land-use, small fields, the juxtaposition of crops and cattle and much sub-letting limited the choices considerably. The first choice was a lineament (A-A') shown in Figure 3.5 at the western end of the profile. The lineament had an associated topographic low expression. Despite many discussions with local farmers access difficulties posed too much of a problem. A second selection was made towards the centre of the profile (framed in Figure 3.5) between 71 and 72 Easting. The target was a portion of a main NW-SE lineament which transects (assuming lateral continuity) the whole granite outcrop. The lineament has no discernable topographic expression in the vicinity of the profile.

The seven site lineament survey is shown in detail in Figure 3.6. Site designation codes read from 491 to 497 . A 50 m spacing, dropping to 25 m due to boundaries, was used. To our knowledge this is the first AMT experiment involving such small spacings. The profile has a bearing of 19 degrees (grid) and intersects the projection of the lineament as shown in Figure 3.6. As indicated above only high-frequency (Decade 1 and Decade 2, 100 to 1 Hz) data were

collected.

3.3 Data quality.

The quality of data obtained by the field experiment can be described as 'good' although this is a rather meaningless average when the details are considered. The power content, and hence signal-to-noise levels of natural signals are inherently variable. To counter natural variability at low frequencies the low frequency decades (Decades 3 and 4) were collected for two successive nights (unattended operation) at each sounding location. This proved adequate at the majority of locations.

General comments about data quality can be made with reference to the two resistivity sounding curves shown in Figure 3.7. The results for the two sites 102 (in the west) and 110 (in the east) can be considered typical and represent two 'outcomes' of data collected and the processing applied. The results shown are the apparent resistivities (R) and associated phases (P) in the two principal measured directions (north=xy and east=yx) as a function of frequency. Error bars are 1 standard error.

Throughout the survey the data quality of Decades 1 and 2 remained high. The hardware and software procedures for the removal of 50 and 150 Hz proved very effective. An inevitable spectral gap always results however around 50 Hz. The most severe test of 50 Hz rejection was experienced at sites 302 and 303 which had to operate within 200 m of the main 33 kV pylon-line near Rosemanowes quarry. Data quality across Decades 3 and 4 proved more variable and a small spectral gap often occurs around 1 Hz (Fig. 3.7b). The spectral gap around 0.1 Hz is present in all the (impedance) results and is due to a system calibration error. It is recommended that a complete procedure for accurate field-calibration of the system be introduced in future. Of the 17 full-bandwidth soundings performed for the main granite profile only site 108 produced an 'inadequate' set of results. Only vertical field results are presented for this site. Low frequency data were not acquired at site 302.

Different comments concerning data quality apply to the vertical field results from the same two sites shown in Figure 3.8. The sounding curves are presented as induction arrows displaying magnitude (Gr,Gi) and direction (AzGr,AzGi). Error bars are 1 standard error. In the case of the vertical fields, the higher frequencies (Decades 1 and 2) suffer most variability due to wind-vibration and ground-roll. Despite some severe meteorlogical conditions, however, only one site (104) produced inadequate high-frequency results. Low frequencies provided the better (overall) data quality during the course of the survey.

As noted previously electric-fence noise (EFN) was detected at the six locations shown in Figure 3.3. The effects of EFN are described in Appendix A.

4. RESULTS OF THE LINEAMENT SURVEY.

The seven site lineament survey is shown broadly in Figures 3.5 and 3.6. Site codes are from 491 to 497 as shown in Figure 4.1. Only high-frequency data (100 to 1 Hz) were collected for this survey. Vertical fields were collected at sites 492, 494 and 496. The primary objective is to compare the field sounding results with the results obtained from the forward 2-D modelling of type-structures. The modelling results, described in Appendix B, are presented as profile variations in resistivity and phase across test structures. The results of Appendix B consist of two orthogonal polarisations (E-pol and H-pol) and are presented for 3 test frequencies from 100 to 1 Hz. In the case of E-pol results, profile variations of the in-phase (Zr) and in-quadrature (Zi) vertical magnetic field are also included as profile results. In addition to the information provided in Appendix B, a relevant example of the interpretation aspects of E field and Z field azimuths can be found in section 5.8. In order to assess data quality and as a prelude to presenting profile variations, the resistivity sounding curves are considered first.

4.1 Resistivity sounding curves.

The sounding curves obtained from all seven sites are overlaid in Figure 4.2. The results shown are the apparent resistivity (R) and associated phase (P) in the two principal *measured* directions (north=xy and east=yx) over the bandwidth from 100 to 1 Hz. It can be seen that, in relative terms, the north (xy) curves appear stable while the east (yx) curves show considerable variability. The variability is most pronounced in Decade 2 (10 to 1 Hz). In addition, while the variations in Rxy appear systemmatic along the profile (see section 4.3) the variability in Ryx is spatially erratic. The instances for which Ryx >> Rxy indicate an additive noise component in the Ey (east) electric field. A retrospective and detailed examination of the survey data collected has revealed electric fence noise primarily confined to the Ey electric field at all seven sites. Details are provided in Appendix A. It should be noted that the lineament survey was carried out *prior* to the detailed investigation of electric field noise described in the Appendix.

The unreliable nature of the Ey component means that the complete (2x2) impedance tensor cannot be formed and we are unable to provide rotational information from the impedance results. While the hindsight detection of the contamination of the Ey field is unfortunate, it is still possible to examine the profile spatial behaviour of the Ex (xy) component results together with the vertical field results obtained at sites 492, 494 and 496.

4.2 Vertical field results.

The analysis of the vertical magnetic field is particularly useful in the detection of lineament-type resistivity contrasts. Such a 2-D contrast generates a vertical field only in a direction normal to structural strike (E-polarisation, see Appendix B). When the information is presented in terms of induction arrows, the azimuths must be *perpendicular* to the strike direction of the contrast generating the vertical fields. Azimuths of real (in-phase) and imaginary (in-quadrature)

induction arrows are shown in Figure 4.3 at two frequencies of 8 and 88 Hz. At the lower frequency (Fig. 4.3a) azimuths are approximately parallel to the projected lineament strike. This indicates that the lineation has no low-frequency expression in the vertical magnetic field. At the higher frequency of 88 Hz (Fig. 4.3b), the same imaginary azimuths are maintained but the real azimuths do display a spatial rotation towards 'normal-to-strike' as the lineation is approached. The results *indicate* that the only vertical field expression of a simple conductive structure associated with the lineament is confined to the in-phase vertical field at frequencies approaching (or higher than) 100 Hz.

Figure 4.3 displays only azimuthal information. The amplitudes of the real (Zr) and imaginary (Zi) induction arrows along the profile are shown in Figure 4.4 for three frequencies. Detection of a conductive contrast would follow from zero values (Zr and Zi) above the structural axis together with an associated spatial wavelength away from the axis (see Appendix B). Although at 88 Hz, the response is largely in-phase (Zr >> Zi), no significant (at the 95% level) spatial variation is observed across the profile.

4.3 Resistivity results.

Although an examination of the Ey-field results appears unwarranted, it is worth examining the profile results obtained for the Ex-field in the measured north direction. It is obvious from the projected lineament strike that the north measurement will provide a combined response azimuthally offset between the limiting cases of E and H polarisation.

The profile variation in apparent resistivity and phase is shown in Figure 4.5 for the three control frequencies used above. There is an apparently significant and spatially-consistent variation in apparent resistivity across the profile while the associated phase remains stationary. While we cannot entirely rule-out EFN contamination in these results we note that the observed spatial behaviour does *not* follow the pattern of contamination experienced by the orthogonal Ey component. Detection of a conductive contrast would follow from a *minimum* in the apparent resistivity. The 'peak' response in apparent resistivity displayed in Figure 4.5 is *not* consistent with the monotonic decay observed in the vicinity of single isolated structures (see Appendix B).

4.4 Discussion of lineament results.

Although the lineament survey data were marred by EFN contamination, the results presented do offer some constraints in relation to the examples of Appendix B. It should be noted that only a simple vertical (or sub-vertical) fluid-filled (i.e. conductive) zone is considered.

It is highly unlikely that the results obtained can be viewed as compatible with a conductive zone of any substantial resistivity contrast which intersects the surface or near-surface. It could be argued that the results do not rule out a conductive zone which is deeply buried (see Fig. B.4b, Appendix B). In this case, the magnitude of the vertical field (Fig. 4.4) suggests that the zone

would need to be considerably off-set (at depth) from the surface expression of the lineament. In addition, it is likely that the upper surface of the zone would need to be deeper than 250 m to provide a degree of compatibility with the results obtained. Such a deeply buried zone is not considered likely.

Although the results are somewhat restricted, it seems unlikely that the depth projection of the lineament is simply associated with a substantial conductive zone. The feature targeted in this study does not appear to represent a 'thin' fluid-permeated zone that persists to deeper crustal levels.

5. RESULTS OF THE GRANITE SURVEY.

5.1 Introduction.

Because of the 3-D nature of the sounding technique this section attempts to separate results related to one-dimensionality (the vertical resistivity profile) from the two-dimensional azimuthal information related to lateral geoelectric anisotropy. To assist in the interpretation of results we have transformed frequency to an equivalent one-dimensional depth as described below.

5.2 Framework for analysis and interpretation.

These comments are supplied to assist in understanding the background to the results that will be presented. The basic relationships of the magnetotelluric method are summarised in Figure 5.1. Each sounding represents an approximately hemispherical volume of electromagnetic wave propagation beneath and around the site. The radius comprises both depth and lateral distance. Since it is a *volume* sounding, the fields and results may be influenced and interpreted in a full three-dimensional (3-D) sense. The penetration radius must increase from a minimum at the highest frequency to a maximum at the lowest frequency used. The actual values achieved depend on the resistivity structure encountered. The sounding values (the impedance tensor as a function of frequency) can be viewed as a 1-D sounding curve which may be perturbed by lateral variations in geoelectric structure. In the near-field of strong lateral contrasts, the lateral effect may well dominate and the concept of a vertical sounding radius is misleading.

Normally magnetotelluric interpretation parameters, derived from the impedance tensor, are plotted as a function of frequency. To assist in the interpretation of results we have transformed frequency to an equivalent depth scale. When the structure encountered is 1-D, it is possible to transform an observed impedance/frequency estimate to an equivalent resistivity(ρ^*)/depth(z^*) estimate. This is the ρ^* - z^* transformation described in detail by Schmucker (1987). Thus in the 1-D case we can map any interpretation parameter from the frequency to the depth (z^*) domain.

When the structure is not 1-D we can usefully employ a rotationally invariant average impedance, derived from the principal impedances (xy and yx) as

$$Z_a = (Z_{xy} - Z_{yx}) / 2$$

Since Z_a is rotationally invariant we can effectively use this impedance to again transform from frequency to depth. The sequence used here in presenting results as a function of depth is to form Z_a at each frequency estimate. This impedance is then transformed to the complex impedance of Weidelt (1972) as

$$c(\omega) = g(\omega) - i.h(\omega) = Z_a(\omega)/i\omega\mu_o$$

Where ω is angular frequency and μ_0 is the magnetic permeability of free space. We then form a depth estimate as

$$z^*(\omega) = Re(c(\omega)) = g(\omega)$$

with z^* expressed in metres. The estimate is an indicator of the depth in the same sense as a 'centre-of-mass'. The depth z^* is referred to as P. Depth with P denoting Pseudo.

5.3 Penetration depths.

The 1-D penetration radii, interpreted as penetration depths (z^*) as discussed above, which were achieved by the survey are now considered. The results are shown for the four decade sounding bandwidth in Figure 5.2 using the standard 3 sets of site groupings. Simple consistency tests for the applicability of 'one-dimensionality' result in some points being omitted, usually at deeper penetrations.

The granite survey results (SET 1, Fig.5.2a) display reasonable consistency with the exception of site 105 whose curve indicates a more conductive (greater attenuation) crustal section. Omitting site 105, minimum penetration depths range from 832 m (site 106) to 1,686 m (site 110) for the on-granite soundings. The two off-granite soundings (Fig. 5.2b) are clearly more attenuated by a more conductive upper-crustal section. Minimum penetration depths are 452 m (site 201) and 515 m (site 202). The penetration depths achieved by the three centre-granite soundings (Fig. 5.2c) are broadly equivalent to those along the granite profile.

5.4 Dimensionality indicators.

In order to provide reasonable interpretations of the data we first perform an assessment of the likely 'dimensional' influences on the sounding curves. A background to this aspect of

interpretation is given by Beamish (1986). The interpretation is not exact; it is more a matter of degree.

The skew values (logarithmic scale) for the three sets of site groupings are shown in Figure 5.3. We are not interested here in the depth dependence since skew is usually an erratic (low s/n) parameter. The overall magnitude of skew can be used to identify likely 3-D contributions to a sounding curve. For these data we can identify skew values of < 0.2 as 1-D and/or 2-D contributions and skew values > 0.2 as the onset of 3-D contributions. The results of Figure 5.3 indicate that the off-granite site 202 is the only site to be influenced by a significant 3-D contribution. The grouping of skew values of > 0.1 at large p. depths for the SET 1 results derive from the eastern-most profile sites 110, 111 and 112.

To further identify dimensional influences, the dimensional weights D1, D2 and D3 (see Beamish 1986) are shown in Figure 5.4. These weights, in the range 0 to 1, attempt to simultaneously assess the *relative* dimensional contributions to the sounding curves. The 1-D (D1) weights shown in Figure 5.4a are high (> 0.75) for the SET 1 granite sites. The D1 weights display a monotonic decrease with increasing penetration radius. The D1 weight at site 201 is clearly low while the D2 (2-D) weight at this site (Fig. 5.4b) is distinctly high thus confirming strong 2-D contributions at this off-granite site. The D3 weight for site 202 (Fig. 5.4c) confirms the high skew value at this site and emphasises the 3-D influence at this off-granite site.

Taking into account all the dimensional indicators we can confirm that for the upper 12 km of the crustal section, the sounding data on the granite possess a strong 1-D contribution while retaining an additional constant and persistent 2-D factor. The degree of 'one-dimensionality' decreases with depth through the lower crustal section.

5.5 Anisotropy ratios.

If all the sounding data were 1-D then there would be only vertical (depth) information to be assessed. Since we have established that there exist 2-D influences on the sounding data, rotational characteristics of the impedance tensors can be examined. Conventional methods exist to extract this information based on simple rotations in the horizontal plane (Word et al. 1970). More recent and reliable formulations decompose the impedance tensor via an eigenstate analysis thus providing state eigenvalues and eigenvectors (Eggers 1982). We here use the characteristic state formulation of the impedance tensor developed by Tzanis (1987). This analysis provides extremal values (magnitudes, phases and azimuths) of the impedance tensor. From this analysis we obtain the maximum (and minimum) states of the **E** and **H** fields. The horizontal azimuth of the maximum **E** state defines a direction of maximum resistivity. The direction of minimum resistivity (maximum **H** state) will be approximately orthogonal to the direction of maximum resistivity.

Before discussing azimuthal information, the anisotropy ratios defined by the maximum and minimum states are first presented. Because the information now starts to become variable with depth we concentrate on the results from the upper crustal section (p. depths in the range 0 to 10 km). The anisotropy ratio (AR) is simply defined as the ratio of maximum to minimum apparent resistivities determined by the eigenvalues of the impedance tensor. The lower bound of the AR is of course unity.

The results obtained for the SET 1 profile sites across the granite are shown in Figure 5.5a. With the exception of the initial behaviour at site 109, the results are remarkably consistent and form a set of values in the range 1.5 to 3. The relatively depth-independent behaviour indicates that the 2-D influence provides a *parallel off-set* between the maximum and minimum resistivities.

The results for the SET 2 and 3 sites are shown in Figure 5.5b. The AR at site 201 (strong 2-D) are clearly unique to this site and the rapid movements suggests the near-field influence of strong anisotropy. In the results obtained for the SET 3 sites it can be noted that the AR ratio at site 301 is more variable than at sites 302 and 303 which display equivalent values in the upper 7 km.

5.6 Rotational characteristics.

From the above analysis we obtain the maximum (and minimum) states of the **E** and **H** fields. The horizontal azimuth of the maximum **E** state, here referred to as GE, defines a direction of *maximum* resistivity. In simple terms, if the major fluid-filled lineaments of the granite were directed NW-SE then the direction of maximum resistivity (GE) would be NE-SW. Rotational characteristics and the interpretation of maximum and minimum resistivities are discussed further in sections 5.8 and 9. The direction of minimum resistivity will be approximately orthogonal to GE. We again concentrate on the results fron the upper crustal section. All horizontal azimuths refer to grid north and GE is defined in the range $-90^{\circ} \leq GE \leq +90^{\circ}$.

The azimuths GE for the SET 1 sites across the granite are shown in Figure 5.6a. There appears to be a distinction between the azimuths (and rotations with depth) obtained in the extreme west (sites 101 and 102) and the consistent set formed by sites 103, 104, 105, 106 and 107. At site 109 the initial 'swapping' is simply due to +/- azimuth ambiguity but it seems clear that this site (to the south of the main profile) detects a maximum direction that is approximately orthogonal to that at the other sites i.e. it is more 'normally' a *minimum* direction. It is also noteable that the azimuth at site 110 rotates below 5 km to a 'minimum direction' similar to that at site 109. The azimuths at the eastern profile sites (110 to 112) display behaviour that is more in character with sites 101 and 102.

It can be seen in Figure 5.6a that, with the exceptions of sites 109 and 110, the azimuths display a characteristic rotation with depth through the upper crustal section. The azimuths clearly

rotate counterclockwise with increasing depth. Although 'local' influences are apparent at the shallowest depths (around 1 km), azimuths appear confined to the NE/ENE sector. In the lower part of the section, azimuths are confined to the N/NE sector.

Azimuths (GE) at the off-granite sites are shown in Figure 5.6b. At site 201 (strong 2-D), a stable depth-independent azimuth is observed. At site 202 (strong 3-D) a straightforward interpretation of a single horizontal azimuth is probably not possible.

The SET 3 site azimuths are also shown in Figure 5.6b. The behaviour at site 303 is unusual. Within the upper 5 km the azimuth rotates rapidly i.e. it 'spins'. Below 5 km the azimuth rotates to a direction that is consistent with the 'normal' granite azimuths of Figure 5.6a. In contrast the azimuths at sites 301 and 302 display a direction that would be classified as a 'minimum' direction with respect to the behaviour at the majority of granite sites.

The azimuthal information is generated by the inherent geoelectric anisotropy of the upper crustal section. It is clear from the results presented that the azimuthal information is sensitive to location on the granite. We observe an inherent spatial character both from west to east along the profile and from north to south across the profile. Within the variability observed we can identify the 5 profile sites 103, 104, 105, 106 and 107 as forming a 'consistent' set of azimuths for the upper crustal section.

The principal azimuths of maximum (GE) and minimum resistivity (GH) for the complete bandwidth at each site have been plotted for each frequency decade of the sounding. An example of the complete information at a single site is shown in Figure 5.7. It should be noted that only azimuthal information is considered. Amplitude information in the form of the anisotropy ratios has been considered previously in section 5.5. In order to provide summary spatial information, the results for individual decades (see Figure 5.7) have been plotted in map form. We here consider only the direction of maximum resistivity (GE). The maps for the four decades are displayed in Figure 5.8. Because the azimuths rotate with frequency (penetration radius), individual sequences or complete sectors have been identified in some cases.

For sites on the granite considerable counterclockwise rotations exist across Decades 1 and 2 (Fig. 5.8 a,b). The spatial variation observed indicates that different portions of the granite exercise different control on the direction of maximum resistivity. On the granite the pattern that emerges from Figures 5.8 a,b is that the western portion covered by sites 101, 102, 103, 104, 105, 106 and 107 appears relatively consistent. The SE portion of the granite covered by sites 109, 110, 111 and 112 exhibits a set of azimuths which may be linked by a large-scale *spatial* rotation not observed to the west. The SET 3 results with the exception of the spinning rotation at site 303 are more in keeping with the azimuths obtained in the SE. The 2-D (site 201) and 3-D (site 202) off-granite sites, particularly 201, are largely irrotational over this bandwidth.

A distinct sequence of rotations occur with decreasing frequency across Decades 2, 3 and 4

(Figures 5.8 b,c,d). The azimuths at the lowest frequencies (Decade 4, Figure 5.8 d) are all associated with a (theoretical) penetration radius of greater than 30 km and yet a remarkably stable set of orientations is observed. To some extent the azimuthal rotations observed across Decade 2 and 3 (Figure 5.8 b,c) can be viewed as transitional from the azimuths relating to the upper 4 km (Decade 1, Figure 5.8a) to the spatially uniform set observed in Figure 5.8d. It appears then that the azimuth configuration at the lowest frequencies is largely *decoupled* from the spatially-dependent, near-surface set of orientations found at the highest frequencies. The slight exception to this is the retention of a possible large-scale spatial rotation across the SE portion of the granite.

It is worth remarking that the complete information presented in Figure 5.8 contains a large amount of spatial detail concerning the lateral anisotropy of the granite. As a background to this information we note that the results indicate a spatially non-homogeneous geoelectric anisotropy in the upper crustal section that transfers to a regional and relatively spatially-independent anisotropy at large (> 30 km) penetration distances.

5.7 The vertical resistivity profile.

The dimensional information considered in section 5.4 revealed that the sounding data on the granite possess a strong 1-D contribution while retaining a relatively constant 2-D influence. The 2-D influence provides anisotropy ratios of between 1.5 and 3.0 through the upper 12 km of the vertical section. The degree of the 1-D influence decreases with inceasing depth. In order to provide an assessment of the resistivity/depth profiles for the complete survey, the rotationally-invariant, average impedance is used throughout the analysis.

The 1-D inverse methods used are an attempt to recover the resistivity profile using automatic methods. The sounding data, in this case the average impedance, together with its associated errors are used to provide models that are consistent with the observations at a certain level of misfit. Three inversion schemes have been applied to survey data. The first is an approximate transform in which errors are not utilised. The second scheme provides minimum-norm (best-fit) solutions when the section is characterised by a series of layers. The third scheme provides a solution as a smooth resistivity profile at a chosen level of misfit.

The ρ^* - z^* transformation as discussed previously is particularly appealing as it imposes no constraints on the solution space (i.e. interfaces, layers or a continuum). The results of the transformation are shown in Figure 5.9 in the usual log-log scaling. The SET 1 profile results (Fig. 5.9a) have been separated into two groups which display slightly different resistivity values. With the exception of site 105 the group of western sites 101 to 107 display very consistent behaviour, the resistivity increasing with depth until a turning point is reached in the middle/lower crust. The result obtained at site 105 appears anomalous. The results obtained at sites 109 to 111 appear consistent with slightly larger resistivity values than sites to the west. The profile at site 112 is, by contrast, more typical of the profiles obtained to the west.

The SET 2, off-granite results (Fig. 5.9b) are clearly characterised by much lower resistivities (several hundred ohm.m) in the upper kilometer. Typical on-granite resistivities (i.e. > 1000 ohm.m) are only achieved below 1 km. The SET 3 site results (Fig. 5.9b) display the overall characteristics of the SET 1 profile results of Figure 5.9a. These results are considered in more detail below.

The same results are repeated for the upper crustal section (0 to 10 km) using a linear depth scale in Figure 5.10. The same comments as above apply but the plots provide greater detail in the depth range of immediate interest. All the sites on the granite (with the exception of site 105) display resistivities in the range 1000 to 10,000 ohm.m for the whole crustal section with sites in the SE (109 to 111) displaying the highest overall resistivities. In Figure 5.10a, the results for sites 101 to 107 (again excluding 105) provide a highly uniform set of depth profiles. In the upper 2 km resistivities range from 900 to 2500 ohm.m and these increase to values in the range 2700 to 5000 ohm.m at a depth of 10 km.

The depth profiles obtained for the SET 3, HDR sites shown in Figure 5.10b are interesting because the results at sites 302 and 303 are identical down to 5 km and exhibit lower resistivity values than site 301. Reference is made to Figure 5.11 in which the detailed site locations are shown in relation to the microseismic zone associated with the reservoir. Site 303 is located centrally over the 'cloud' while site 302 is some 500 m to the north. Site 301 is located 1.3 km away fron site 303. It can be argued that the common resistivity profile at sites 303 and 302 represents a low-resistivity, reservoir-influenced section while the higher resistivity profile at site 301 represents a nearby but non-reservoir-influenced section. Expanding the resistivity scale to one order-of-magnitude and including errors results in the profiles shown in Figure 5.12. The resistivity contrast between 303/302 and site 301 although small appears significant down to a depth of 4.5 km where the profiles merge. Below this depth the resistivity profiles at all three sites are similar down to a depth of about 8 km. To further emphasise the correlation the vertical section at sites 303/302 and 301 is compared against the vertical section containing the microseismic zone in Figure 5.13. No information is available for the first kilometer but the two curves 'start' displaced at a depth of 1 km. Apart from the displacement a significant feature of the 'reservoir-influenced' profile (site 303) is the low-resistivity 'bulge' with an onset at about 2.5 km. This is in contrast to 'normal' depth-increasing (or constant) resistivity behaviour. The return to 'normal' resistivity values at a depth of about 4.5 km appears consistent with the termination depth of the microseismic zone.

The inversion scheme that treats the vertical section as a stack of discrete layers is due to Fischer and Le Quang (1981). As applied here the starting model (the parameters of the crustal section) consists of 5 layers above a uniform half-space of 1000 ohm.m. In each case the minimum-norm solutions are presented which can, if no constraints are applied, provide extreme model behaviour. No constraints other than the initial parameterisation were applied in the present case. Adequate fits to the data were obtained. The measure of misfit used (EPS as

defined by Fischer and Le Quang) provided values from 0.030 to 0.050 in the majority of cases.

The results for the SET 1, granite profile sites are shown in Figure 5.14 again split into two groups (Figure 5.14a,b). The first 'at-surface' layer is not resolved by the data bandwidth. Below a depth of 1 km the previous pattern of inceasing resistivity with depth is broadly observed. Individual layer parameters which involve relatively small resistivity movements are not likely to be significant. The eastern-most sites (Fig. 5.14b), with the exception of site 112, again display slightly higher resistivity values in the upper 5 km.

Although a minimum-norm 1-D inversion should not be attempted for data displaying strong 2-D or 3-D characteristics the results for the SET 2, off-granite sites are shown in Figure 5.14c. The overall oscillatory nature of the solutions can be noted. What is of interest is the transition depth from low resistivities (several hundred ohm.m) to typical granite resistivities (> 1000 ohm.m). At site 201 the transition depth occurs at about 1 km while at site 202 the transition occurs at around 1.75 km. If we assume that the low resistivities are associated with the Devonian cover then the transition depth defines the granite contact. Reference to the contour map of the depth to granite of Figure 2.1 indicates that the depths observed can be interpreted in this way.

The results of the layered inversion scheme applied to the SET 3, HDR sites are shown in Figure 5.15. The results obtained are in overall agreement with the equivalent transform results of Figure 5.12. The small resistivity contrast between sites 303 and 301 transfers to a common resistivity profile at a depth of about 4 km. The difference between this depth and the transitional depth region of Figure 5.12 is simply a matter of parameterisation. The point-discontinuity interfaces generated by the layered solution are considered to be the least attractive when modelling the resistivity profile of a fluid-filled reservoir.

Since the layered interface-type solutions for the SET 1 profile sites (Fig. 5.14a,b) do not reveal any spatially-consistent major discontinuities across the upper vertical section, solutions involving only *smooth* behaviour are now considered. The algorithm for generating smooth vertical profiles is the Occam inversion presented by Constable et al. (1987). Rather than fitting the sounding data as well as possible (which maximises interface-type behaviour), the smoothest model which fits the data to within an expected tolerance is sought. A 99% confidence level (fitting the whole data to within 3 standard errors) was used here.

The results for the SET 1 profile sites are shown in Figure 5.16, and are separated into three groups running west to east (Fig. 5.16a,b,c). In most respects the solutions obtained are smoothed versions of the previous transform and layered results. Given the results obtained thus far it is extremely tempting to interpret the low resistivity layer (Figure 5.14) or gradient (Figure 5.16) observed at some of the sites at a depth of about 1 km. The locations where this behaviour is observed are sites 103, 104, and 105 and 107. The behaviour is most pronounced at sites 103 and 104 which straddle one of the main NE-SW alluvial fans of the area (see

below).

The resolution of the data in the upper 1 km is difficult to determine. The at-surface resistivity of each solution depends on high-frequency asymptotic behaviour 'extrapolated' by the minimisation. It should therefore be appreciated that the 'definition' of this layer/gradient depends primarily on the extrapolated value of the at-surface resistivity. At present we have no way of confirming the at-surface values obtained. At two locations (sites 105 and 106) however, consistently low at-surface resistivities (of order 500 ohm.m) are observed. Reference to the site locations in relation to the main alluvial fans crossing the area (Figure 5.17) shows that these two sites are indeed the only two sites situated centrally within major fans. Reference to the regional geological maps confirms that the fans in question provide major arterial connections to the coast. Of the two sites in question, site 105 is situated on Porkellis moor which, in volumetric terms, appears to represent the main alluvial 'basin' on the granite. The trend of the fan coastwards (NE-SW) also represents one of the main NE-SW trending lineaments on the Carnmenellis structure. It is suggested that the relatively low resistivity values obtained at site 105 are due to the spatially-localised influence of the alluvial fan and/or associated lineament.

The Occam inversion results at the SET 3, HDR sites are shown in Figure 5.18. While the solutions exhibit the same principal features of the earlier vertical sections, the detailed behaviour is strongly dependent on the at-surface resistivity values. The previously-noted cautionary comments should be applied. Finally the Occam solutions for all the sites on the granite (excluding 105) are overlaid in Figure 5.19. These provide a summary of the one-dimensional bounds on the resistivity section across a substantial portion of the Carnmenellis outcrop. If the spatial variation of the upper 1 km is excluded, a well-defined median profile can be extracted.

5.8 Vertical field results.

The vertical field results provide strike information on predominantly vertical or sub-vertical resistivity variations in the vicinity of the sounding site. Such variations generate a vertical field only in a direction normal to structural strike (E-polarisation, see Appendix B). When the information is presented in terms of induction arrows, the azimuths must be perpendicular to the contrast generating the fields.

As an example consider a major vertical, fluid-filled lineament striking NW-SE. Such a feature, if the resistivity contrast is high, would generate a vertical field *only* in a NE-SW direction. Vertical field induction arrows would be directed NE-SW and because the vertical field changes phase across such a feature, induction arrows would point *towards* the conductive zone on *both* sides of the lineament. The vertical field would be zero directly above the location of the lineament. If the lineament is two-dimensional (i.e. it appears in electromagnetic terms to extend to $\pm$ infinity), the two principal (i.e. maximum and minimum) resistivity directions are horizontal and are generated as an orthogonal pair in the NW-SE and NE-SW directions. The individual direction in which maximum resistivity occurs depends on the 'nature' of the resistivity contrast. For this conductive lineament example, maximum resistivity occurs in a NE-SW

direction on either side of the conductive zone (this is H-polarisation in the examples of Appendix B). Directly above the lineament however the maximum resistivity direction will 'swap' by 90° to become NW-SE (this is E-polarisation in the examples of Appendix B). Such behaviour provides a 90° ambiguity in structural strike interpretation if only principal resistivity directions are available. The 90° ambiguity of structural strike is removed only by making some form of assumption or by reference to corresponding vertical field results. In strictly two-dimensional terms, the directions of maximum and minimum resistivity will always be parallel or perpendicular to the direction of the vertical field. In simple situations a comparison of the principal E field and Z field azimuths might reveal the extent to which the structure encountered can be considered two-dimensional. Such azimuthal comparisons are undertaken in section 7.

In order to first assess the extent to which the vertical fields are influenced by local and/or regional variations, induction arrows are presented for the four decades of the sounding. In this first presentation only the SET 1, profile sites are considered. For each decade we present results for two groupings of on-granite sites. The first group comprises sites 101, 102, 103, 104, 105, 106 and 107. The second group comprises the SE sites 109, 110, 111 and 112. For each decade of the sounding we present first the real (in-phase) azimuths for the two groups followed by the imaginary (in-quadrature) azimuths. Amplitude information is also included. The scale diameters for the real results are 0.5 compared with 0.25 for the imaginary results i.e. the imaginary magnitudes are enhanced by a factor of 2 with respect to the real magnitudes.

The Decade 1 (100-10 Hz) results are shown in Figures 5.20a,b in which the reason for the separation into 2 groups of sites is evident. The SE sites 109 to 112 clearly display much larger magnitudes in both real and imaginary components. The western sites 101 to 107 show a great deal of spatial variability and real and imaginary azimuths display little or no parallel/antiparallel behaviour. The Decade 2 results of Figures 5.20c,d show a similar pattern with even more spatial variability. In fact this part of the bandwidth provides much frequency-dependent rotation at the majority of sites. The beginnings of regional scale azimuths are detected in the Decade 3 results of Figures 5.20e,f. The vertical field magnitudes for the two groupings become comparable, although distinctly different azimuths are apparent. The transition to a regional set of magnitudes and azimuths has been achieved by Decade 4 (0.1 to 0.01 Hz, Figures 5.20g,h) although the distinctive difference of the SE sites 109 to 112 should be noted. At these low frequencies the vertical field response is predominantly in-phase.

The spatial variation of the vertical field azimuths is now considered using the vertical field maximum response function which avoids separating the response into two distinct phase contributions differing by 90 degrees. In effect the maximum response azimuths display the most appropriate 2-D orientation. The Decade 1 results are shown in Figure 5.21a. Heavy dots denote the 'mean' direction over the bandwidth. Previous comments still apply but now we observe the extent of a spatial 'reversal' between sites 102,103,105 and sites 106,107,108. The

SET 3, HDR sites 302 and 303 display rapid rotations. The Decade 2 results of Figure 5.21b indicate the localised reversal about a NE-SW axis at sites 102 to 108 has disappeared in favour of a more regional set of azimuths. Of particular note at the SET 3 sites is the 'stable' reversal between sites 301 and 303 while the azimuths at site 302 continue rotating. The stable reversal between sites 301 and 303 indicates a strong localised 'edge-effect' striking NE-SW. The rotation to more regional azimuths continues in Decade 3 (Fig. 5.21c) with some degree of continuing reversal between sites 301 and 303. By Decade 4 (Fig. 5.21d) the rotations to a remarkably spatially stable set of orientations appear to have been completed. Judging by the slow spatial decay of magnitudes, the feature to the SW is substantial and generates a minimum wavelength of order 10 km.

6. BACKGROUND TO THE INTERPRETATION OF RESULTS.

Prior to the interpretation of the results a brief background to the interpretation of crustal resistivity variations in crystalline (granitic) rocks is provided. A detailed and more specific examination of the physical controls actually operating in the Carnmenellis granite (e.g. jointing and stress) is deferred until section 9. The two main mechanisms requiring consideration are (a) temperature dependent and (b) pressure dependent resistivity variations. It should be noted at the outset that the in-situ resistivity will be controlled by the crack and pore parameters of the rock coupled with the fluid content. In order to assess the complete dependence, the effects of temperature and pressure have then to be taken into account.

6.1 The temperature dependence of resistivity.

In a series of thorough experiments conducted in the 1960's, Brace and co-workers deduced some of the basic electrical properties of crystalline rocks with low porosities (Brace et al., 1965; Brace et al., 1966). The principal results suggest that over the pressure interval from 0 to 8 kbar (1 kbar = 100 MPa), conduction is by flow of ions in the pore fluids. Thus the effect of temperature is usually incorporated by using the known variation of the pore fluid resistivity with temperature (Quist and Marshall, 1968). The empirically-determined expression relating fluid resistivity to temperature depends on a set of electrolyte-dependent coefficients. Below a temperature of about 370° C, for NaCl solutions close to sea-water, the principal resistivity variation is an approximately linear and reciprocal function of temperature. This form of decrease in resistivity with increasing temperature (and hence depth) would generate a linear 'background' to all other possible influences.

The influence of the fluid volume may be described either in terms of rock porosity (e.g. Brace et al., 1965) or by the 'weight-percent' of free fluids (e.g. Olhoeft, 1981). We would expect the two to be related for a given rock type. According to Olhoeft (1981) the electrical properties of granite appear to be dominantly controlled by the amount of *free* water in the granite and by temperature. Near room temperature a monolayer of water will decrease the resistivity by an

order of magnitude. Several weight-percent of water may decrease the resistivity by as much as 9 orders of magnitude as shown in Figure 6.1. The observed resistivity bounds for the Carnmenellis granite are also shown in the figure and we note that, according to the predicted depth-temperature profile, the likely temperature at a depth of 10 km is about 360 degrees C. Two main points arise from the comparison in Figure 6.1.

The first point is that the observed resistivities of the upper-crustal section are much closer to the 'wet' granite curve. The difference between the bounding 'wet' curve and that observed is likely to be due to the actual weight-percent of free solutions in the Carnmenellis granite. An examination of the resistivity laterolog for well RH15 at Rosemanowes (supplied by CSM/HDR) down to a depth of 2800m, reveals intact formation resistivities of the order of the tool limit (200,000 ohm.m) but with a large depth-integrated density of fracture resistivities descending to several thousand, and in some cases, to several hundred ohm.m. Clearly the volume, or bulk, resistivity is controlled by the low-resistivity (fluid) content of fractures and pores within the highly-resistive intact matrix. The observed vertical resistivity profiles indicate that this control is maintained down to the middle crust.

The second point to arise from Figure 6.1 is that the laboratory temperature dependence gives rise to a decreasing resistivity with increasing temperature, as discussed above. The results of our vertical profiles require an increasing resistivity with depth (and temperature). Clearly the temperature effect is offset by a modified or more dominant mechanism within the Carnmenellis granite. Mechanisms which would cause an increase resistivity with depth are discussed below.

6.2 The pressure dependence of resistivity.

As noted above, the theory of pressure dependent resistivity in low-porosity rocks, saturated with different pore fluids, was established in the 1960's by Brace and co-workers (Brace et al. 1965, 1966, 1968). The model proposed is one in which the mineral grains act as an insulating matrix and conduction occurs solely through the pore fluids. Specifically, the experiments showed that as the external confining pressure is increased, the resistivity rises sharply and then less so. Their data for a series of granites (using 0.3 ohm.m water) are reproduced in Figure 6.2. They also measured the dilatancy of these samples as a function of pressure. The dilatancy rises sharply with pressure and then asymptotically approaches a straight line. The conclusion was that some of the porosity (called cracks) closes up quickly with pressure while that remaining (called pores) does not. This qualitative picture has since been verified by many other experiments on similar systems. It is important to point out that the definition of 'cracks' and 'pores' (as discussed in the above papers) is in terms of their *response* to pressure or stress. Thus 'cracks' close under applied pressure while 'pores', though free to deform elastically, remain open. Due to the fact that the experiments indicate that a wide range of rock types display this type of behaviour, it is presumed that nearly all rocks must contain high-aspect ratio void spaces that can be closed by applied pressure. Such closure will be complete in granites at around 200 MPa (i.e. 2 kbar, Fig. 6.2). The laboratory observations provide further evidence

that *pore* space remains connected in most rocks in spite of deep burial. For example, Brace and Orange (1968b) report that an effective pressure of 1000 MPa was insufficient to eliminate water-filled pore spaces in granitic and other rocks.

It should also be noted that much of this work also accounts for permeability (and hence fluid flow) dependence. The permeability (k) scales with resistivity (ρ) as

$$\rho \propto k^{-1.5}$$

For in-situ rocks, experiment and theory should also take fractures into account. The theoretical work of Stesky (1986) does this for brine-saturated rock but the results are complex and depend on a large number of variables. Most of the above work has consisted of studying the effects of simple unaxial pressure (isotropic stress) using nominally zero pore pressures. Walsh (1981), considering the case of fluid permeability, shows that the influences of confining and pore pressures differed, a result that is likely to be similar for electrical resistivity.

For a realistic granite mass, and the Carnmenellis in particular, we should also take into account the likely influence of both the highly-jointed nature of the granite and the in-situ anisotropic stress-distribution. The subject of crustal stress in the UK is receiving growing attention and a recent review is provided by Evans (1987). The review emphasises that the one good quality stress measurement has been obtained within the Carnmenellis granite. A summary of the in-situ stress measurements taken from Evans (1987) is shown in Figure 6.3. Rummel (1986), reviewing European results, quotes the Cornwall results as an extreme case of high deviatoric stress. It appears it is the extremely low minimum horizontal stress that provides the large deviatoric behaviour.

According to conventional laboratory analyses (e.g. Fig. 6.2) using uniaxial confining pressure, the transfer from crack-dominated behaviour to pore-dominated behaviour will occur at modest lithostatic pressures of say 200 MPa. However at this point it is possible to suggest that the *in-situ* rock-mass behaviour can be described by the dilatant growth and alignment of microcracks which are kept open by pore-fluids at high pressures as described by Brace and his colleagues (Brace and Byerlee, 1967; Brace and Orange, 1968a; Walsh, 1965) and as more recently advocated by Crampin (1985) and by Crampin and Atkinson (1985). The extended theory of Extensive Dilatancy Anisotropy (EDA) has been examined using shear-wave splitting for the Carnmenellis granite by Roberts and Crampin (1986) and their result concerning the mean direction of maximum horizontal stress (30° west) is compared with other indicators by Evans (1987) as in Figure 6.3.

Relatively little work has been developed to relate the implications of the EDA hypothesis to geoelectric behaviour. This is, in part, due to the large influence of *structural* (or macroscopic) anisotropy (see Appendix C). In the absence of such anisotropy a qualitative guide to the likely effects is now suggested. The pressure-dependence of granite resistivity, shown in Figure 6.2,

displays a sensitive, non-linear relationship in the region of laboratory crack-dominated behaviour (e.g. 0 to 200 Mpa). This simple uniaxial dependence would then form a model for deviatoric differences due to an anisotropic stress field. We therefore superimpose an existing stress field with magnitude axes s_H (maximum horizontal, acting at θ_H), s_h (minimum horizontal, acting at θ_h) and s_v (vertical). Using Figure 6.2 we can visualise a situation ($s_H \neq s_h \neq s_v$) which will generate substantial resistivity variations depending on the relative magnitudes of the inequalities. Clearly for a horizontally dominant stress field, *maximum* resistivities will be generated (by s_H) at an azimuth θ_H. For this situation, the degree of resistivity anisotropy will be related to the ratio s_H/s_h. Once again, it should be noted that a detailed examination of the physical control on the observed resistivity variations is undertaken in section 9.

7. INTERPRETATION OF LATERAL GEOELECTRIC ANISOTROPY.

This section describes the extent to which the granite can be considered laterally homogeneous in terms of its rock/fluid properties across the survey area. The results relevant to this consideration have been presented in sections 5.5, 5.6 and 5.7. Specifically we refer to the azimuthal characteristics that have been identified. We note that for sites on the granite the anisotropy ratios are remarkably consistent and form a set of values in the range 1.5 to 3. The azimuths of maximum resistivity (GE) shown in Figure 5.6 display a consistent rotation pattern from NE/ENE at shallow depths to N/NE at a depth of 10 km. The spatial maps of the azimuths presented in Figure 5.8 extend the information to much larger (regional) penetration radii.

A main feature of the rotational characteristics of *both* the E fields (section 5.6) and the vertical fields (Z) of section 5.8 was the transfer from *local* influences at high frequencies (Decade 1) to an apparently regional geoelectric anisotropy at low frequencies (Decade 4). These charactersitics are now considered in turn.

The rotation with depth across the upper vertical section is likely to be due to the transition from near-surface to regional influences. The near-surface hydrogeological model of the granite (Burgess et al. 1982) implies a saline water circulation system down to a depth of 1.1 km and suggests that the joint/fracture system extends to 2 km or more. Gregory and Durrance (1987) extend the hydrogeological model further (using the distribution of radioelement concentrations) and propose and map an active hydrothermal circulation system across the Carnmenellis structure.

The near-surface azimuths of maximum resistivity shown in Figure 5.8a (i.e. Decade 1) display a fairly complex spatial pattern and must therefore be compared with the joint/fracture information which, despite apparent trends, may constitute a 3-D geoelectric 'fabric'. The results of Figure 5.8a are repeated in Figure 7.1 with the major lineations of the region superimposed. Although the azimuthal sectors identify the directions of maximum resistivity, an

ambiguity of 90 degrees arises in the identification of structural strike due to possibilities of the interchange of maximum and minimum resistivity directions as discussed in section 5.8. The ambiguity is only resolved using the vertical field information. The mean directions of the maximum vertical field (GM) for Decade 1 are superimposed on the azimuths of maximum resistivity (GE) in Figure 7.2a. Figure 7.2b expands the information to include lineations in the vicinity and an indication of the apparent zone (shaded) of the conductive feature. The GM azimuths for the SET 3 sites are not displayed since they suffer rapid rotations. It is evident from Figure 7.2 that for the majority of sites the azimuths GE are parallel to 2-D strike, the exceptions occuring at sites 101 and 201. It is also evident from the magnitude of the vertical fields (Fig. 5.21a) that sites 102, 103 (104 is omitted), 105, 106, 107 and 108 provide a consistent low-amplitude set in relation to other sites on the granite. These sites essentially detect a spatially-localised conductive structure striking NE-SW.

If we now refer back to the vertical resistivity profiles of section 5.7 we can correlate this same feature with the anomalously low resistivities observed at site 105. The results of Figure 7.2 appear to be the 2-D contribution of a lineament associated with a main NE-SW arterial fan extending to the coast. It should be noted that the conductive zone *appears* displaced (to the SE) from the NE-SW lineament and associated alluvial fan. The spatial resolution is however limited to about 1.5 km (in the vicinity) and the *association* between the two features is made primarily on the basis of orientation.

The set of azimuths (GE,GM) at sites 109, 110, 111 and 112 in Figure 7.2 together with the enhancement of the vertical field magnitudes shown in Figure 5.21a indicate the influence of a much larger scale effect. It is suggested that the cause is associated with boundary or off-granite variations rather than with variations occuring across the Carnmenellis outcrop although this cannot be ruled out. The different 'character' of the SE portion of the granite extends to much lower frequencies as described below.

The main feature of both the E field azimuths (Fig. 5.6) and the Z field azimuths (Fig. 5.21) for Decade 2 appears to be their transitional character. The NE-SW structure identified by the Decade 1 data has been 'submerged' by the growing influence of a regional scale effect. The most readily identified feature of this bandwidth is the Z field reversal between sites 301 and 303 indicating a strong localised edge-effect striking NE-SW between the two sites.

The main feature of the E field azimuths for Decade 3 is the regional rotation. It is apparent (see Fig. 5.6a) that the directions of maximum resistivity at the western granite sites (101 to 107) have rotated to a reasonably consistent set that is parallel to the irrotational azimuth at the western-most, off-granite site 201. The sites 'defining' the SE portion of the granite again appear distinctive in the azimuths derived from both E and Z fields.

The regional nature of the azimuths is most pronounced in Decade 4. It has been argued that the Z fields are influenced by a substantial regional feature to the SW which provides a long

wavelength anomaly decaying slowly to the NE across the granite. The contribution from the large-scale near-surface granite/cover resistivity variations does not appear to be a likely candidate since the Z field at the western-most, off-granite site (201) is large. The source of the anomaly is therefore intriguing. The projected strike direction of the feature is NW-SE which would be approximately normal to the main set of thrusts of the region (i.e. the Carrick and Dodman thrusts). The origin of the regional anomaly must therefore remain speculative.

The relationship between the Z field azimuths (GM) and the E field azimuths of maximum resistivity (GE) is shown in Figure 7.3. The results are for Decade 4 and comprise two groupings of on-granite sites. The first set includes sites 101 to 107 (Fig. 7.3a) while the second set includes sites (109-112) across the SE portion of the granite (Fig. 7.3b). A comparison of Figures 7.3 a and b emphasises the different mean orientations that exist between the two sets of sites. A comparison between the azimuths GM and GE for each set reveals that the azimuths are skewed from orthogonality. Such orthogonality (or parallelism) would be required if both types of azimuth were influenced by the same, simple 2-D geoelectric contrasts. This is clearly not the case and an unambiguous interpretation is not possible.

The distinctive difference between the two sets of sites in both the Z and E field azimuths, are a continuation of differences observed at higher frqeuencies. These observations together with the differences in Z and E field magnitudes and slight differences in the vertical resistivity profiles all indicate that the SE portion of the outcrop has a distinctive geoelectric fabric in relation to the more westerly portion. In this regard it is worth noting the 'splay' apparent in the main NW-SE lineament orientations as they enter the SE portion of the granite (see Fig. 3.4).

8. INTERPRETATION OF THE VERTICAL CRUSTAL SECTION

The dimensional information considered in section 5.4 revealed that the sounding data on the granite possess a strong 1-D influence. This information alone testifies to the overall 'homogeneity' of the granite mass defining the Carnmenellis outcrop. The validity of the 1-D results presented in section 5.7 is thought to be very high, particularly for the upper 12 km of the crustal section. The two off-granite soundings provided strong 2-D and 3-D influences so a recovery of their complete vertical profiles is not simple.

Resolution within the upper 1 km is limited and the profiles presented in section 5.7 concentrate on the upper 10 km of immediate interest. The transition of resistivity values that occurs in the middle crustal section below 15 km is only noted in the transform results of Figure 5.9 and further work is required to identify and resolve this deep feature.

The overall set of solutions provide a very consistent profile of the deep resistivity structure of the Carnmenellis granite. Typical resistivities at a depth of 1 km are in the range 1000 to 2000 ohm.m. The resistivity increases slowly with depth reaching values approaching 10,000 ohm.m

at a depth of 10 km. Although the resolution of such a small but steady increase is difficult, maximum resistivity levels are apparent in the depth range 4 to 6 km. The observed resistivity values correspond to a 'wet' granite saturated with several weight-percent of water; a mechanism that is maintained down to at least 10 km.

Thermal control of resistivity does not appear to be the dominant mechanism. It has been suggested (section 6.2) that the pressure dependence of resistivity must account for the observed increase in resistivity with depth. Refinements to the interpretation are difficult since most laboratory analyses deal only with uniaxial pressure i.e. lithostatic load. It has been pointed out that a horizontal deviatoric stress field may exist at depth although its magnitude and variation with depth is unknown. A more specific examination of the physical controls actually operating in the Carnmenellis granite (e.g. jointing and stress) is undertaken in the next section.

The results presented in section 6.2 identify a slight difference in the vertical profiles between the western and the SE portion of the granite. The resistivity profiles in the SE appear displaced to moderately higher values.

Of direct interest to the interpretation of the upper crustal section are the wide-angle seismic reflection results of Brooks et al. (1984). Line 4 crossing the Carnmenellis outcrop observed two reflectors (R1,R2) above the Moho. The shallowest reflector (R1) was observed at a depth of about 7 to 8 km and appears to be confined to the granite. The model reflector R1 defines the upper surface of a low-velocity zone which extends to the second reflector (R2) in the depth interval 12 to 15 km. The interpretations considered by Brooks et al. (1984) were confined to the nature of the horizons rather than the nature of the low velocity zone which defines the horizons. The most direct 'interface' comparison is with the minimum-norm, layered resistivity profiles of Figure 5.14. For these solutions individual layer parameters which involve small resistivity contrasts are not likely to be significant. The solutions obtained do not reveal any spatially consistent major discontinuities across the vertical section. Instead we note that the depth interval of the low-velocity zone appears to be associated with an interval of approximately constant and maximum resistivity. We conclude no detectable geoelectric variations in rock/fluid properties can be identified at the depth associated with the R1 reflector. Thus R1 does not appear to represent a fractured zone with an associated enhancement of conducting fluids.

At a shallower crustal level there is some indication of a conductive layer/gradient at a depth of 1 km at sites in the immediate vicinity of a NE-SW conductive lineament. The anomalously low resistivity profile at one site (105) has also been correlated with the same lineament which appears to be a very localised feature. The lineament and associated alluvial fan must be considered to be a limited zone of enhanced fluid concentration.

The three sites above and around the HDR reservoir provide the most interesting results in the upper 5 km. The common resistivity profiles at two of the sites (one centrally above the reservoir and one displaced 500m) display a lower resistivity profile when compared with a third

site 1.1 km away from the central site. The two sites, 500m apart, provide a low-resistivity, reservoir-influenced section down to approximately 4.5 km. This depth appears consistent with the termination depth of the microseismic zone.

It should be noted that the relative resistivity contrast that corresponds to 'reservoir-influence' is small but nonetheless appears significant. In this regard it is likely to be a fluid-enhanced *volume* that controls the resistivity variations and other interpretation parameters confirm the low-resistivity zone is limited in spatial extent. Azimuthal orientations at the two reservoir-influenced sites display rapid rotations not observed elsewhere. The rotations culminate in a reversal of the vertical magnetic field between the central and 1.1 km distant third sites. This reversal therfore defines a localised 'edge-effect' of the low-resistivity reservoir.

9. PHYSICAL CONTROLS ON THE RESISTIVITY VARIATIONS

The results presented have provided approximate 1-D models (0 to 10km) across the Carnmenellis granite and lateral variations in resistivity (resistivity anisotropy) have been mapped. Although the background to physical interpretation has been discussed in section 6, the relationships between the geoelectric anisotropy, the increase in resistivity with depth and the effects of jointing and stress-induced microcracks are now considered in detail. In particular we address the question of whether the results can provide diagnostic information as to the predominant physical mechanism. We are largely concerned here with pressure/stress dependent behaviour. When 'neglecting' the influence of temperature-dependent effects it is assumed, as indicated in section 6.1, that there exists a linear decrease in resistivity with increasing temperature (and hence depth) which generates a linear 'background' effect to the pressure/stress dependent behaviour discussed below.

The joint/fracture types of the Carnmenellis granite have been discussed by a number of authors. According to Heath (1985), two groups of joints are commonly observed at the surface. One group is near-vertical and the other is sub-horizontal. The steeply dipping joints normally occur in sets of parallel fractures perhaps 1m apart. Two sets at right angles to each other (forming a set) are commonly observed. Careful observation of many 'joints' reveals displacement of perhaps only a few mm. Where displacement has occurred, the discontinuity is a fault, though it may simply be a joint along which minor adjustment has taken place. Evidence for faulting on a larger scale in the Carnmenellis granite is to be found in the development of topographical linearity, commonly exemplified by the courses of river valleys. This 'general' observation is confirmed in our results by the identification of the spatially-localised conductive zone that appears correlated with a major alluvial fan.

According to Gregory and Durrance (1987), where a system of hydrothermal convective circulation operates in a well-fractured granite such as the Carnmenellis, the spatial distribution of these cells is likely to be closely tied to the distribution of major water-conducting features.

In this context, fractures include all classes of physical break within the granite, such as joints and faults, whether mineralised or barren. The pattern of jointing within the Carnmenellis is generally described by two sets of master joints trending NE-SW and NW-SE. The borehole information considered by Heath (1985) indicated that in the upper 200m the water-conducting fractures were dominantly orientated NW-SE, but below this zone the preferred orientations change with depth. Larger scale faults cutting the Carnmenellis generally run parallel to the master joints with the NW-SE trend dominant as shown in Figure 3.4. The NW-SE faults are part of a major series of strike-slip displacements which occur throughout southwest England (Dearman, 1963).

In addition to the joint characteristics the Carnmenellis possesses a strongly anisotropic residual stress configuration as discussed in section 6. The maximum horizontal stress direction is orientated approximately NW-SE with the minimum horizontal stress orientated NE-SW and an intermediate vertical overburden stress. As a result, on uplift, fractures which trend approximately NW-SE will open, while NE-SW fractures remain closed. The asymmetry is apparent in the fluid flow systems described by Gregory and Durrance (1987).

A summary of the strike directions of the two master joint sets (JOINT SETS 1 and 2) is shown in Figure 9.1 (from Green et al., 1987). Also shown in Figure 9.1 are the maximum and minimum principal stress directions. Since the principal stress directions differ from the azimuths of the two joint sets, it may be possible to use these as constraints in relation to the observations of resistivity anisotropy.

Using the previous examples of control of resistivity anisotropy (section 6) we could anticipate two distinct effects. If simple and spatially persistent jointing controls the resistivity anisotropy we would expect maximum resistivity azimuths to be perpendicular to the direction of the major fluid-filled joints. Thus if a NW-SE joint set is the major fluid-filled feature within the granite the azimuth of maximum resistivity would be NE-SW. If however the resistivity anisotropy is controlled by microcracks we would anticipate maximum and minimum resistivity azimuths to be controlled by the principal stress directions, as discussed in section 6.

The rotational characteristics of the results have been discussed in section 5.6. The azimuths of maximum resistivity display a characteristic rotation with penetration depth. To provide diagnostic information on the possible influences, the azimuths of maximum resistivity are shown in relation to the joint/stress directions in Figure 9.2 for three frequencies (penetration depths). At the first frequency (89.5 Hz, Fig. 9.2a), penetration depths range from 832 m (at site 106) to 1686 m (at site 110). For the second frequency (8.95 Hz, Fig. 9.2b), penetration depths are predominantly in the range 3 to 6 km and for the third frequency (0.089 Hz, Fig. 9.2c) penetration depths are greater than 25 km.

The directions of maximum resistivity shown in Figure 9.2a show reasonably consistent orientations that are predominantly parallel to JOINT SET 2 (60 to 90 degrees). This suggests

that within the upper 1.5 km, resistivity may be controlled by joint (c.f. stress) related effects. In this case the predominant fluid-filled joint system would have a strike approximately parallel to JOINT SET 1. The results shown in Figure 9.2b refer to a much deeper penetration radius of between 3 and 6 km. The counterclockwise rotation is part of a continuous rotation with increasing penetration radius. The main conclusion from Figure 9.2b is that there is no evidence of any alignment with the principal stress directions. Increasing the penetration radius beyond 25 km (Fig. 9.2c) provides a reasonably consistent set of azimuths which again do not display any alignment with the principal stress directions. There *appears* rather to be a correlation between the azimuths of maximum resistivity and the strike direction of JOINT SET 1. It must be noted however that this correlation may be 'coincidental' since the anisotropy at this radius refers to a substantial volume of the granite and root batholith. As discussed in section 7, this direction is also approximately normal to the main set of thrust faults across the area and an unambiguous 'regional' interpretation is not possible using the results of a spatially-limited experiment.

The overall conclusion of the results presented is that the principal direction of resistivity does not display any alignment with the principal horizontal stress directions. Therefore the mechanism of aligned microcracks does not appear to control the observed geoelectric anisotropy. The results of Figure 9.2a suggest instead that within the upper 1.5 km (at least), resistivity is controlled by the principal joint system. The results indicate that the predominant fluid-filled joint system is coincident with JOINT SET 1 i.e. it is the fracture-system parallel to the NW-SE master joints that is 'open'. The results are therefore compatible with the NW-SE trending belts of enhanced groundwater flow noted in the results of Gregory and Durrance (1987).

We now turn to the more difficult task of assessing the mechanism which controls the depth-dependence of resistivity behaviour. Once again we cannot separate the two likely influences (joints or microcracks) without additional constraints or assumptions. We first note that there appear to be no stress-related effects in the observations of geoelectric anisotropy, as discussed above. Instead we observe joint-control in the upper 1.5 km. Information (from geoelectric anisotropy) at greater depths appears to be restricted by the possibilty of 'intermediate' rotations as the volume of the sounding increases and other 'regional' effects become more dominant.

In the discussion of the vertical resistivity profiles (section 8) it was noted that below 2 km the resistivity increases slowly with depth attaining maximum resistivity values in the depth range 4 to 6 km. We can use an estimate of 6 km as a 'lower' depth bound for the attainment of maximum resistivity across the whole Carnmenellis granite (see Fig. 5.19). We can initially make two observations. The first is that the physical mechanism producing the depth-dependence appears spatially consistent from west to east across the granite. In addition the physical control of the maximum resistivity also appears as a uniform property of the granite. Considered in isolation, however, the observations do not provide any constraints as to the operative

mechanism. To achieve additional constraints we must consider laboratory experiments, some of which have been reviewed in section 6. The two main difficulties here are that the laboratory samples (and experiments based on them) do not readily include jointing effects and in addition studies of deviatoric (anisotropic) stress influences have not been included in the majority of experiments.

The deep observations of jointing characteristics within the Carnmenellis granite are obviously limited to borehole information. We know from the Rosemanowes borehole logs that the jointing exists to at least 2.5 km and we can infer from the microseismicity that it persists to a depth of 4 km. The variation of the magnitude of the stress components is also known to a depth of around 2.5 km. These are shown in Figure 9.3, taken from Green et al. (1987). Clearly the observations must be extrapolated to provide deeper information. If we ignore all other possible effects then the linearly extrapolated stress magnitudes at a depth of 6 km are 180 MPa for the maximum horizontal stress, 150 MPa for the overburden stress and 80 MPa for the minimum horizontal stress.

The most relevant laboratory resistivity experiments to which such observations can be related are those of Trimmer et al. (1980) who studied the effect of pressure and stress on water transport in intact and fractured granite. Some conductance (i.e. normalised conductivity) measurements were made during the course of the experiments. The measurements were limited to pressure/stress magnitudes of less than 40 MPa (equivalent to depths of less than 2 km), but the results may have broader application. Trimmer et al. (1980) note that throughgoing fractures in Westerly granite dominate water transport, increasing the permeability by 6-9 orders of magnitude when compared with intact rocks. Observed changes in conductance, where available, mirror changes in permeability. Overall the data on both intact and *fractured* rock are consistent with previous experiments of crack closure and dilatancy both with and without differential stress. The previous experiments referred to are those of Brace et al. (1968) and Brace and Orange (1968b), as discussed in section 6. The Brace model then appears to hold for fractured and stressed rock. The results suggest that although the response of fractured rocks is dominated by fracture closure, the observed response cannot be distinguished from that due to microcrack closure. It would appear then that the depth dependence of resistivity cannot readily identify the depth to which the joint/fracture system extends.

One final observation can be used, however, to place the question of depth dependent mechanisms in perspective. This concerns the attainment of maximum resistivity at a depth of about 6 km throughout the granite. The fundamental resistivity/pressure dependence of low-porosity granitic rocks has been summarised in Figure 6.2. According to the original work of Brace et al. (1965) and all other subsequent experiments, the point of inflection between the initial non-linear response and the subsequent high-pressure linear response corresponds to the transfer from crack-dominated behaviour to pore-dominated behaviour. According to Figure 6.2, the transition should be complete and all forms of cracks should be closed at pressures of 200 MPa. The extrapolated stress measurements of Figure 9.3 clearly approach this value at a depth

of 6 km which, in addition, also corresponds to the depth of maximum resistivity observed across the granite. The resistivity profiles obtained appear therefore to 'reflect' (i.e. are consistent with) the completion of crack closure at a depth of about 6 km and a transfer to a pore dominated resistivity mechanism below this depth. *Thus in very simplistic terms*, if a joint can be defined as a feature that is capable of 'closing' (and closed here means an inability to support ionic conduction of interstitial fluids) then the above observations suggest the absence of such joints below 6 km.

Thus, referring back to section 6, in electrical terms the Carnmenellis granite corresponds to Hot Wet Rock over the depth interval from 0 to 10 km. Several weight-percent of free fluids saturate the rock fabric over this depth range. The observed depth profiles of resistivity appear to have mapped the response of the granite to increasing applied pressure/stress with depth. The efficiency of crack closure (see Batzle et al., 1980) of the Carnmenellis granite appears consistent with laboratory studies on a wide range of other granites (see Fig. 6.2). Crack closure, here defined in electrical terms, appears complete by 6 km. Below this depth, fluids must be retained in open pore spaces.

10. RECOMMENDATIONS

It is hoped that the survey results presented and interpreted here will provide information on the extent to which the magnetotelluric technique can assist in mapping deep rock-fluid properties in three dimensions. The study has been specific to the Carnmenellis granite and the interpretation has concentrated on the critical depth range of Hot Dry Rock geothermal energy extraction within this granite. Interpretational benefits and insights would clearly be generated if results were to be obtained from other granites and across other deep geothermal environments within the U.K.

One of the more critical aspects of the broad geothermal programme within the U.K. has been to establish the variation of the thermal conductivity of deep crustal rocks. This is one of the key areas of uncertainty in the prediction of deep temperatures (Anon, 1987). It appears that the porosity and water content of a given rock provide the *primary* control on *both* the thermal conductivity (Roy et al., 1981) and the electrical conductivity of the rock. It is recommended that some research be directed into the formalism (i.e. both theory and applied methods) for translating deep resistivity profiles into equivalent thermal conductivity profiles to increase the accuracy and confidence in the prediction of deep temperatures. Preliminary tests using the deep resistivity profiles obtained in this study are very encouraging.

The interpretational capability of the sounding method used here is controlled by the frequency-bandwidth of the instrumentation, the spatial coverage achieved and by the data quality. The equipment available in the U.K. is limited in all three respects. It is recommended that capital investment in fully-portable, very broad-band instrumentation is required to provide surveys and interpretations of a comparable quality to those available elsewhere in Europe, in

north America and Japan.

11. ACKNOWLEDGEMENTS

It is a pleasure to acknowledge the friendly assistance of the many farmers of the Carnmenellis area who granted land-access during the fieldwork. Scott Finnie proved a very capable field-assistant and his fortitude is gratefully acknowledged. The staff of the Camborne School of Mines, Geothermal Energy Project at Rosemanowes Quarry provided facilities and advice for which we are grateful. Their faith in the applicability of the technique is much appreciated. The work described in this report was funded under a contract from the Camborne School of Mines, Geothermal Energy Project (Department of Energy). This report is published with the approval of the Director, British Geological Survey (NERC).

12. REFERENCES

Anon., 1987. Hot Dry Rock potential of the United Kingdom, Invest. Geotherm. Potent. UK., British Geological Survey.

Batzle, M.L., Simmons, G. and Siegfried, R.W., 1980. Microcrack closure in rocks under stress : direct observation, J. Geophys. Res., **85**, 7072-7090.

Beamish, D., 1986. Geoelectric structural dimensions : methods of estimation, old and new, Geophysics, **51**, 1298-1309.

Beamish, D., 1987. A comparison of AMT systems, GRG Report No. 87/14, British Geological Survey.

Brace, W.F., Orange, A.S. and Madden, T.R., 1965. The effect of pressure on the electrical resistivity of water-saturated crystalline rocks, J. Geophys. Res., **70**, 5669-5678.

Brace, W.F., Paulding, B.W. and Scholz, C., 1966. Dilatancy in the fracture of crystalline rocks, J. Geophys. Res., **71**, 3939-3953.

Brace, W.F. and Byerlee, J.D., 1967. Recent experimental studies of brittle fracture in rocks, in *Failure and Breakage of Rock*, American Institute of Mining, New York, 58-81.

Brace, W.F. and Orange, A.S., 1968a. Electrical resistivity changes in saturated rocks during fracture and frictional sliding, J. Geophys. Res., **73**, 1433-1445.

Brace, W.F. and Orange, A.S., 1968b. Further studies of the effect of pressure on electrical resistivity of rocks, J. Geophys. Res., **73**, 5407-5420.

Brace, W.F., Walsh, J.B. and Frangos, W.T., 1968. Permeability of granite under high pressure, J. Geophys. Res., **73**, 2225-2236.

Brooks, M., Doody, J.J. and Al-Rawi, F.R.J., 1984. Major crustal reflectors beneath SW England, J. Geol. Soc. Lond., **141**, 97-103.

Burgess, W.G., Edmunds, W.M., Andrews, J.N., Kay, R.L.F. and Lee, D.J., 1982. The origin and circulation of groundwater in the Carnmenellis granite : the hydrogeochemical evidence, Invest. Geotherm. Potent. U.K., British Geological Survey.

Constable, S.C., Parker, R.L. and Constable, C.G., 1987. Occam's inversion : A practical algorithm for generating smooth models from electromagnetic sounding data, Geophysics, **52**, 289-300.

Crampin, S., 1985. Evidence for aligned cracks in the Earth's crust, First Break, **3**, 12-15.

Crampin, S. and Atkinson, B.K., 1985. Microcracks in the Earth's crust, First Break, **3**, 16-20.

Dearman, W.R., 1963. Wrench faulting in Cornwall and south Devon, Proc. Geol. Assoc., **74**, 265-287.

Eggers, D., 1982. An eigenstate formulation of the magnetotelluric impedance tensor, Geophysics, **47**, 1204-1214.

Evans, C.J., 1987. Crustal stress in the United Kingdom. Investigation of the Geothermal Potential of the UK. British Geological Survey.

Fischer, G. and Le Quang, B.V., 1981. Topography and minimisation of the standard deviation in one-dimensional magnetotelluric modelling, Geophys. J. R. astr. Soc., **67**, 257-278.

Gamble, T.D., Goubau, W.M. and Clarke, J., 1979. Error analysis for remote reference magnetotellurics, Geophysics, **44**, 959-968.

Green, A.S.P., Baria, R. and Jones, R., 1987. Fault-plane analysis of microseismicity induced by fluid injections into granite, in *Engineering Geology of Underground Movements*, eds., Bell, F.G. and Cripps J.C., Proc. 23rd Ann. Conf. Engineering Group Geol. Soc., Nottingham University.

Gregory, R.G. and Durrance, E.M., 1987. Helium, Radon, and hydrothermal circulation associated with the Carnmenellis radiothermal granite of southwest England, J. Geophys. Res., **92**, 12567-12586.

Heath, M.J., 1985. Geological control of fracture permeability in the Carnmenellis granite, Cornwall: implications for radionuclide migration, Mineral. Mag., **49**, 233-244.

Johnson, D.L. and Manning, H.J., 1986. Theory of pressure dependent resistivity in crystalline rocks, J. Geophys. Res., **91**, 11611-11617.

Olhoeft, G.R., 1981. Electrical properties of granite with implications for the lower crust, J. Geophys. Res., **86**, 931-936.

Quist, A.S. and Marshall, W.L., 1968. Electrical conductances of aqueous sodium chloride solutions from 0 to 800° and at pressures to 4000 bars, J. Phys. Chem., **73**, 978-985.

Roberts, G. and Crampin, S., 1986. Shear wave polarisations in a Hot Dry Rock Geothermal Reservoir : Anisotropic effects of fractures, Int. J. Rock Mech. Min. Sci. & Geomech. Abstr., **23**, 291-302.

Roy, R.F., Beck, A.E. and Touloukian, Y.S., 1981. Thermophysical properties of rocks, in *Physical Properties of Rocks and Minerals*, eds. Touloukian, Y.S., Judd, W.R. and Roy, R.F., *McGraw-Hill/CINDAS Data Series on Material Properties, Vol. II-2*, 409-502.

Rummel, F., 1986. Stresses and tectonics of the upper continental crust : a review, in *Proceedings of the International Symposium on Rock Stress and Rock Stress Measurements*, ed., Stephenson, O., Stockholm, 177-186.

Schmucker, U., 1987. Substitute conductors for electromagnetic response estimates, Pageoph., **125**, 341-367.

Stesky, R.M., 1986. Electrical conductivity of brine-saturated rock, Geophysics, **51**, 1585-1593.

Travassos, J.M. and Beamish, D., 1988. Magnetotelluric data processing - a case study, Geophys. J., **93**, 377-391.

Trimmer, D., Bonner, B., Heard, H.C. and Duba, A., 1980. Effect of pressure and stress on water transport in intact and fractured gabbro and granite, J. Geophys. Res., **85**, 7059-7071.

Tzanis, A., 1987. Investigations on the properties and estimation of earth response operators from EM sounding data, unpublished Ph.D. thesis, University of Edinburgh.

Walsh, J.B., 1965. The effect of cracks on the uniaxial elastic compression of rocks, J. Geophys. Res., **70**, 399-411.

Walsh, J.B., 1981. Effect of pore pressure and confining pressure on fracture permeability, Int. J. Rock Mech. Min. Sci. & Geomech. Abstr., **18**, 429-435.

Weidelt, P., 1972. The inverse problem of geomagnetic induction, J. Geophys., **41**, 85-109.

Word, D.R., Smith, H.W. and Bostick, F.X. Jr., 1970. An investigation of the magnetotelluric tensor impedance method, Tech. rep. 82, Electr. Geophys. Res. Lab., Univ. of Texas at Austin.

Table 1. Summary site locations in National Grid coordinates (Reference SW) and site elevations in metres. Sites 101 to 303 form the sounding locations. Sites a to f identify six sounding locations aborted due to strong electric fence noise.

SITE	EASTING	NORTHING	ELEVATION (metres)
101	663	322	150
102	680	320	140
103	685	325	125
104	689	313	173
105	694	327	125
106	708	320	140
107	716	320	185
108	716	323	182
109	724	303	145
110	742	323	175
111	753	325	145
112	764	322	100
201	625	306	97
202	716	276	70
301	718	353	167
302	730	353	172
303	731	348	180

a	676	327
b	680	325
c	695	323
d	700	323
e	722	319
f	734	328

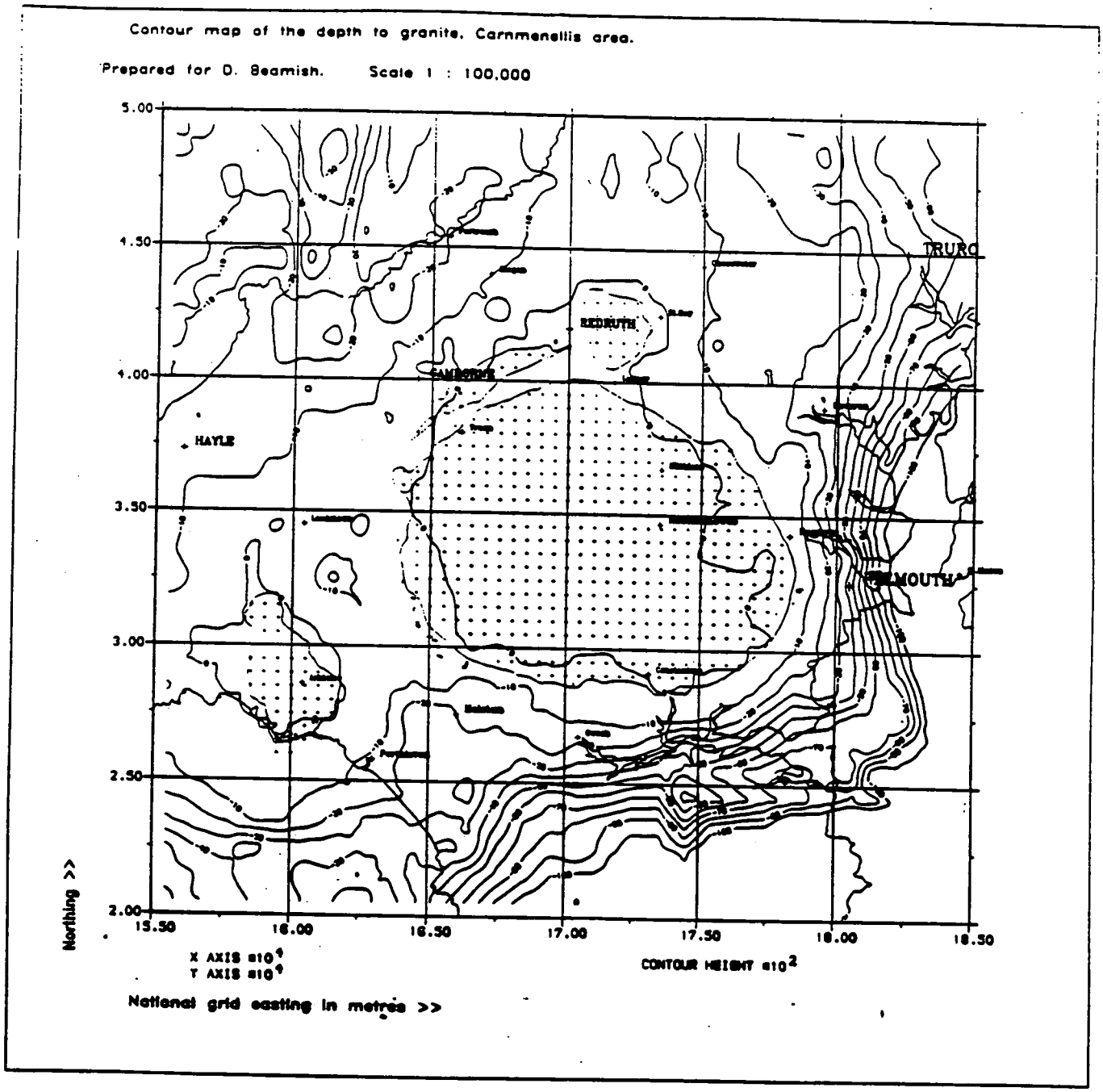

Figure 2.1. Contour map of depth to granite in the area of the Carnmenellis outcrop. Supplied by J. Willis-Richards (CSM/HDR).

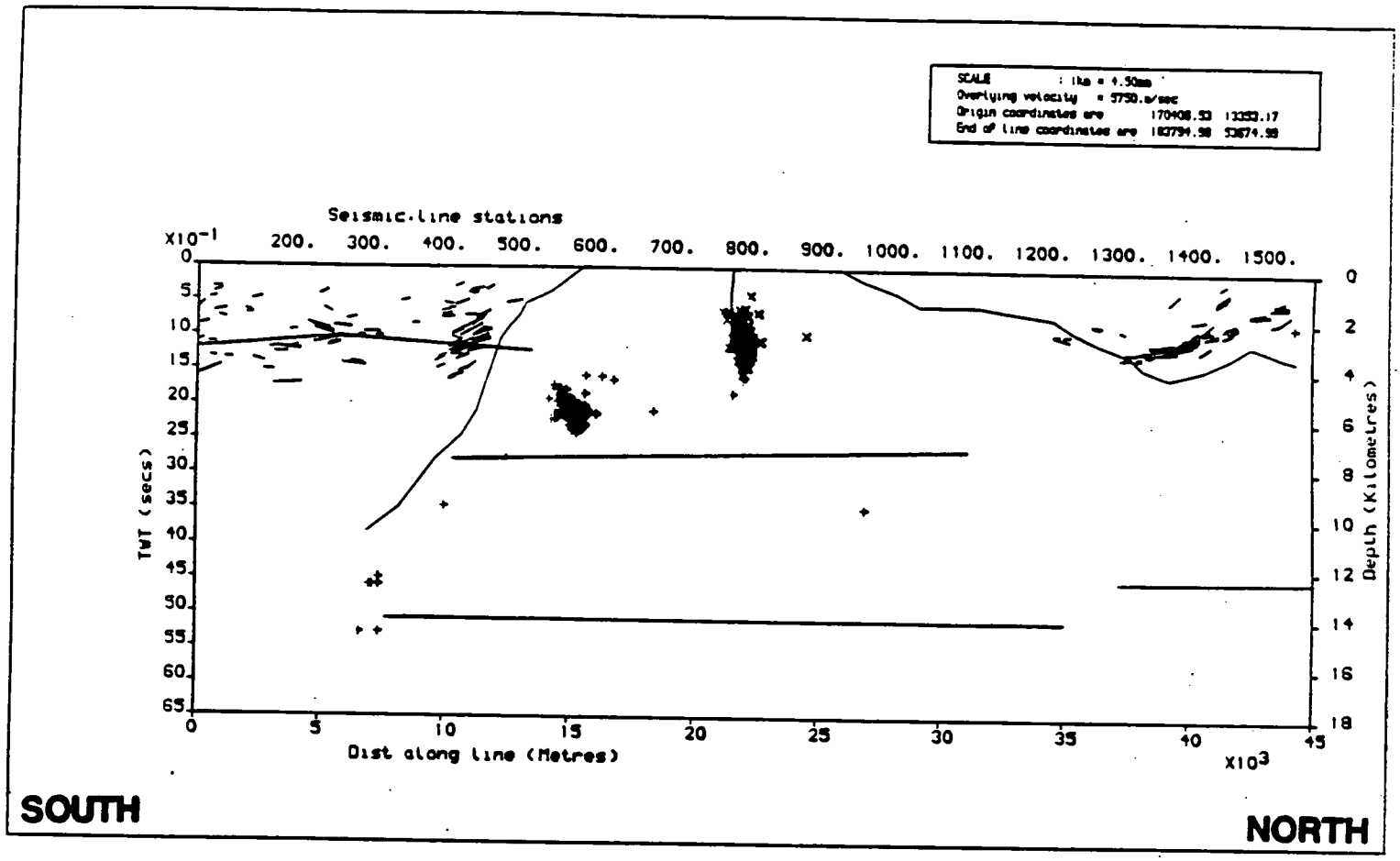

Figure 2.2. North-south geophysical section summary of the Carnmenellis granite. Section contains granite outline, seismicity (x = HDR hydrofracture, + = Constantine earthquakes), upper crustal reflectors and deep reflectors (R1,R2) from the seismic refraction experiment of Brooks et al. (1984).

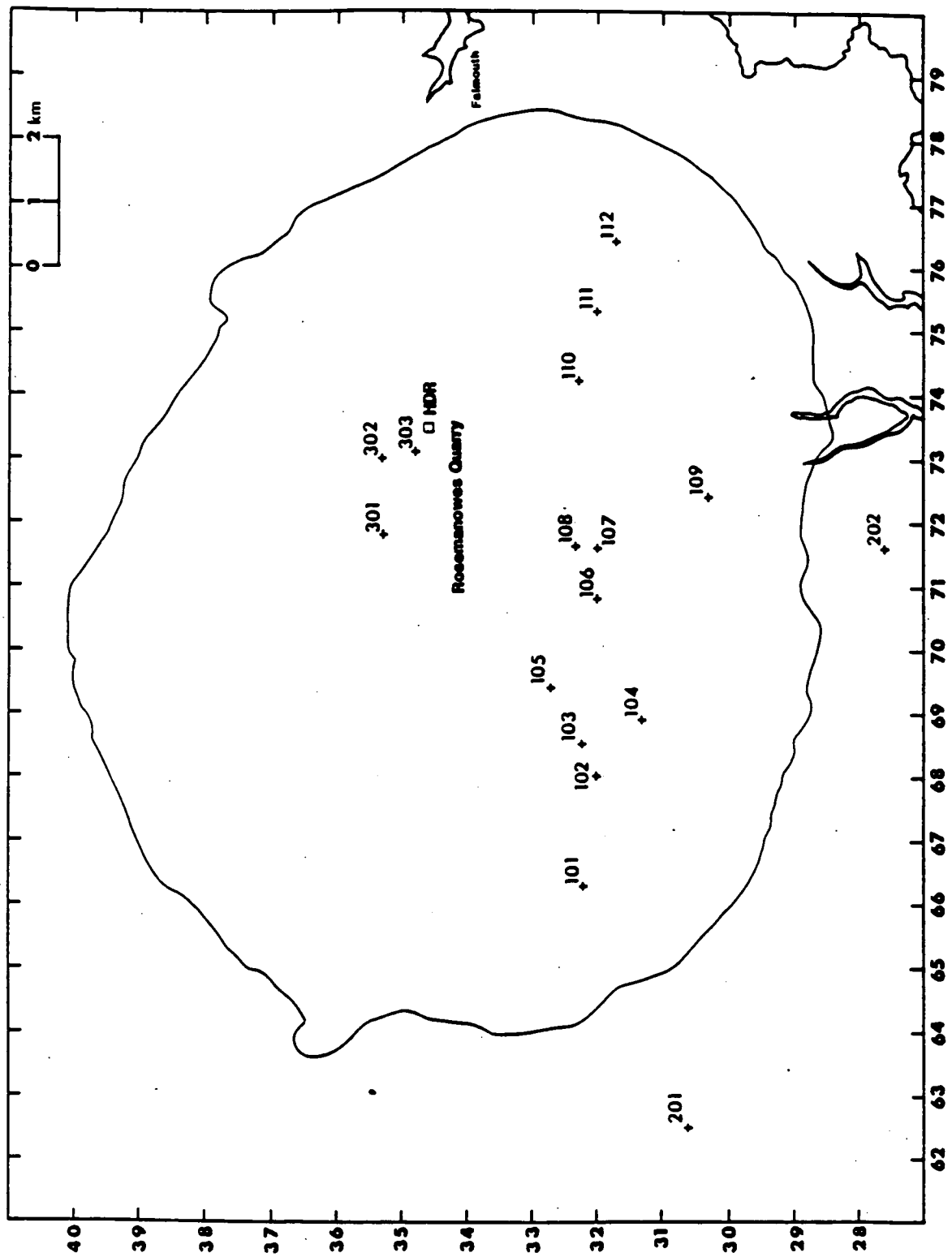

Figure 3.1. Seventeen sounding locations of the 1988 AMT survey of the Carnmenellis granite. Three sets of site groupings are shown. Sites 101-112 form the main E-W profile. Sites 201-202 are off-granite soundings. Sites 301-303 form a cluster above and around the HDR reservoir at Rosemanowes quarry.

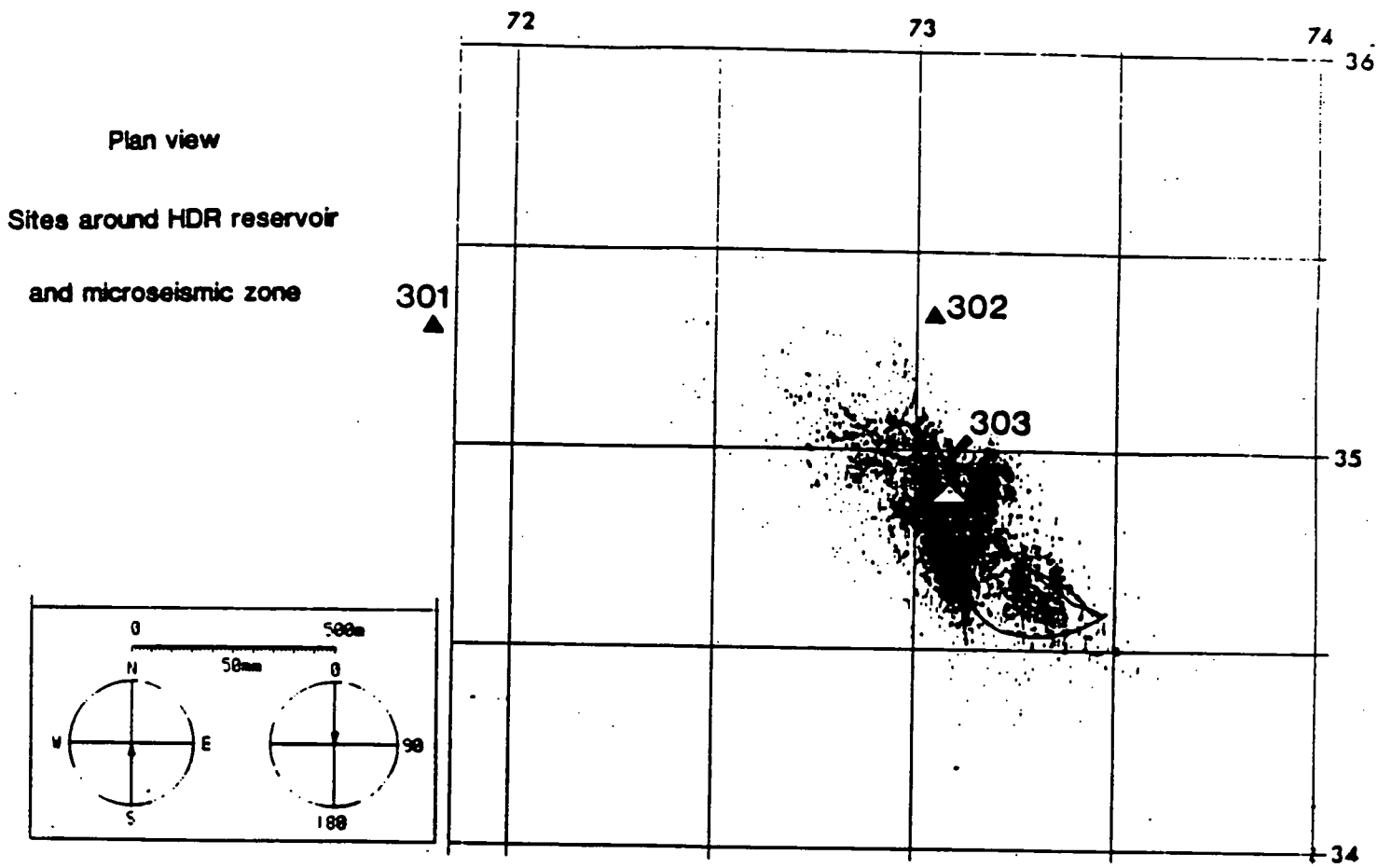

Figure 3.2. Detailed plan view of site locations 301 to 303 in relation to the microseismic zone associated with hydrofracturing at the HDR reservoir.

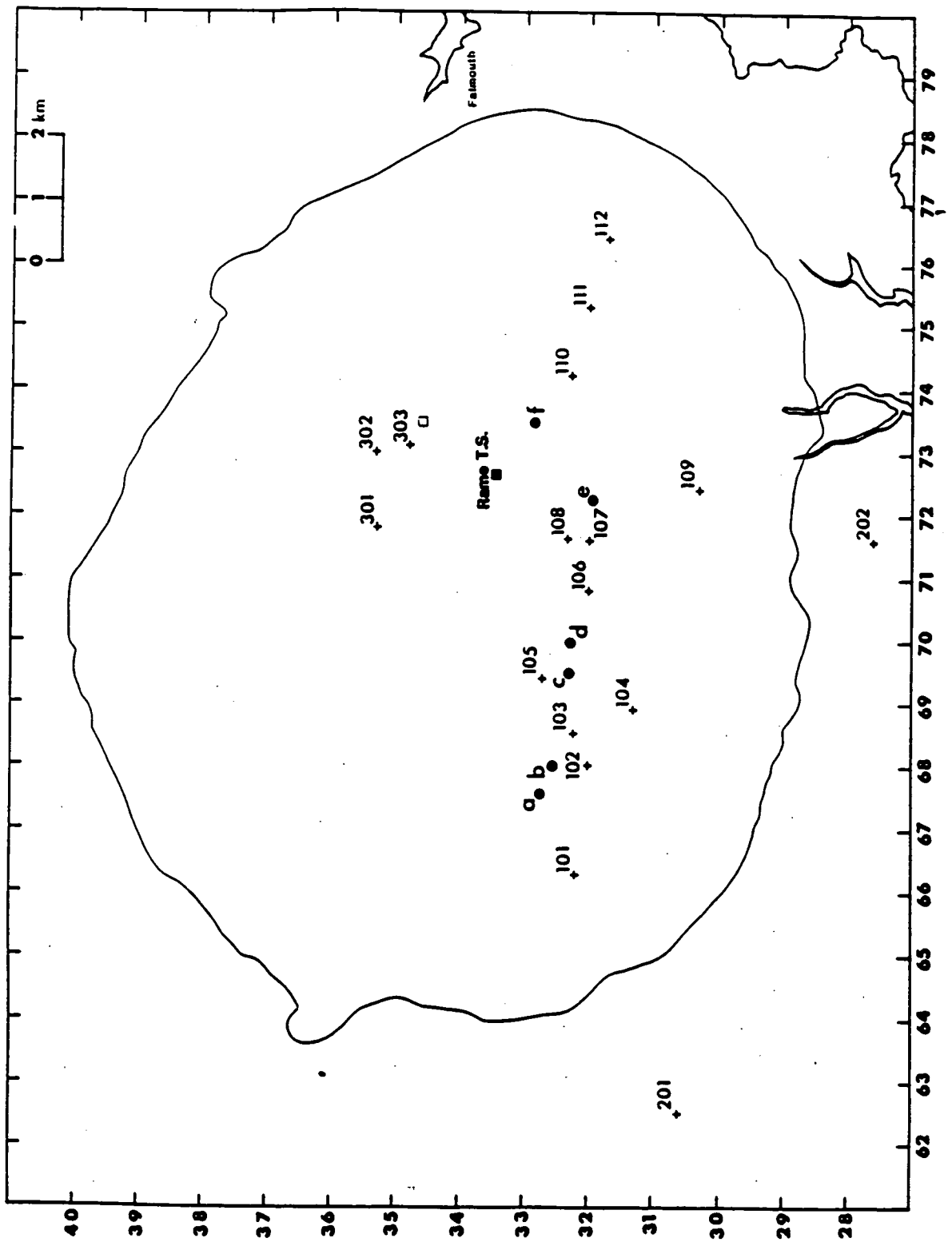

Figure 3.3. Sounding locations as in Figure 3.1 but showing sites (solid circles a to f) which had to be aborted due to electric fence noise. Rame Transformer Station (solid square) defines a major convergence of overhead electricity supply lines.

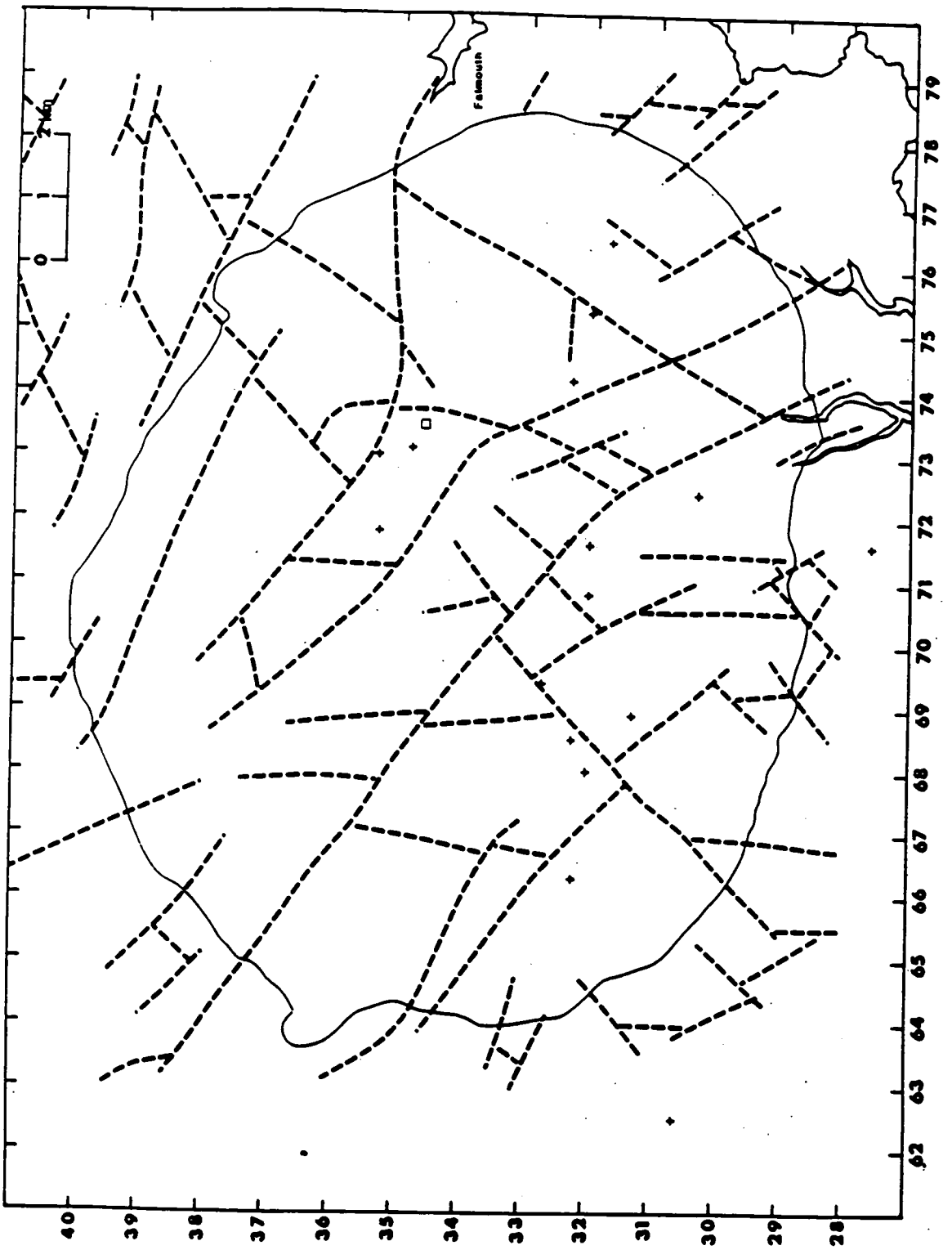

Figure 3.4. Major fracture lineations across the Carnmenellis granite from geological and topological maps and Landsat photographs. After Gregory and Durrance (1987).

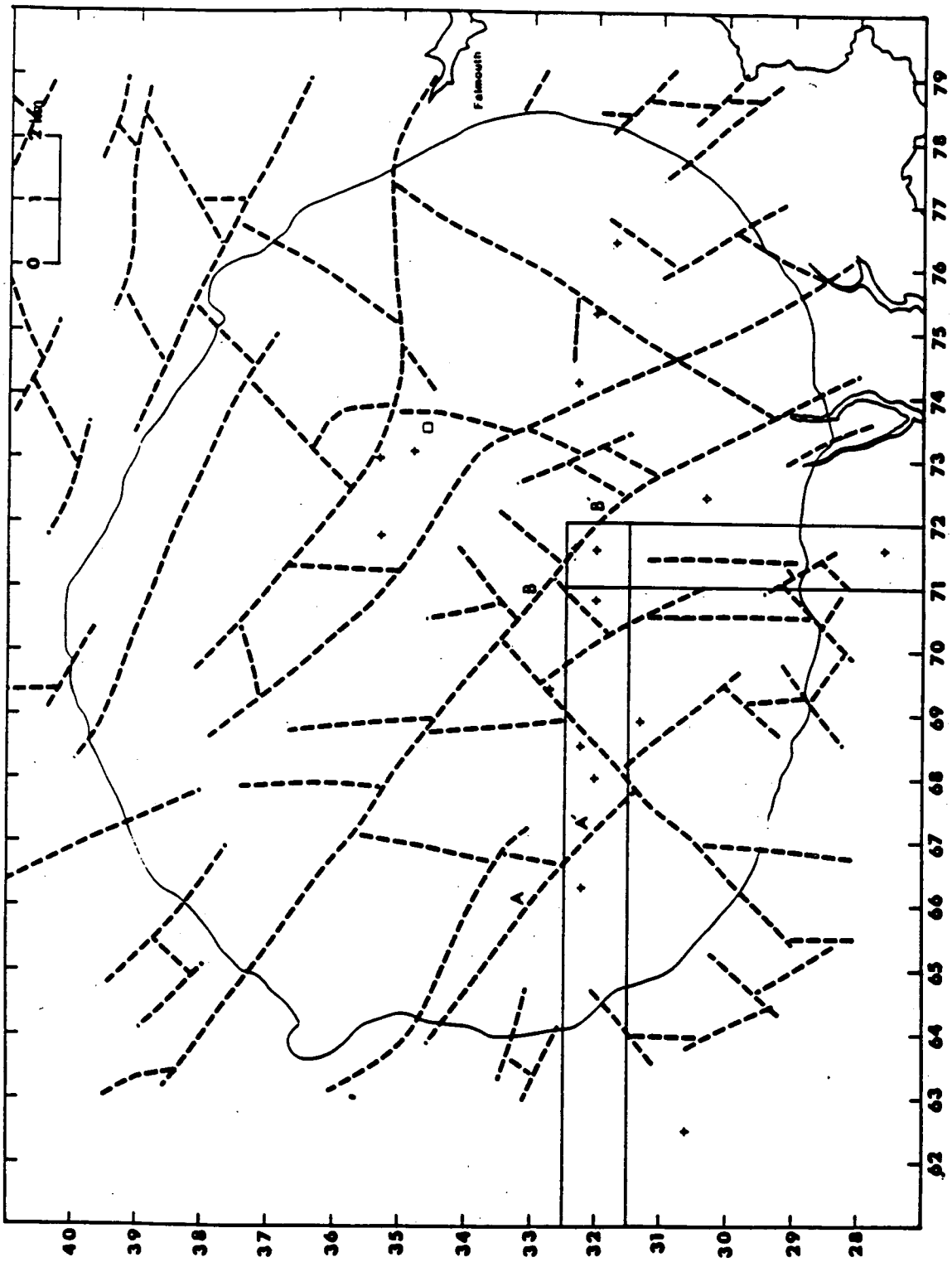

Figure 3.5. Outline lineation map of Figure 3.4 showing lineaments A-A' and B-B' considered during the survey. B-B' was chosen as the target lineament.

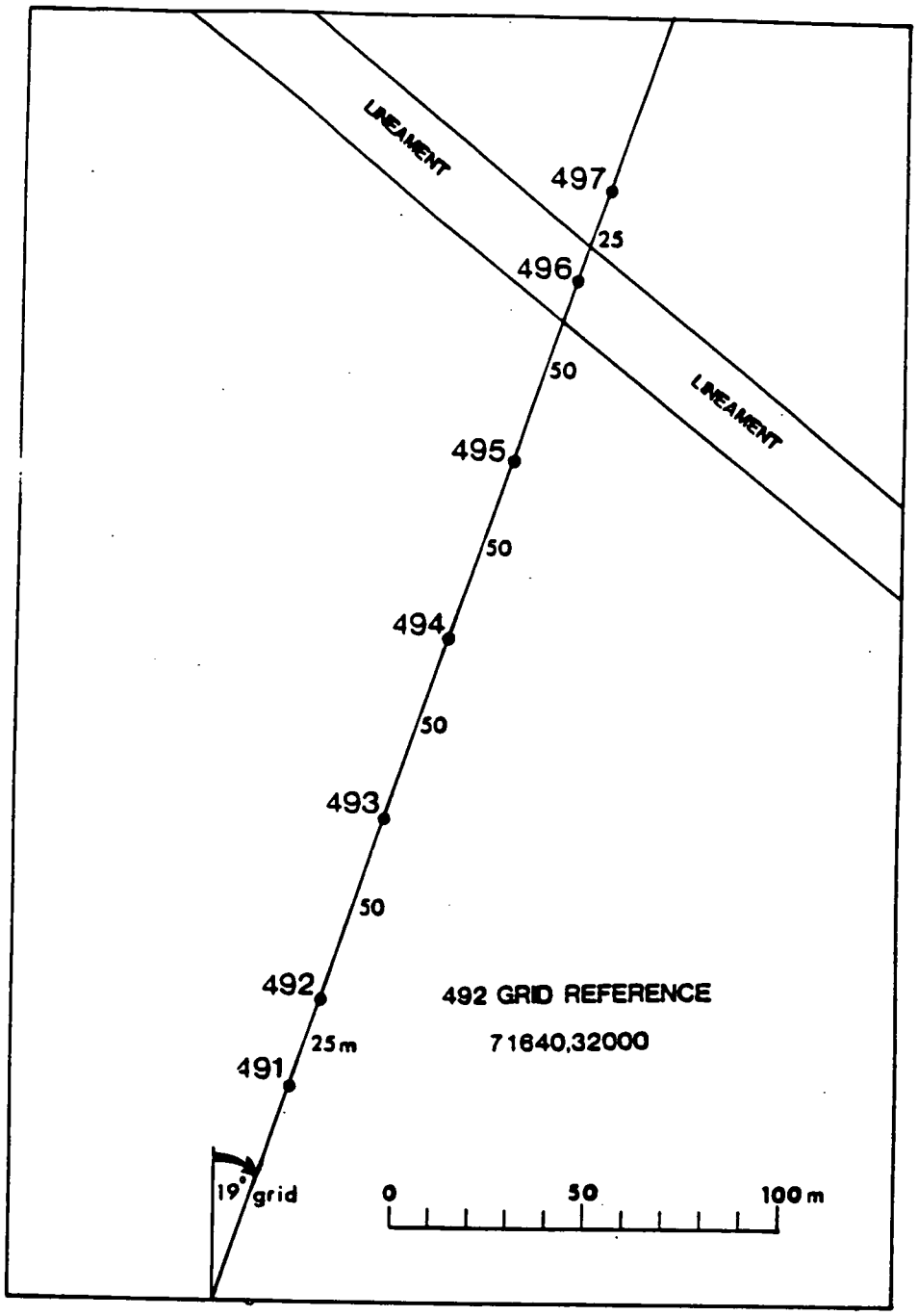

Figure 3.6. The seven sounding locations (491 to 497) of the lineament profile. See Figure 3.5 for larger scale.

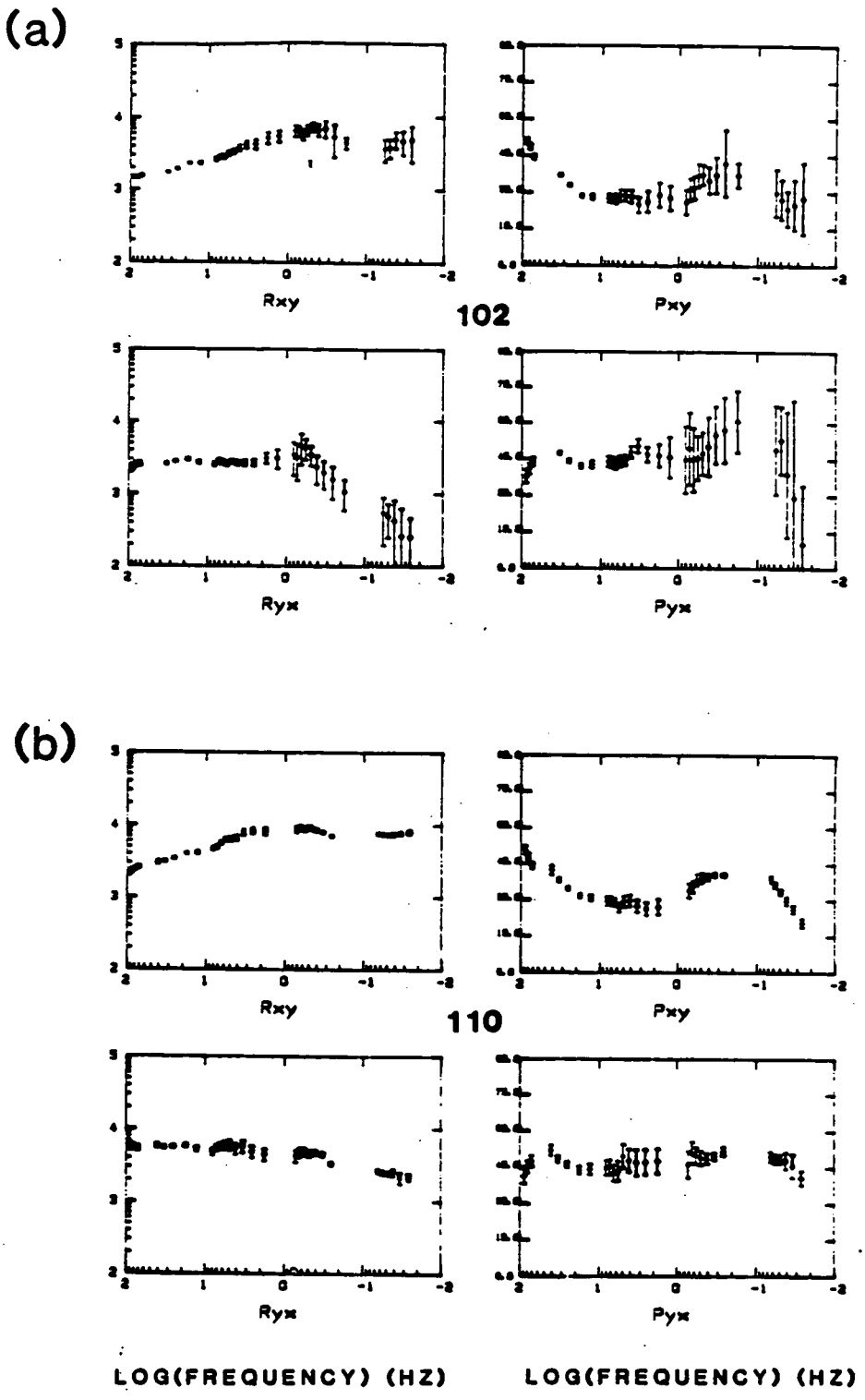

Figure 3.7. Four decade (10^2 to 10^{-2} Hz) resistivity sounding curves at sites (a) 102 and (b) 110. Apparent resistivities (R) are in measured directions (Rxy=north, Ryx=east) and are in ohm.m. Associated phases (P) are also in measured directions and are in degrees.

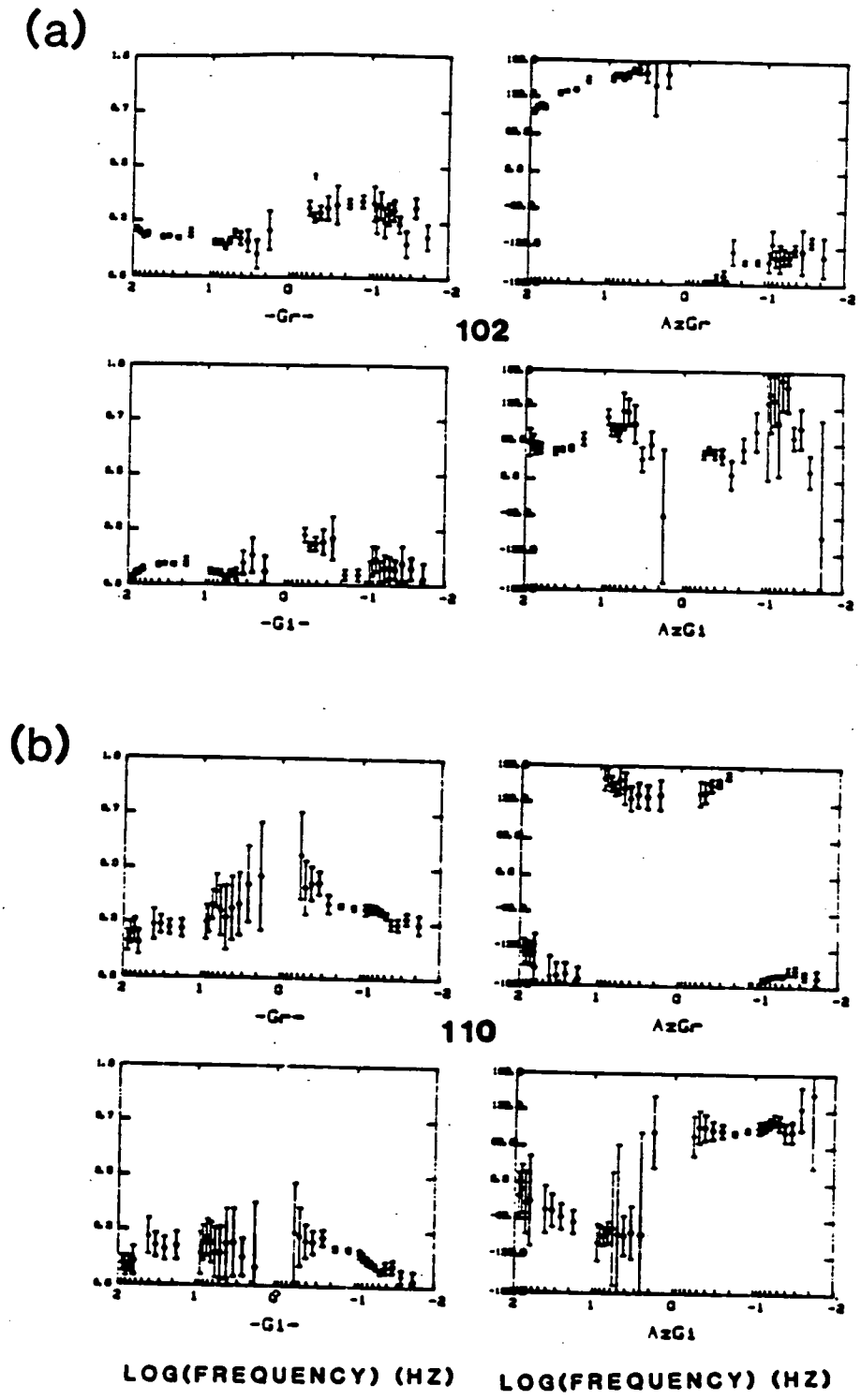

Figure 3.8. Four decade (10^2 to 10^{-2} Hz) vertical magnetic field sounding curves at sites (a) 102 and (b) 110. Gr, Gi are the amplitudes of the real (r) and imaginary (i) induction arrows and AzGr, AzGi are the associated azimuths of the real (r) and imaginary (i) induction arrows.

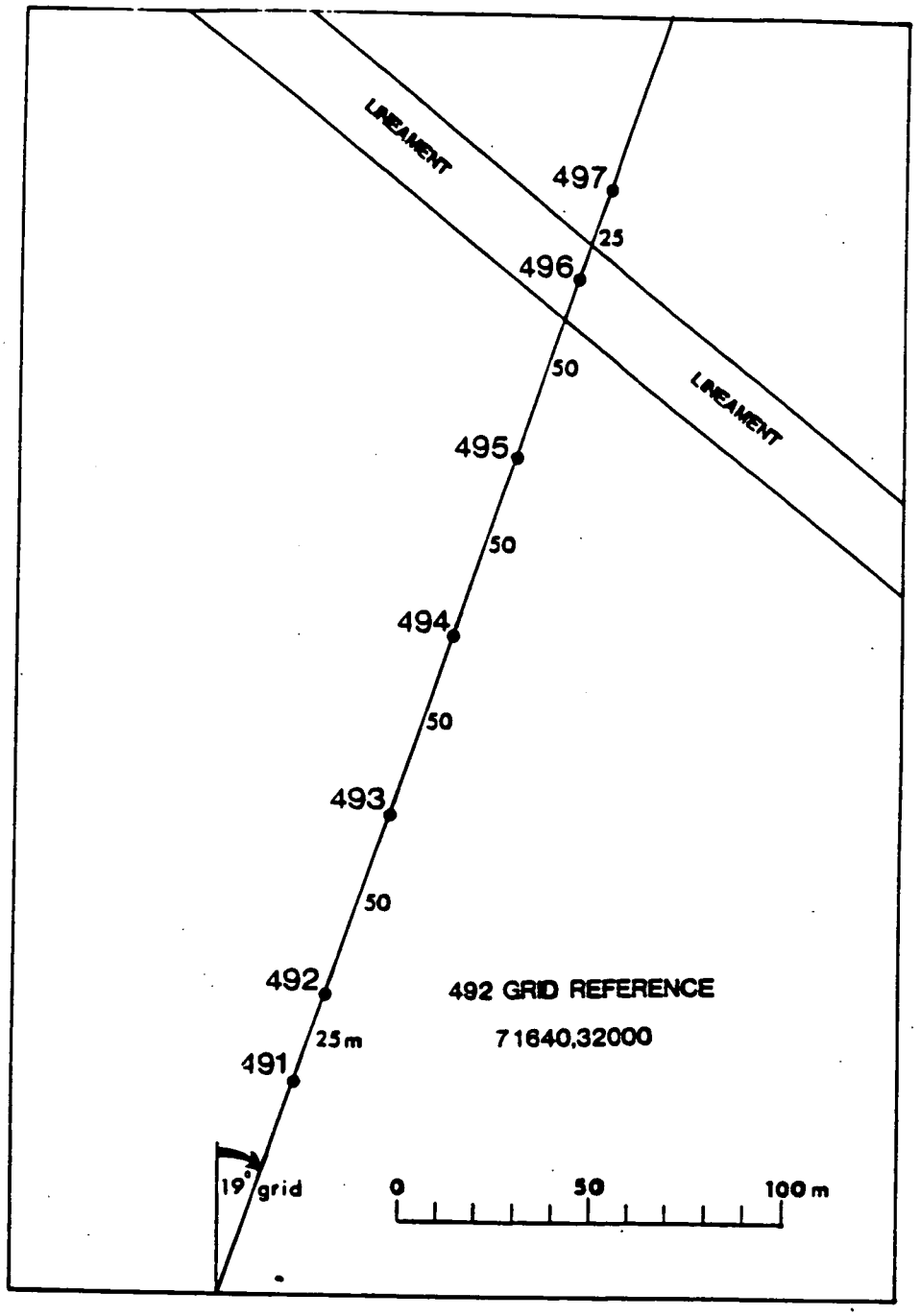

Figure 4.1. Lineament survey. Seven sounding locations (491 to 497) of the lineament profile.

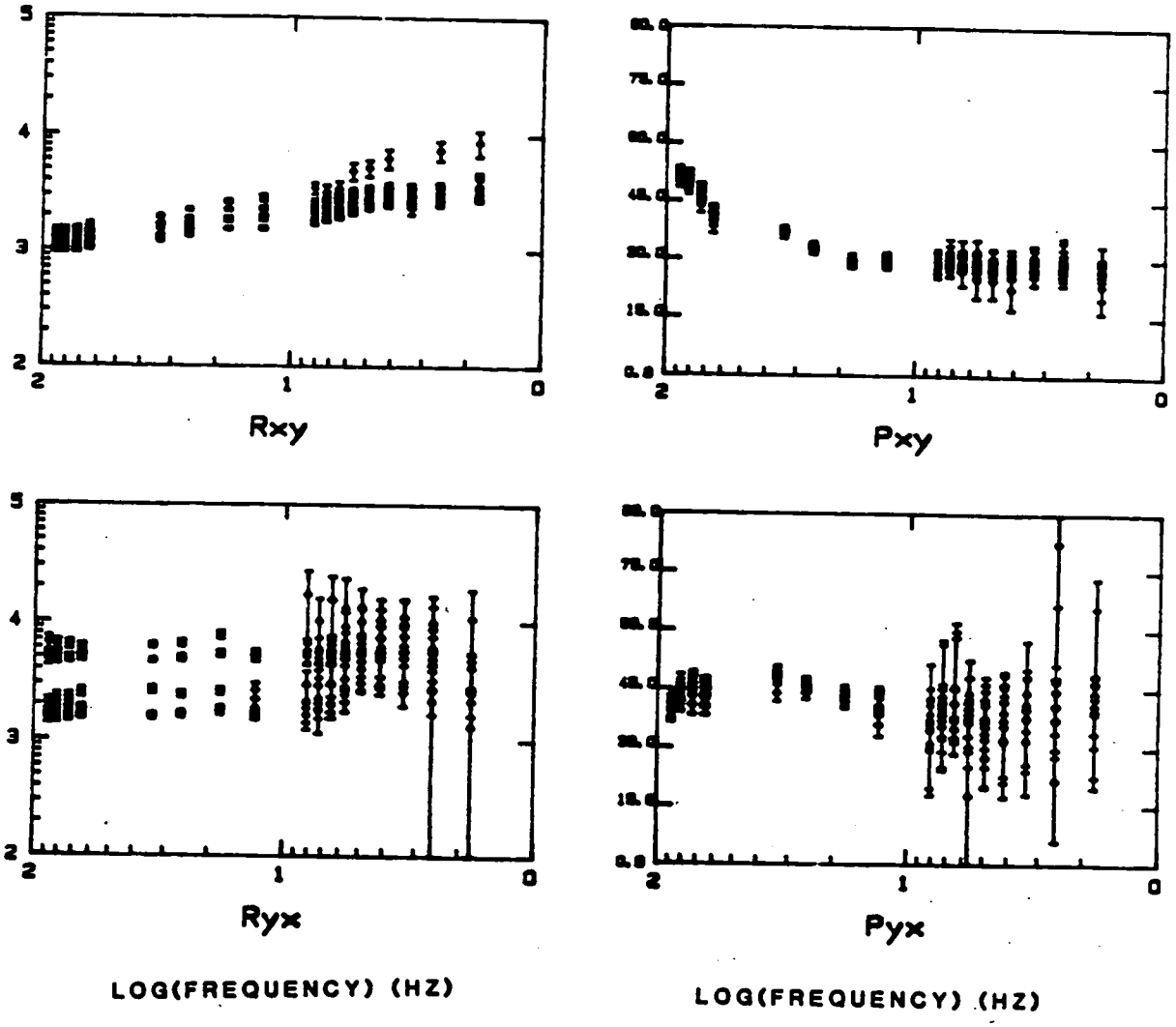

Figure 4.2. Lineament survey. Two decade (10^2 to 10^0 Hz) resistivity sounding curves for all seven soundings. Apparent resistivities (R) in measured directions (xy=north, yx=east) in ohm.m. Associated phases (P) in degrees. Error bars represent 95% confidence limits.

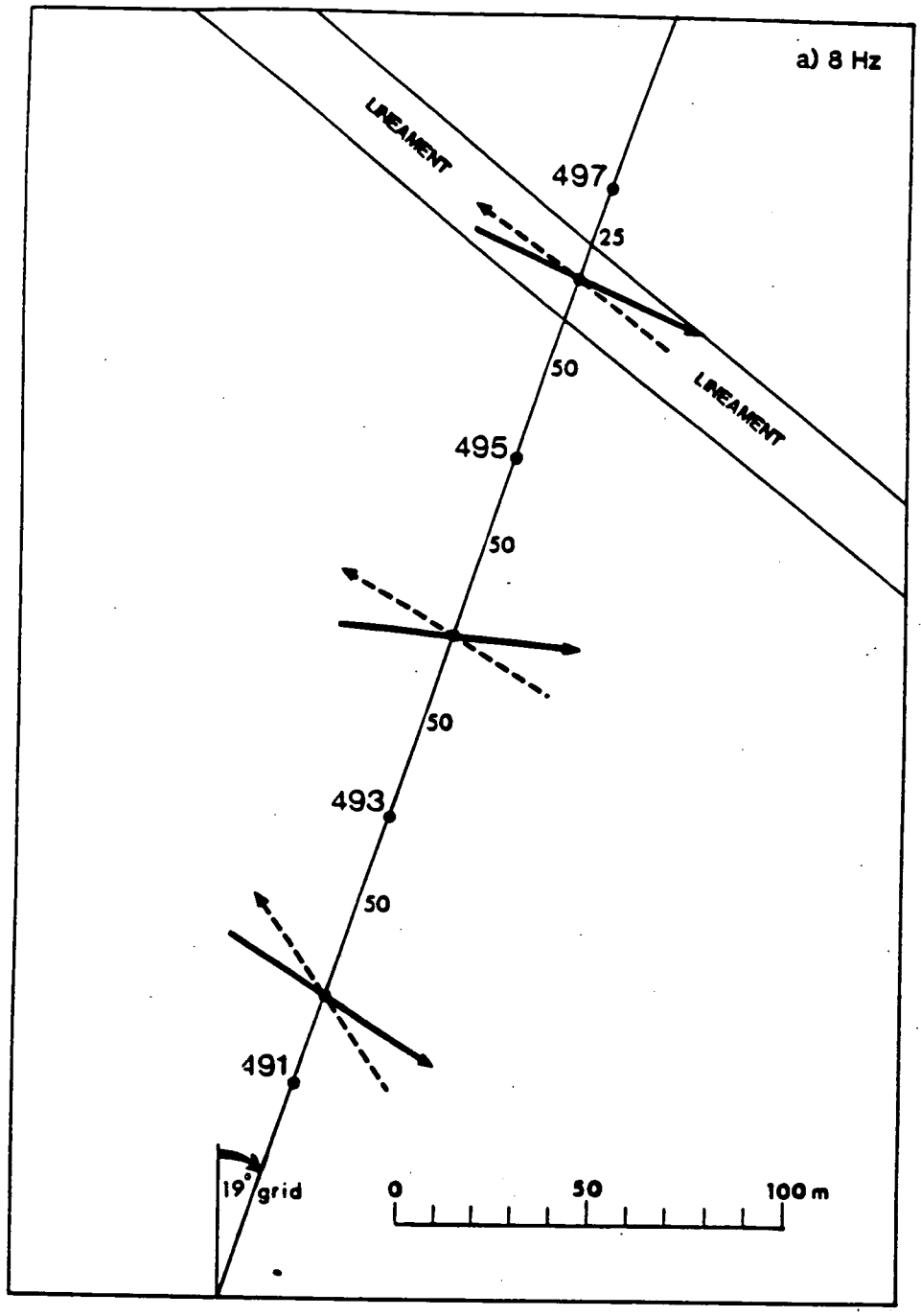

Figure 4.3. Lineament survey. Vertical magnetic field azimuths at two frequencies (a) 8 Hz and (b) 88 Hz. Solid arrows are real (in-phase) induction arrows, dashed arrows are imaginary (in-quadrature) induction arrows. Amplitude information ignored. Arrows should be perpendicular to geoelectric strike.

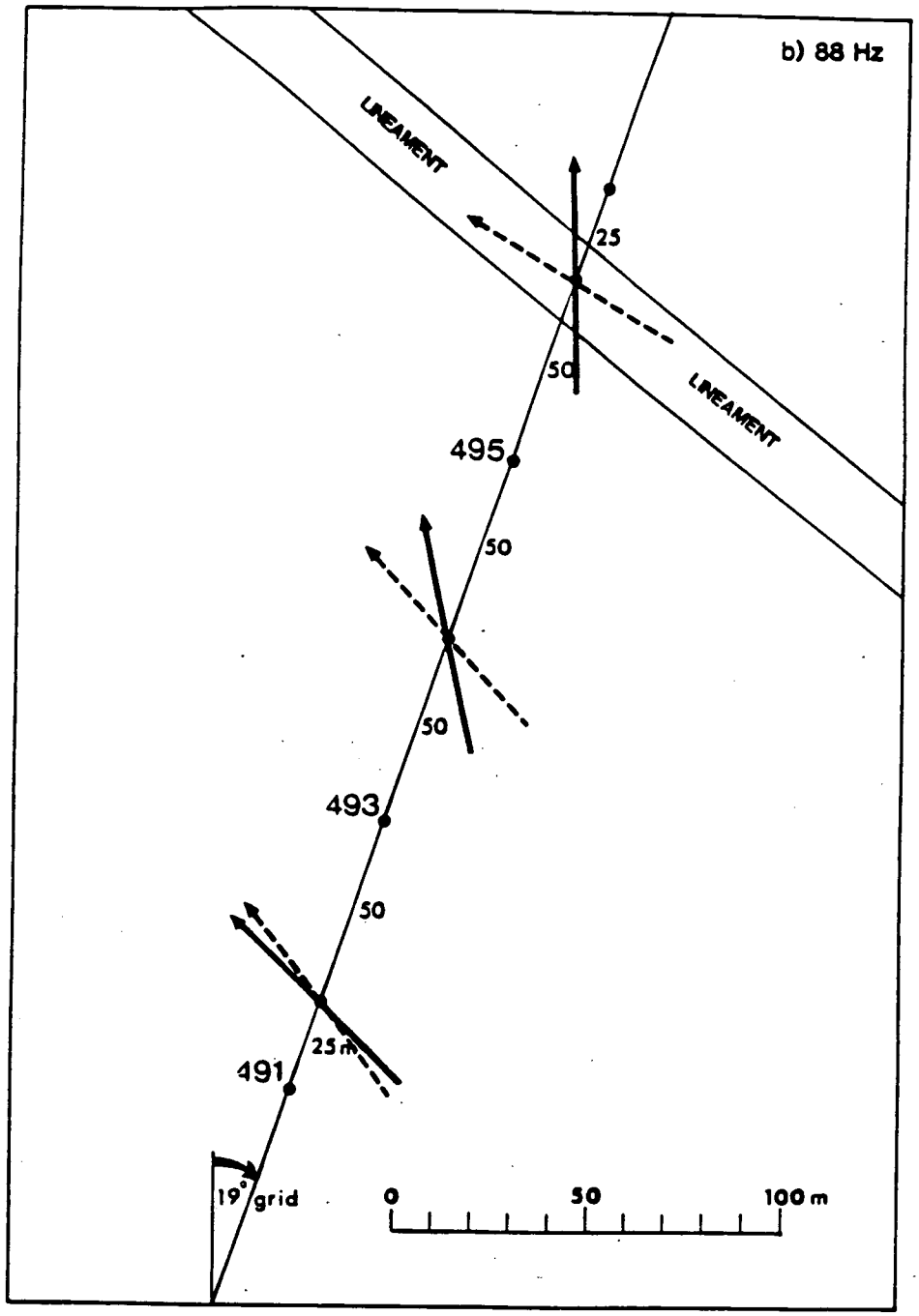

Figure 4.3. Lineament survey. Vertical magnetic field azimuths at two frequencies (a) 8 Hz and (b) 88 Hz. Solid arrows are real (in-phase) induction arrows, dashed arrows are imaginary (in-quadrature) induction arrows. Amplitude information ignored. Arrows should be perpendicular to geoelectric strike.

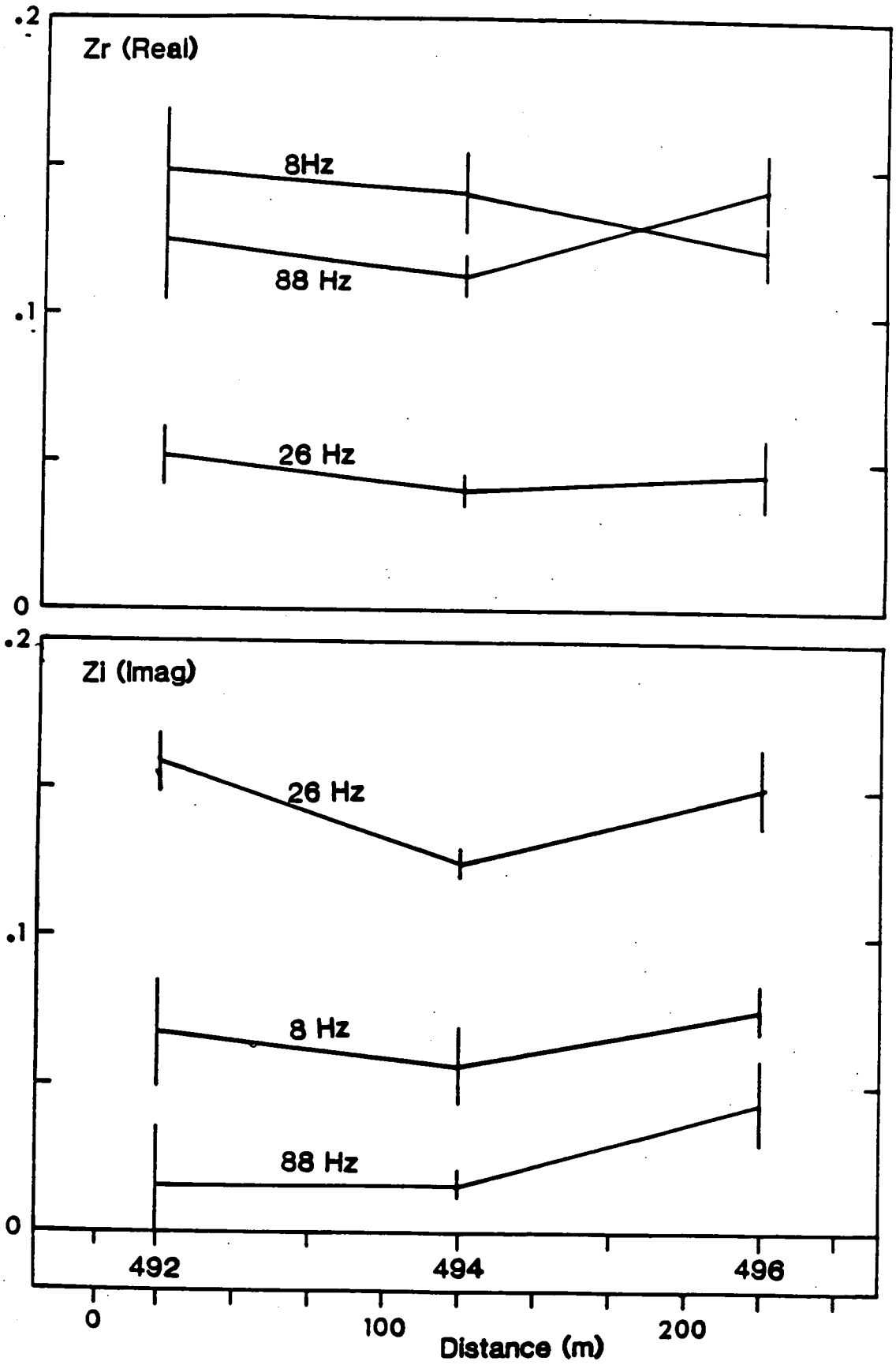

Figure 4.4. Lineament survey. Profile variation of amplitude of real (Zr) and imaginary (Zi) induction arrows at 8, 26 and 88 Hz. Error bars represent 68% confidence limits.

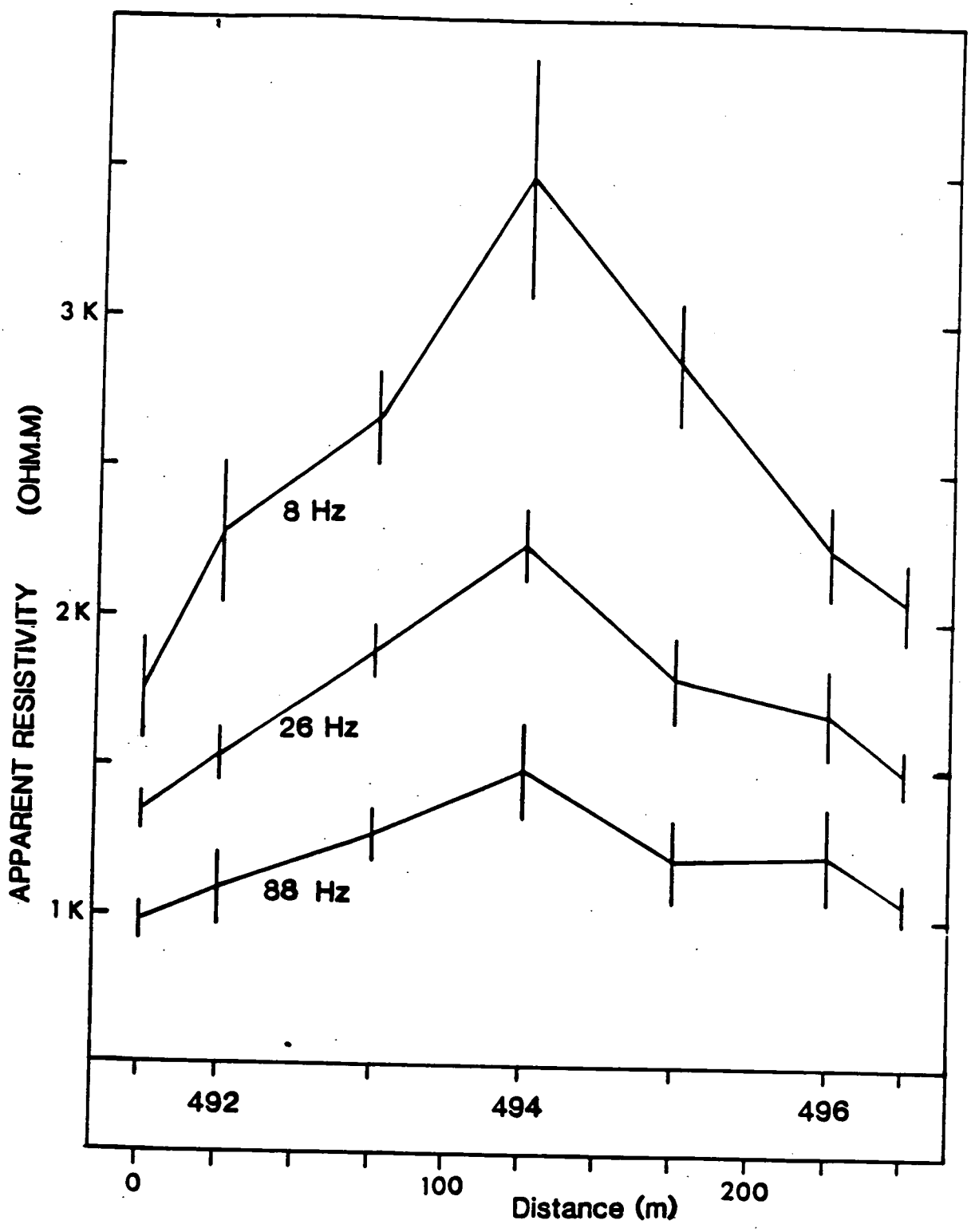

Figure 4.5. Lineament survey. Profile variation of (a) apparent resistivity and (b) phase in measured north direction, at 8, 26 and 88 Hz. K refers to 1000. Error bars represent 95% confidence limits.

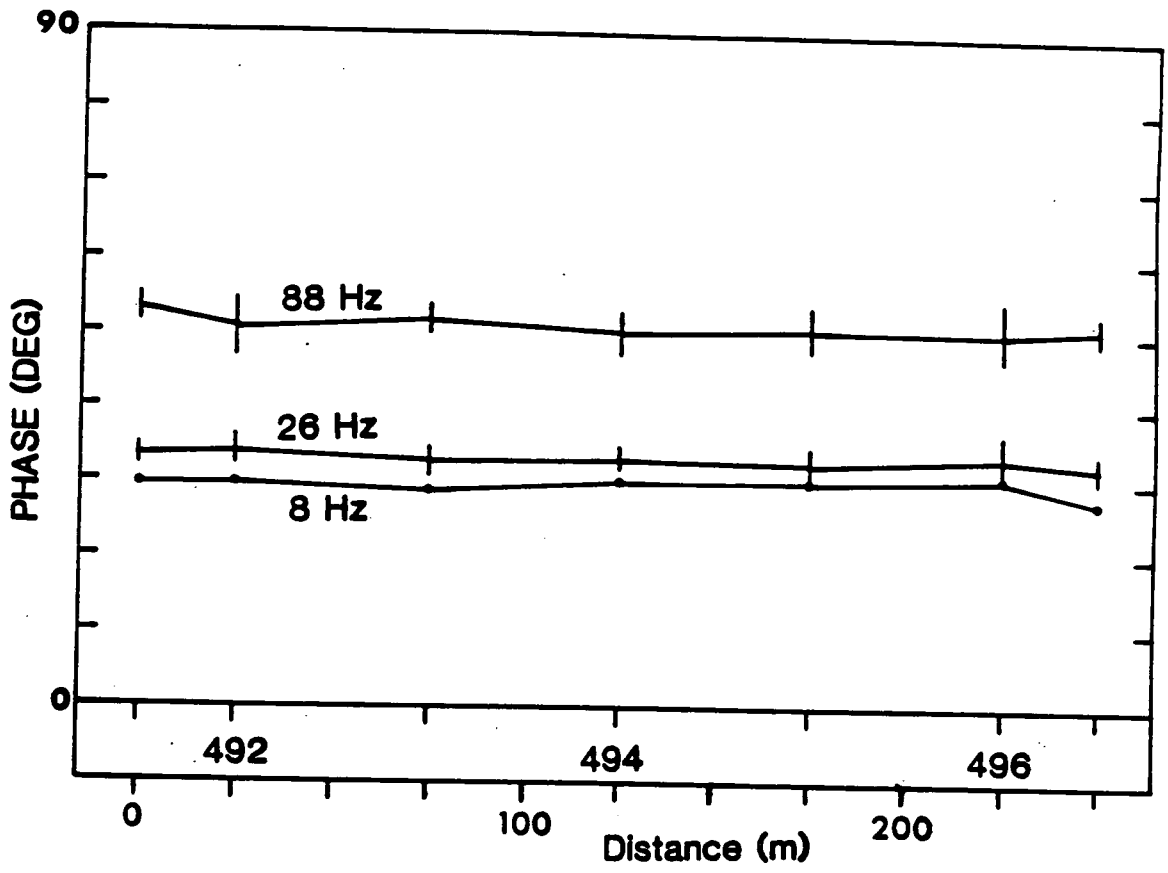

Figure 4.5. Lineament survey. Profile variation of (a) apparent resistivity and (b) phase in measured north direction, at 8, 26 and 88 Hz. K refers to 1000. Error bars represent 95% confidence limits.

THE BASIC RELATIONSHIPS OF MT

The basic realtionships take place in the frequency domain and involve the impedance tensor $\underline{Z}$. This tensor relates the induced electric field E to the surface magnetic field H at a sounding location. We write

$$\begin{bmatrix} E_x \\ E_y \\ \hline E_z \end{bmatrix} = \left[\begin{array}{cc|c} Z_{xx} & Z_{xy} & Z_{xz} \\ Z_{yx} & Z_{yy} & Z_{yz} \\ \hline Z_{zx} & Z_{zy} & Z_{zz} \end{array}\right] \begin{bmatrix} H_x \\ H_y \\ H_z \end{bmatrix}$$

or $$\underline{E} = \underline{Z} \cdot \underline{H}$$

$\underline{Z}$ contains 3D information about the geoelectric structure at a point. Its rotation properties convey information about the dimensionality of the structure and the geoelectric strike. The variation of $\underline{Z}$ with frequency (a sounding curve) provides depth information.

Conventionally the results are given as a variation of apparent resistivity/phase with frequency in one or more principal geoelectric directions.

Figure 5.1. The basic relationships of the magnetotelluric method.

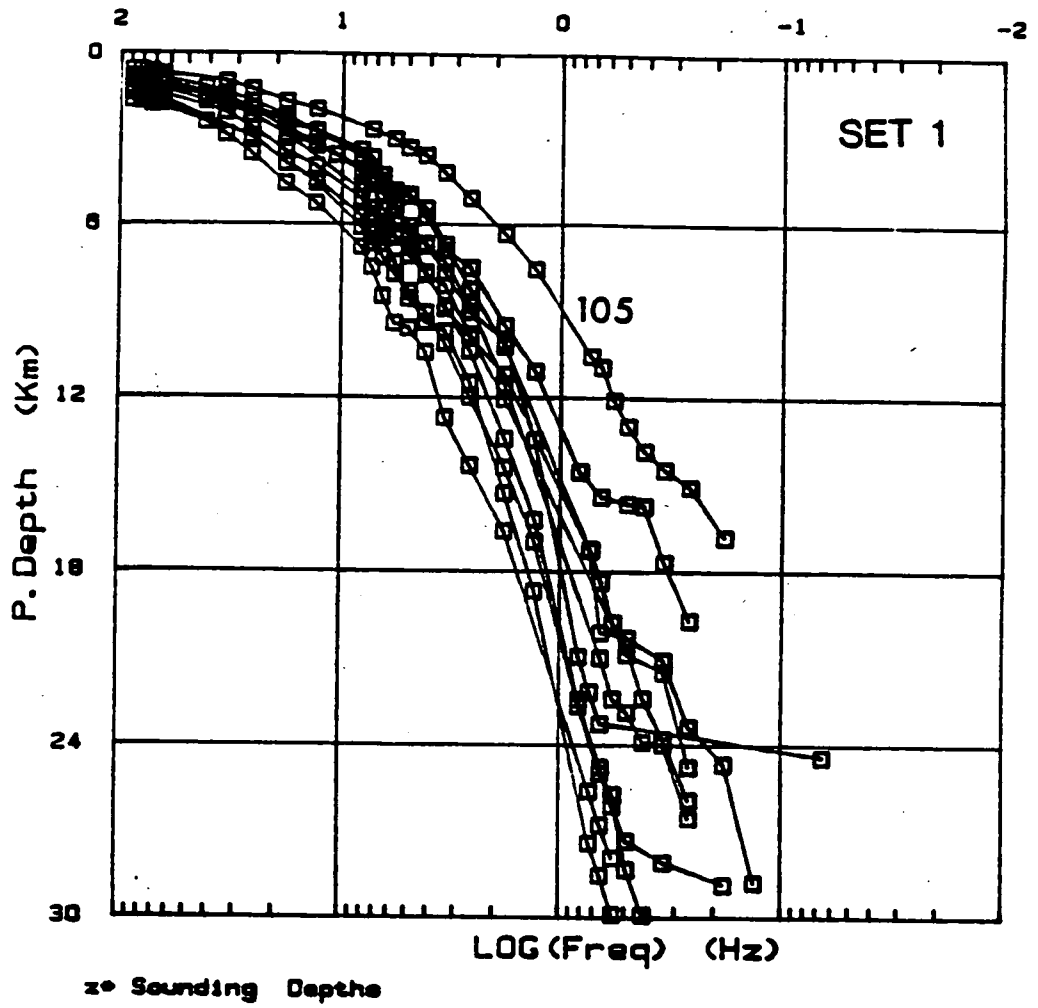

Figure 5.2. Penetration depths for the survey sites (a) SET 1 sites 101-112. (b) SET 2 sites 201-202 and (c) SET 3 sites 301-303. The x axis defines the four decade sounding bandwidth.

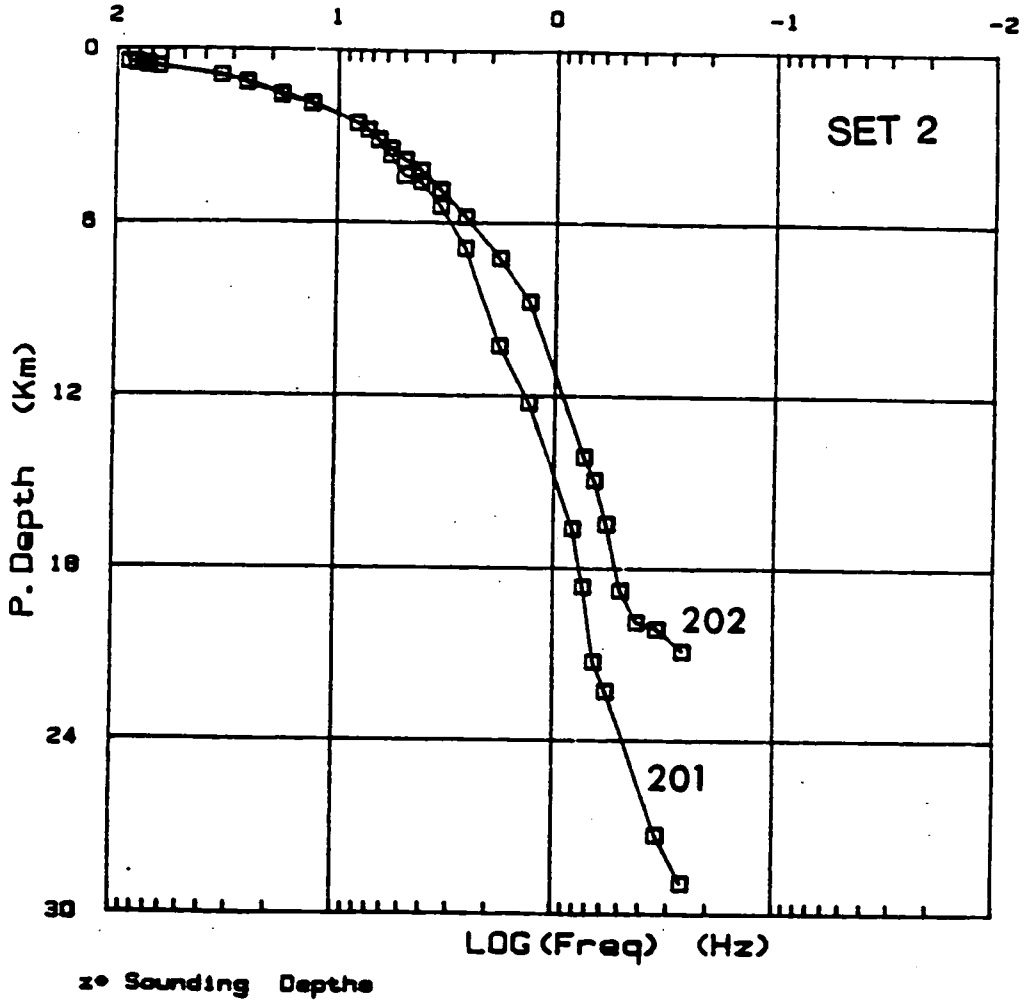

Figure 5.2. Penetration depths for the survey sites (a) SET 1 sites 101-112. (b) SET 2 sites 201-202 and (c) SET 3 sites 301-303. The x axis defines the four decade sounding bandwidth.

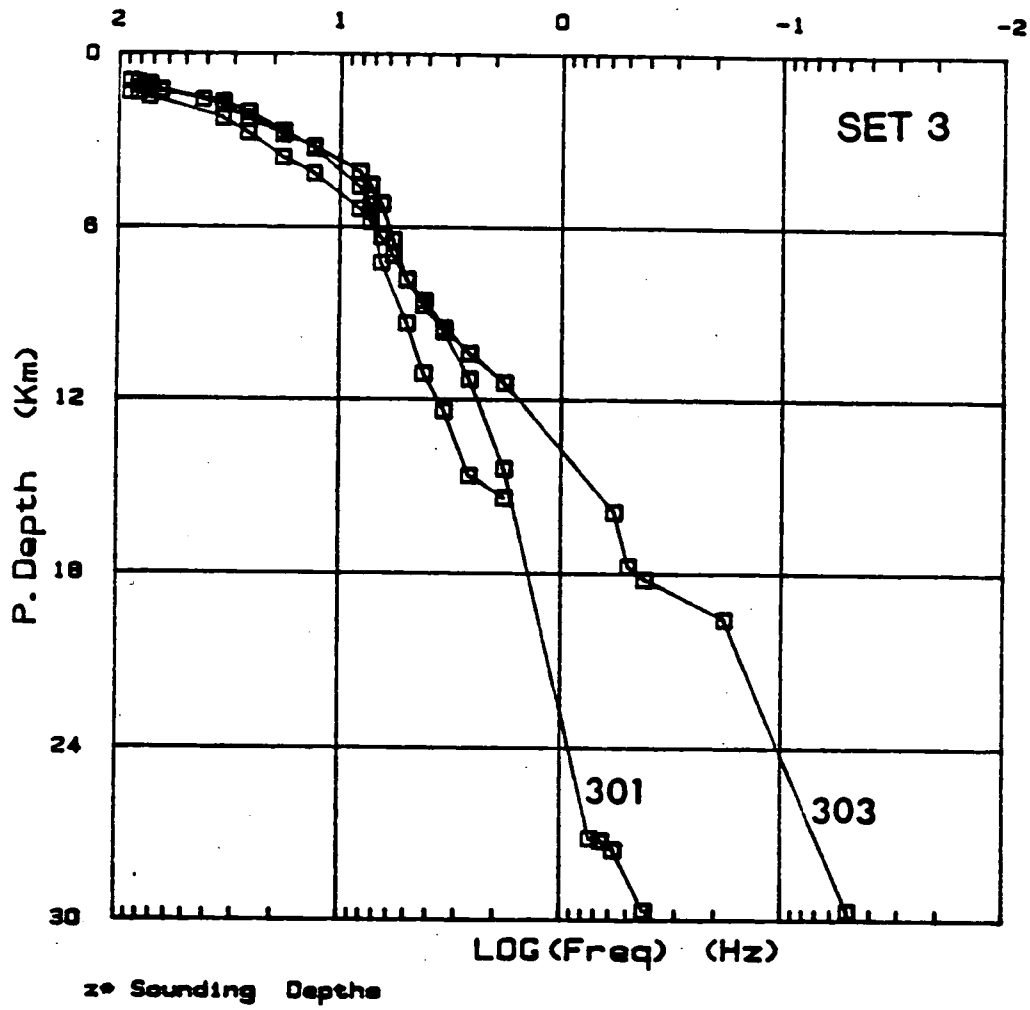

Figure 5.2. Penetration depths for the survey sites (a) SET 1 sites 101-112. (b) SET 2 sites 201-202 and (c) SET 3 sites 301-303. The x axis defines the four decade sounding bandwidth.

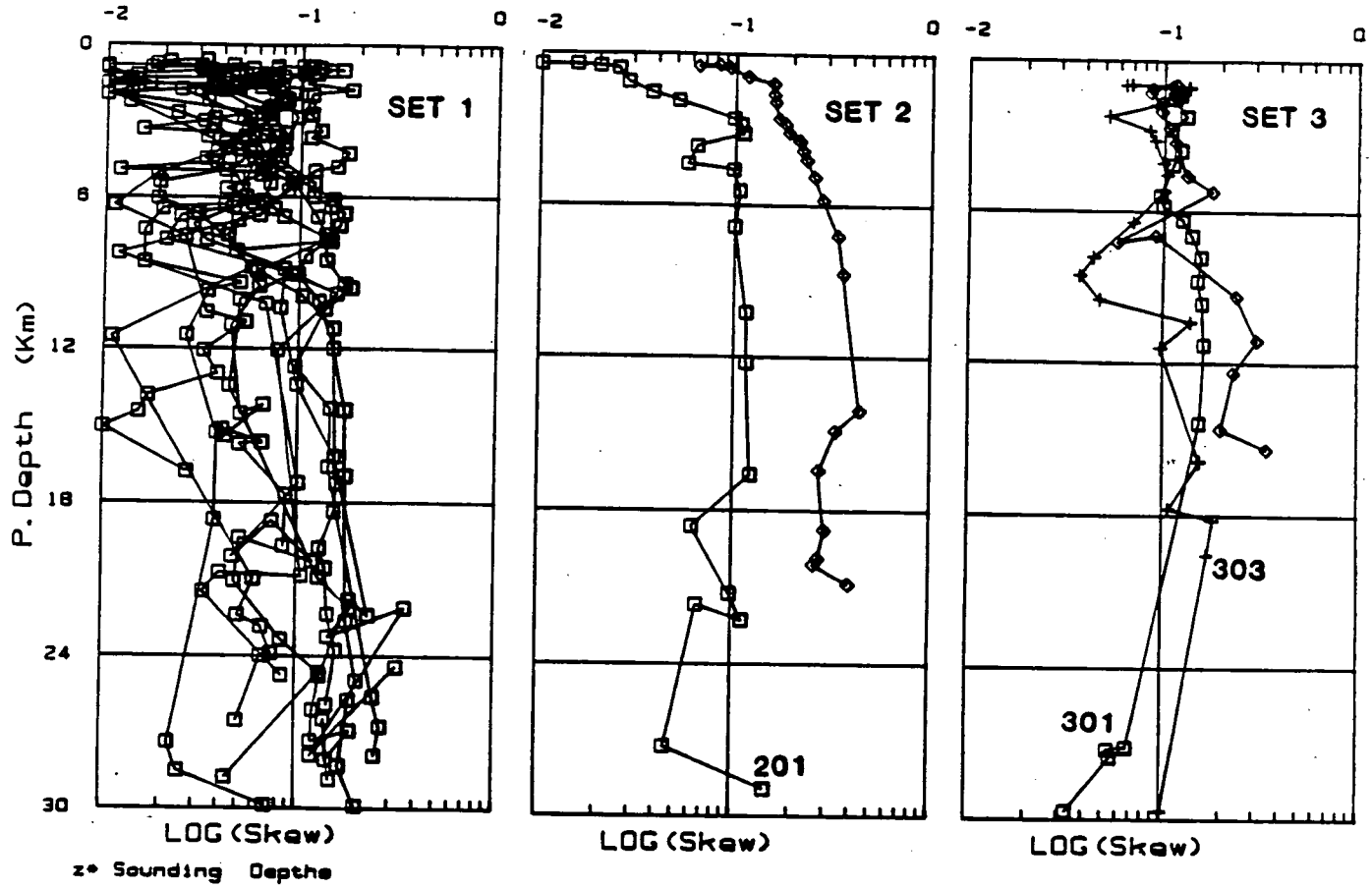

Figure 5.3. Skew values (log scale) for the survey data grouped into the 3 standard SETS.

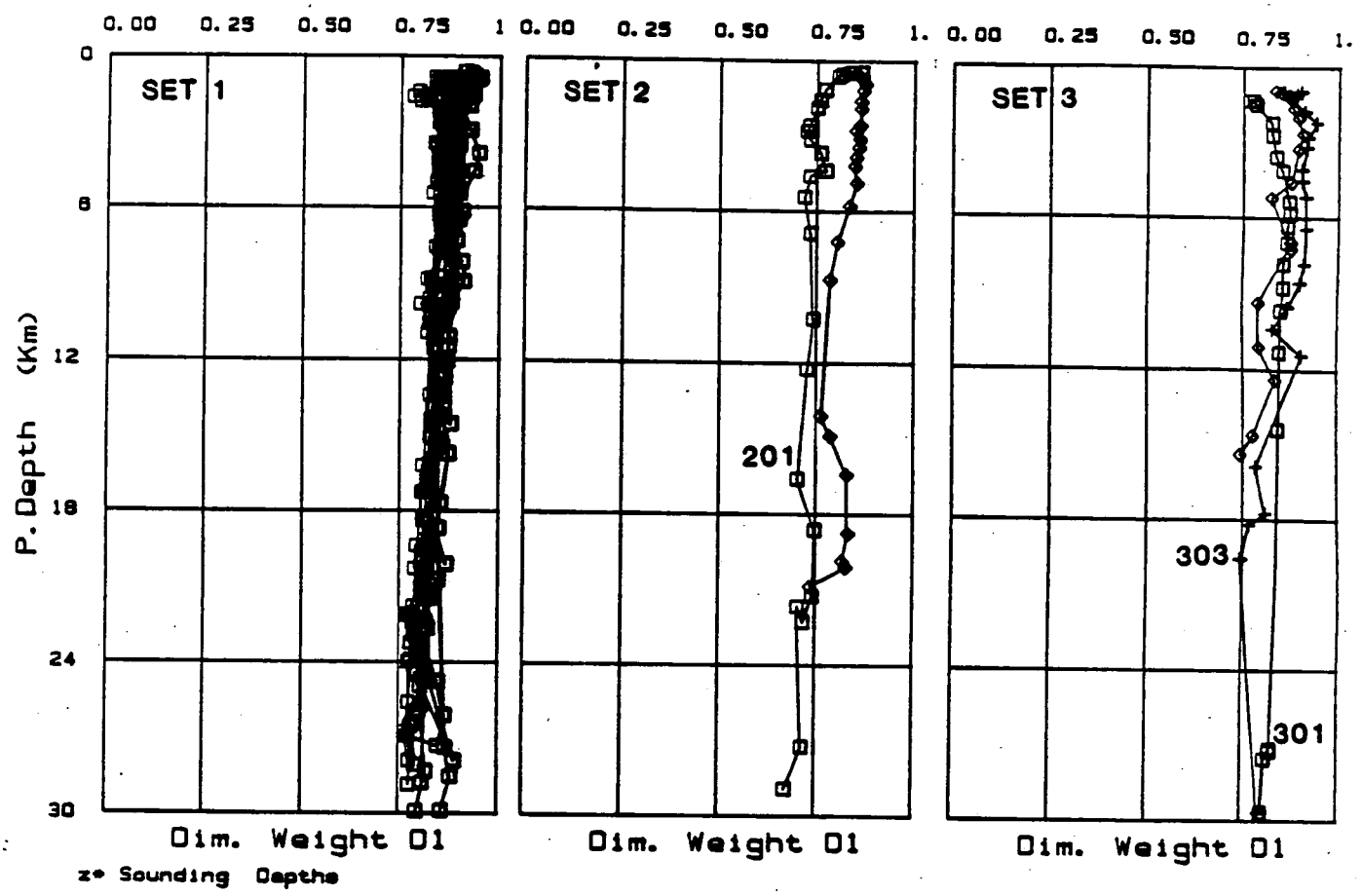

Figure 5.4. Dimensionality weights for the survey data grouped into the 3 standard SETS. (a) one-dimensional D1 weight, (b) two-dimensional D2 weight and (c) three-dimensional D3 weight.

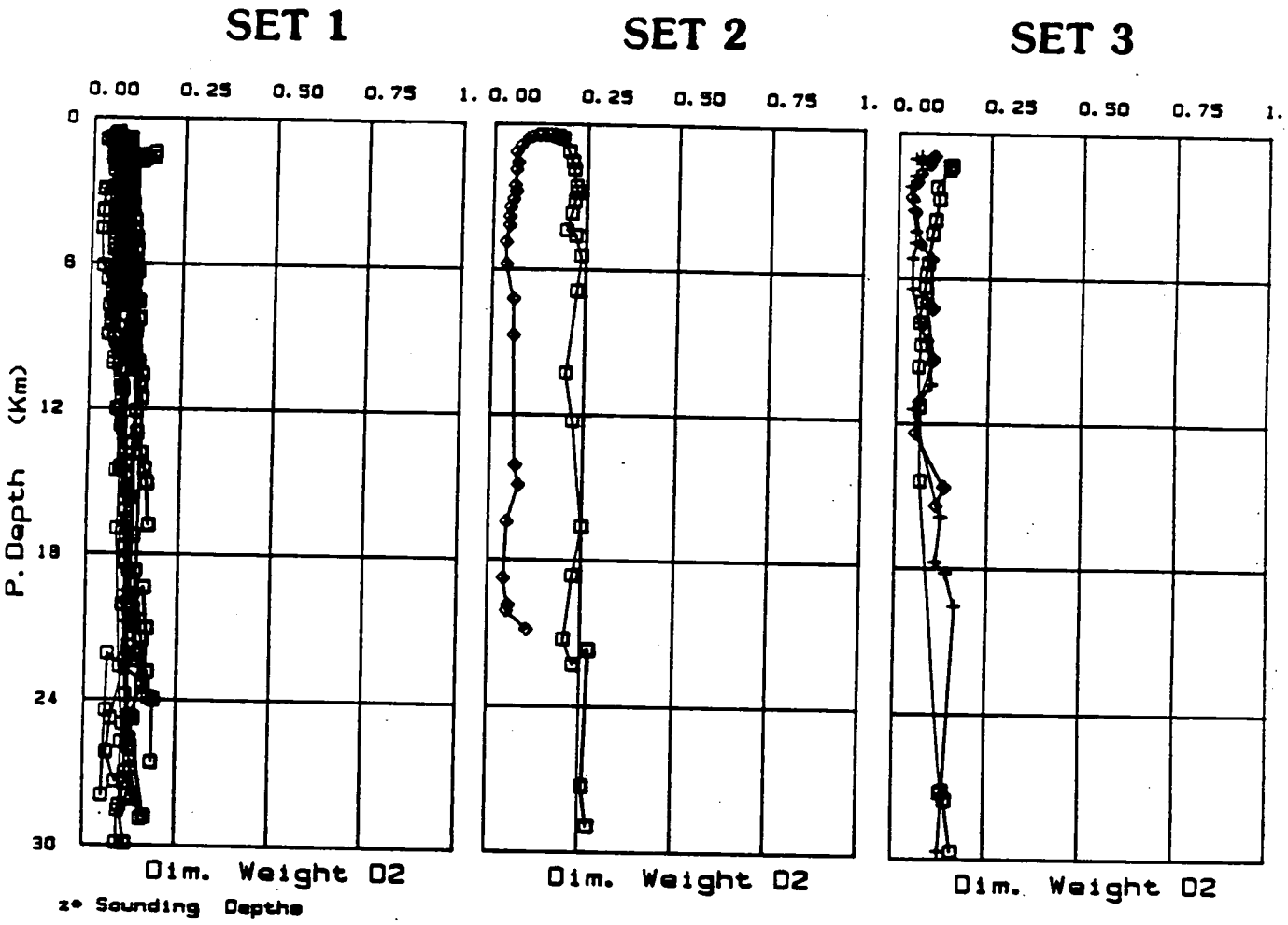

Figure 5.4. Dimensionality weights for the survey data grouped into the 3 standard SETS. (a) one-dimensional D1 weight, (b) two-dimensional D2 weight and (c) three-dimensional D3 weight.

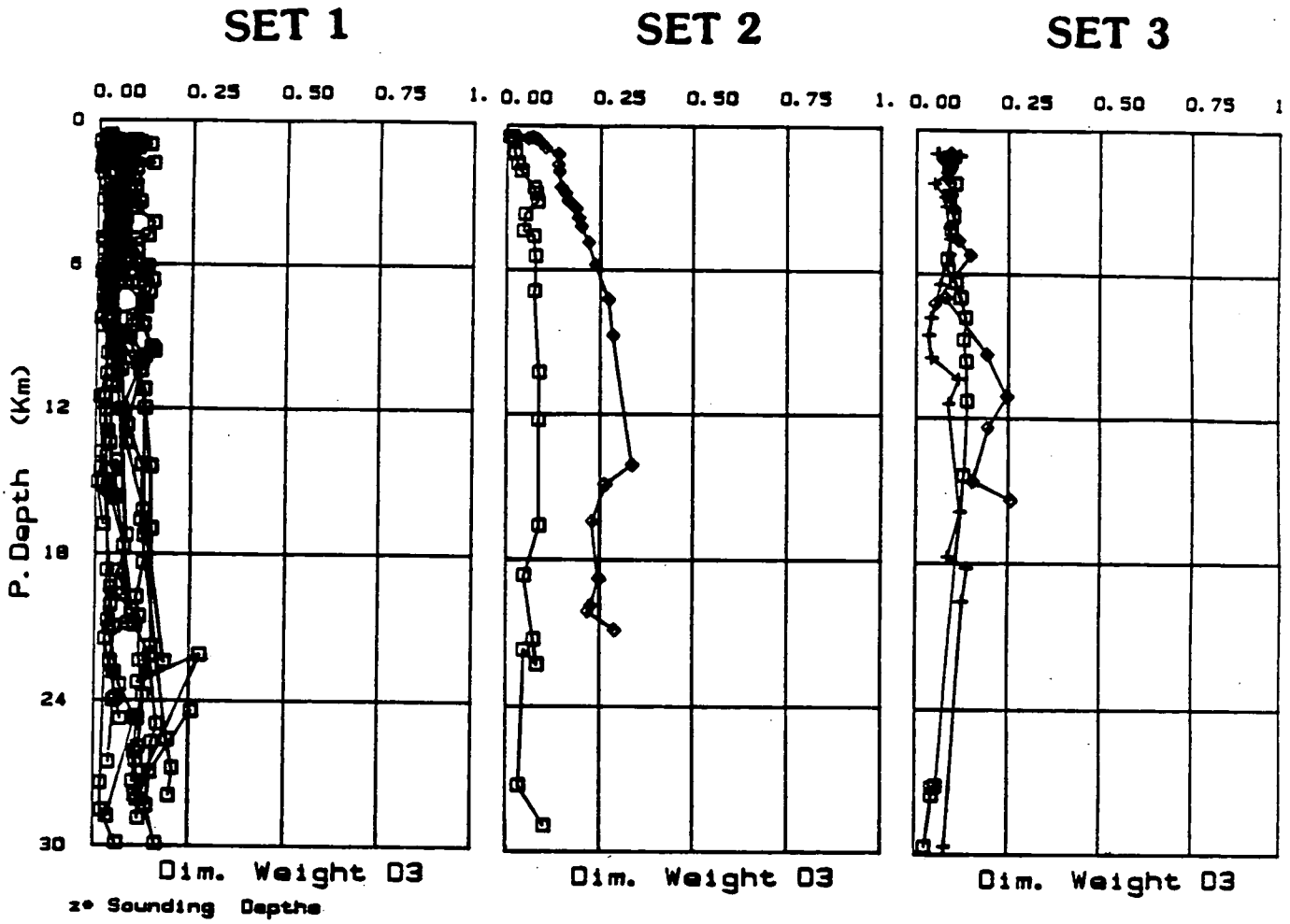

Figure 5.4. Dimensionality weights for the survey data grouped into the 3 standard SETS. (a) one-dimensional D1 weight, (b) two-dimensional D2 weight and (c) three-dimensional D3 weight.

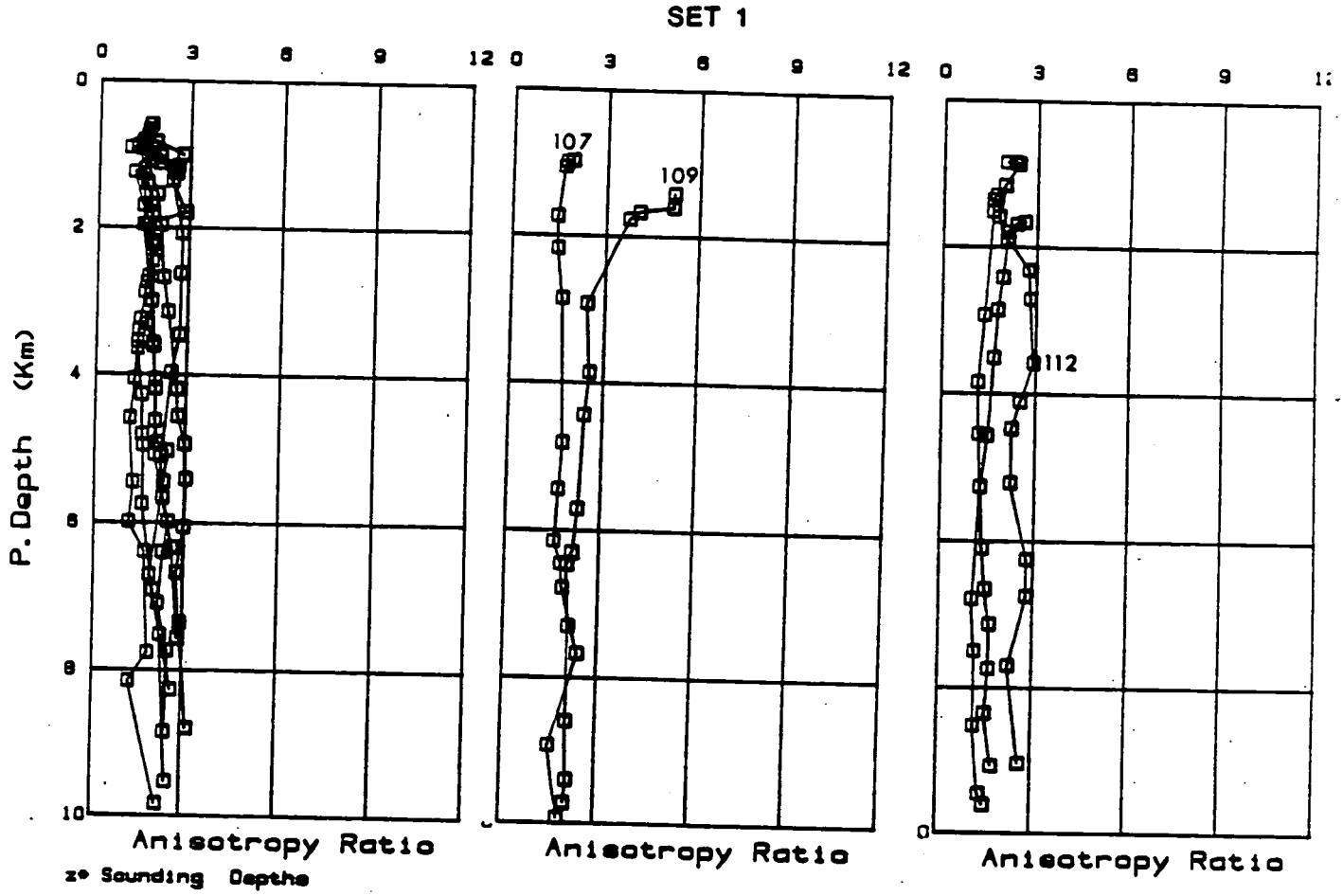

Figure 5.5. Anisotropy ratios for the survey data grouped into the 3 standard SETS. (a) SET 1 sites. (b) SET 2 and SET 3 sites.

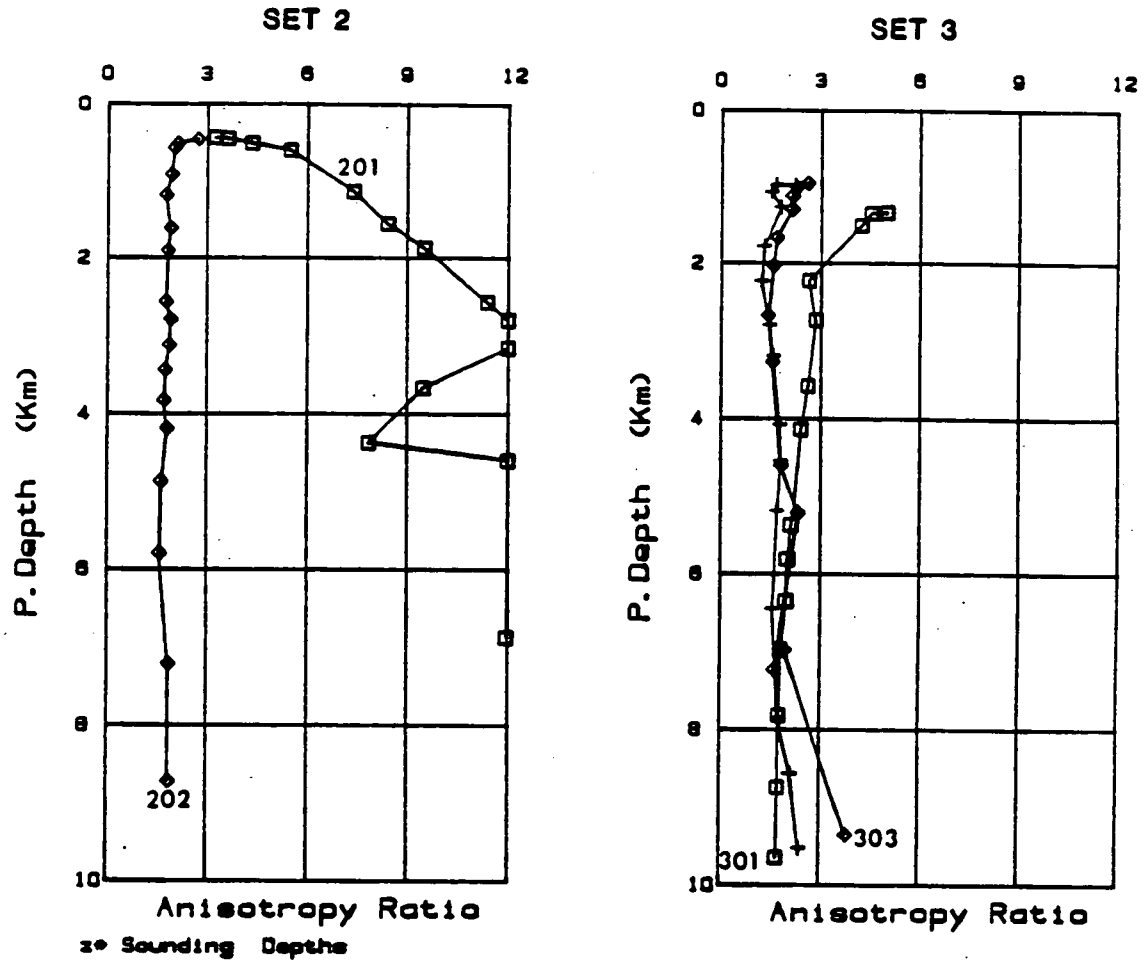

Figure 5.5. Anisotropy ratios for the survey data grouped into the 3 standard SETS. (a) SET 1 sites. (b) SET 2 and SET 3 sites.

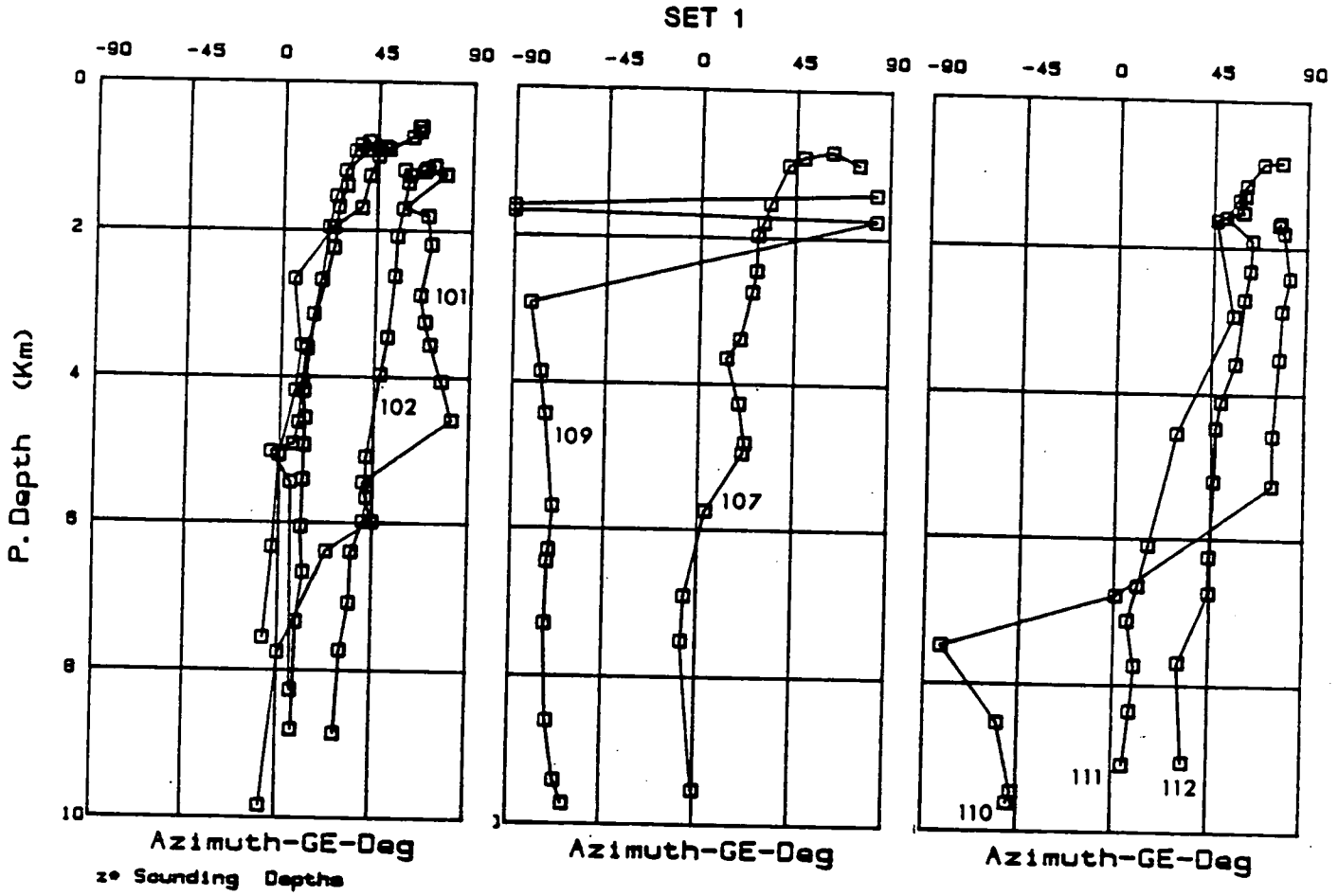

Figure 5.6. Azimuths (GE) of maximum resistivity for the survey data grouped into the standard 3 SETS. (a) SET 1 sites, (b) SET 2 and SET 3 sites.

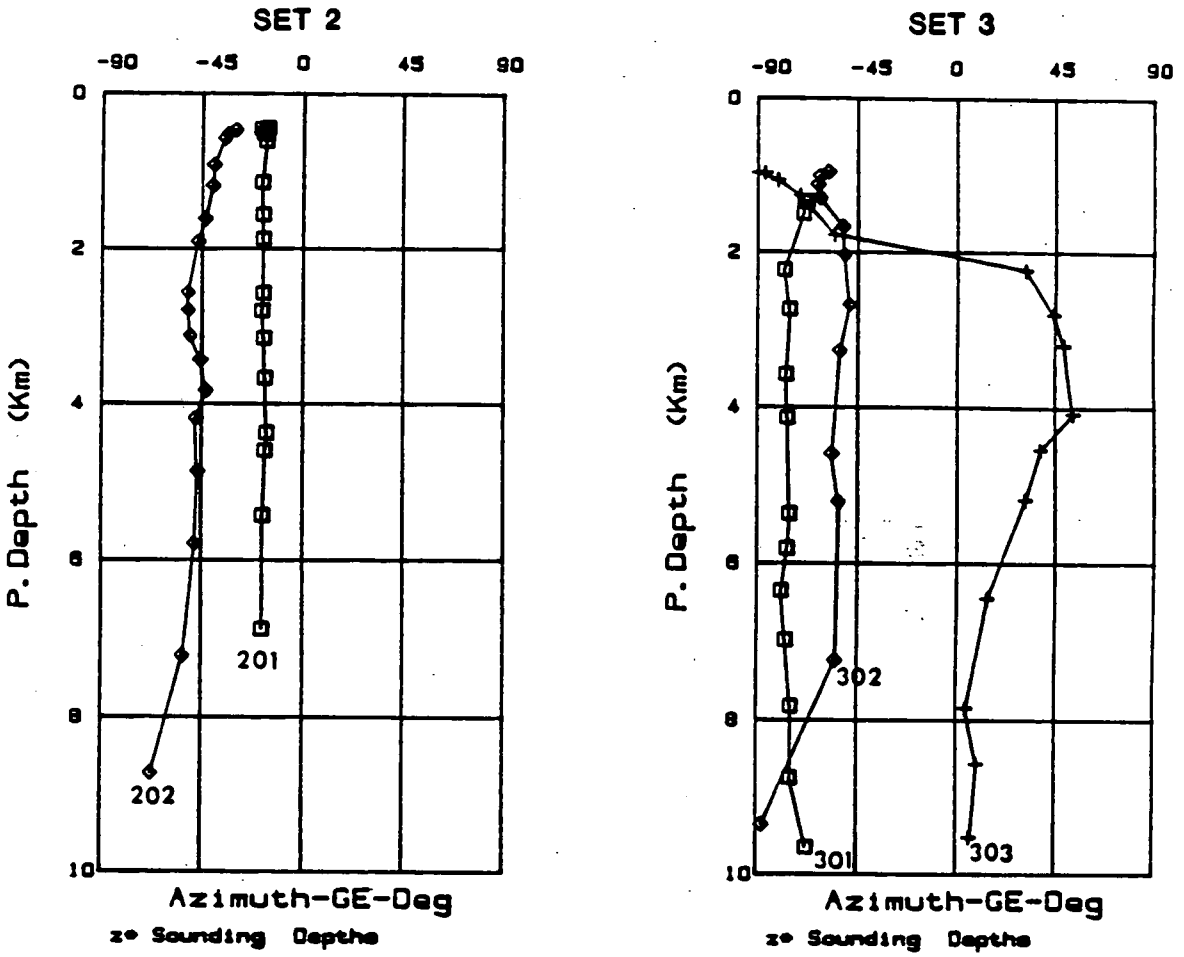

Figure 5.6. Azimuths (GE) of maximum resistivity for the survey data grouped into the standard 3 SETS. (a) SET 1 sites, (b) SET 2 and SET 3 sites.

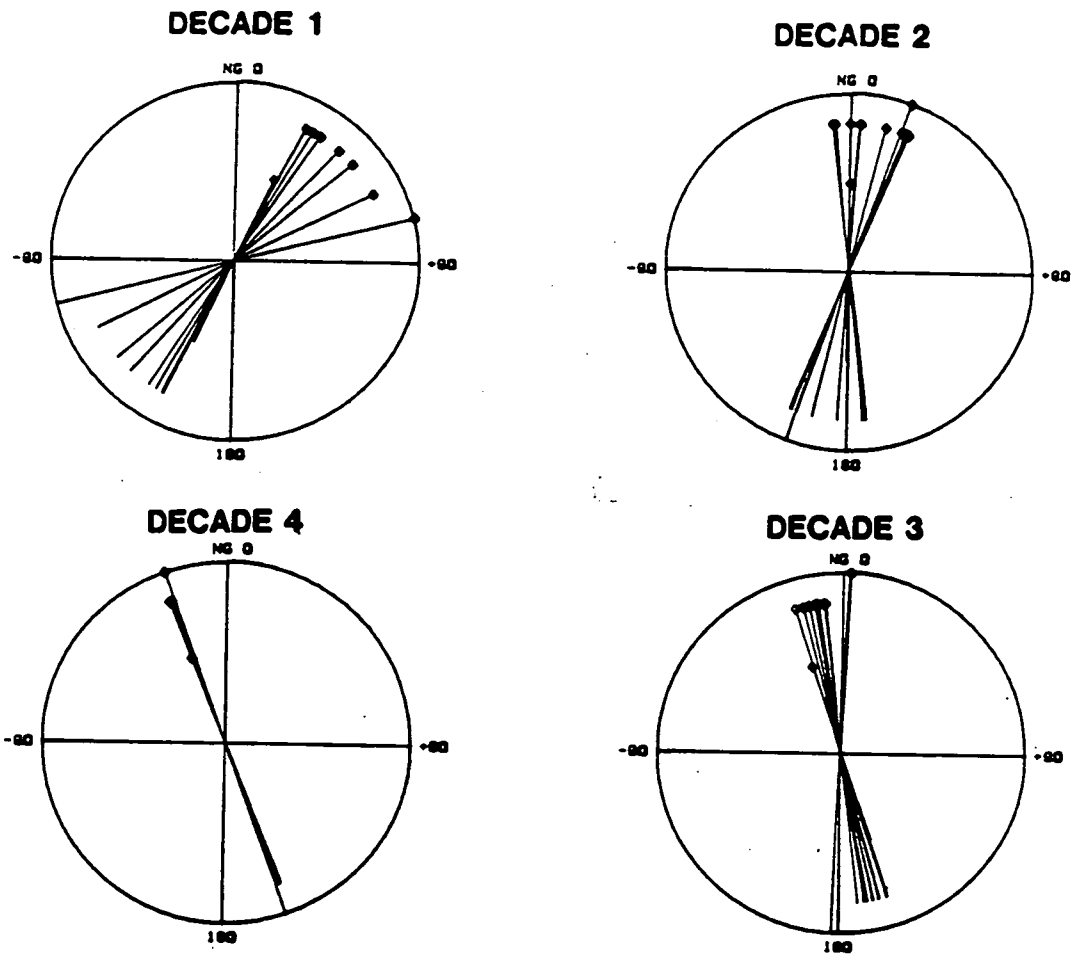

Figure 5.7. Azimuths (GE) of maximum resistivity at site 106 for the four decade sounding bandwidth. Decade 1 (100-10 Hz), Decade 2 (10-1 Hz), Decade 3 (1-0.1 Hz) and Decade 4 (0.1-0.01 Hz).

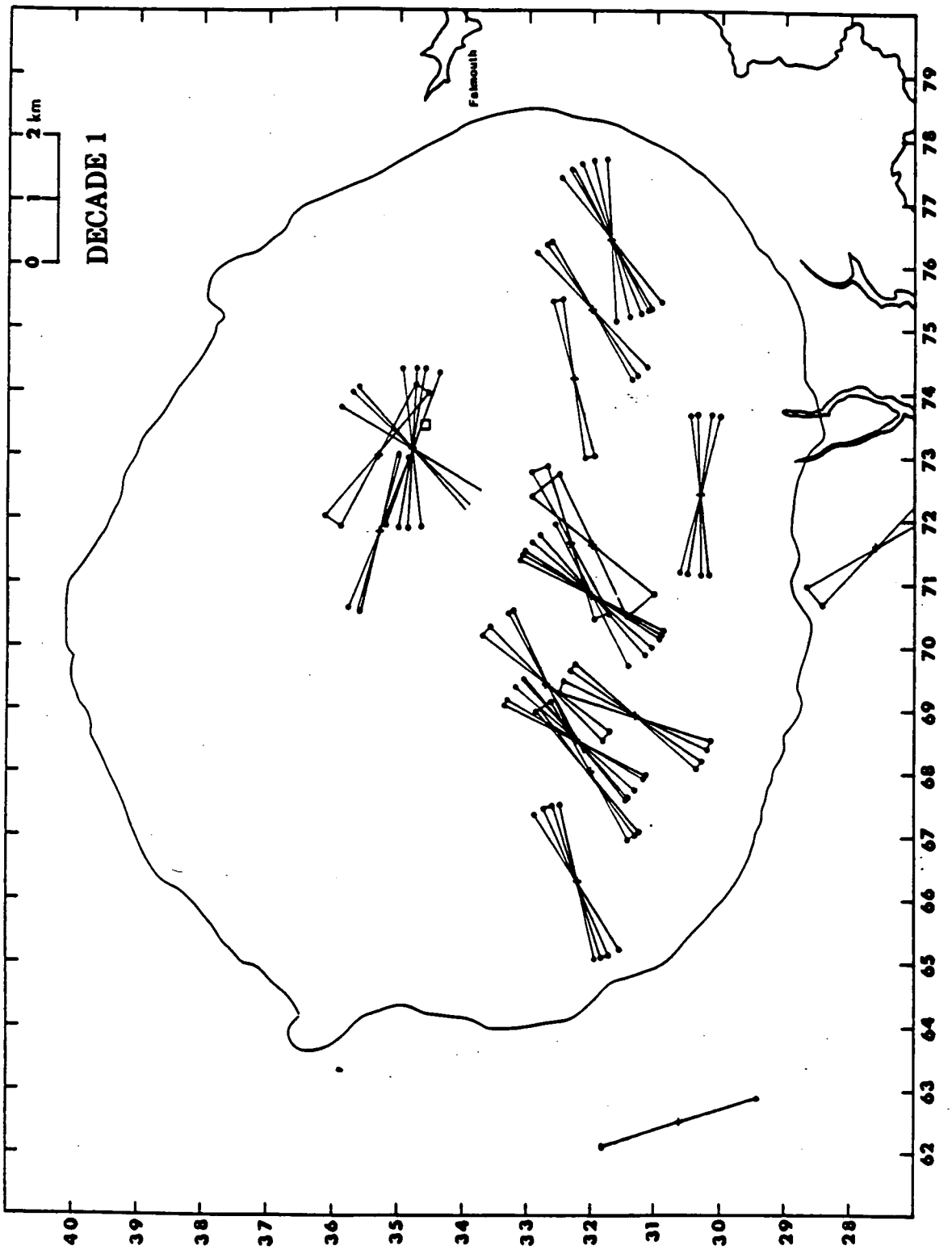

Figure 5.8. Maps of azimuths (GE) of maximum resistivity for the survey data for four decades decreasing in frequency. (a) Decade 1, (b) Decade 2, (c) Decade 3 and (d) Decade 4.

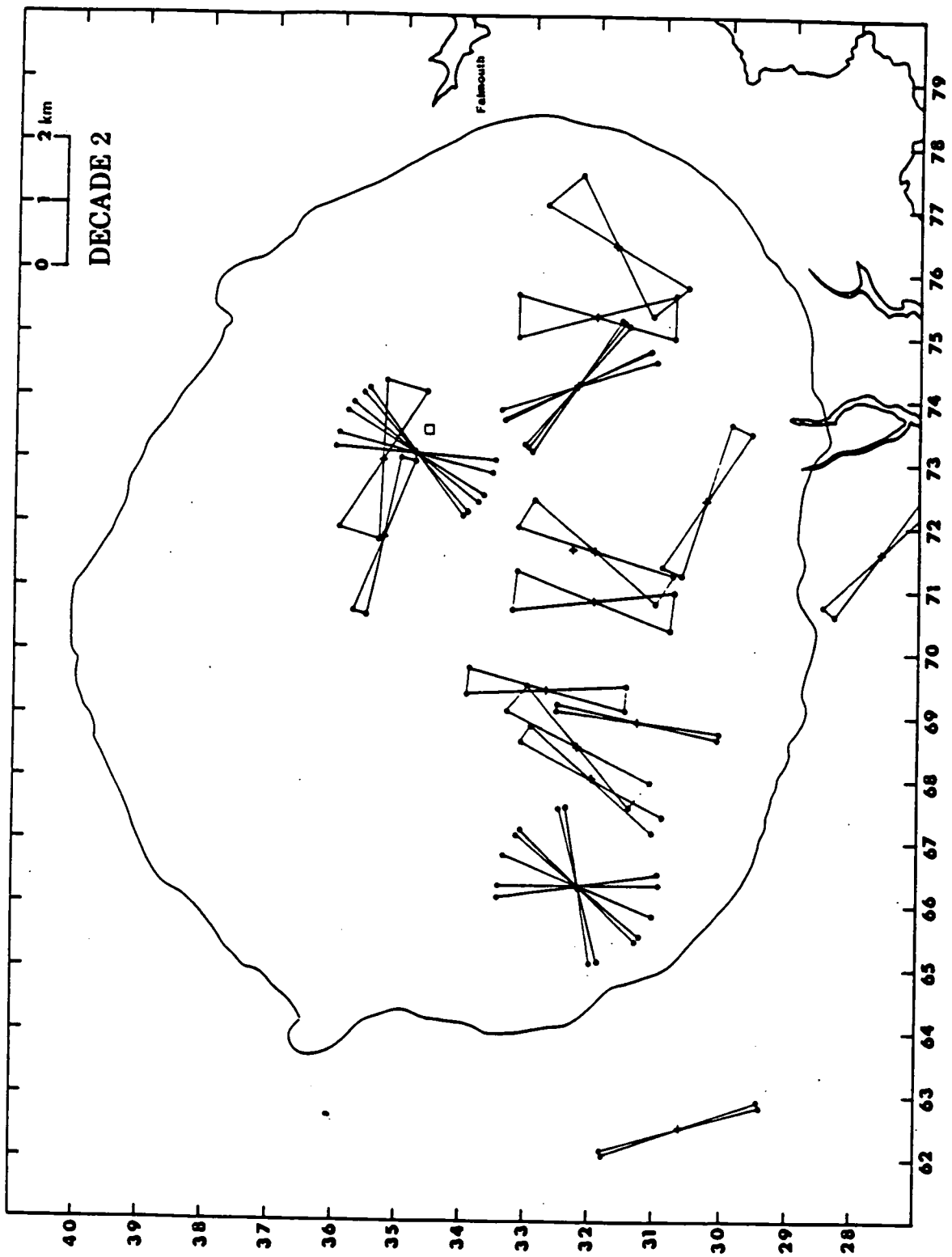

Figure 5.8. Maps of azimuths (GE) of maximum resistivity for the survey data for four decades decreasing in frequency. (a) Decade 1, (b) Decade 2, (c) Decade 3 and (d) Decade 4.

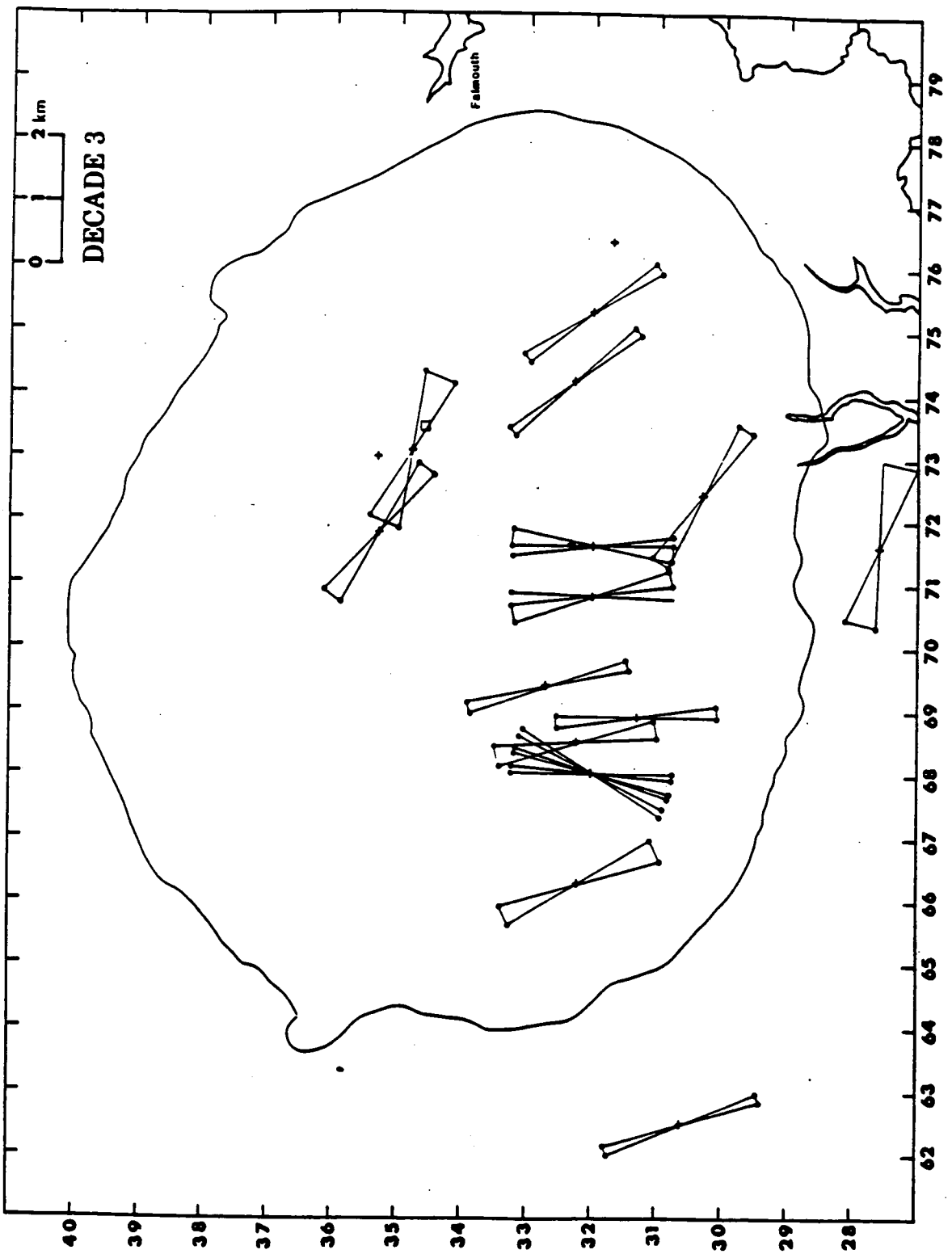

Figure 5.8. Maps of azimuths (GE) of maximum resistivity for the survey data for four decades decreasing in frequency. (a) Decade 1, (b) Decade 2, (c) Decade 3 and (d) Decade 4.

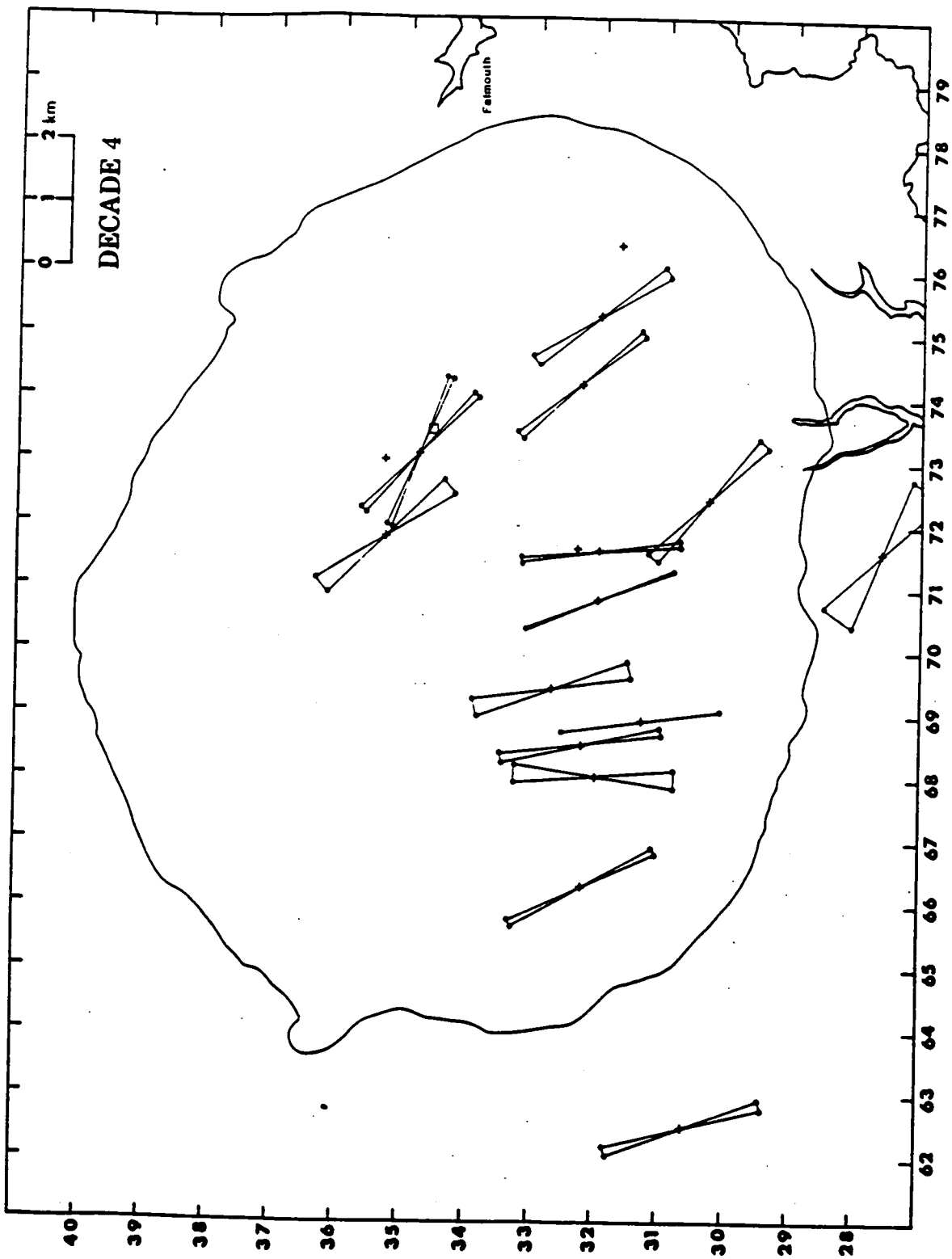

Figure 5.8. Maps of azimuths (GE) of maximum resistivity for the survey data for four decades decreasing in frequency. (a) Decade 1, (b) Decade 2, (c) Decade 3 and (d) Decade 4.

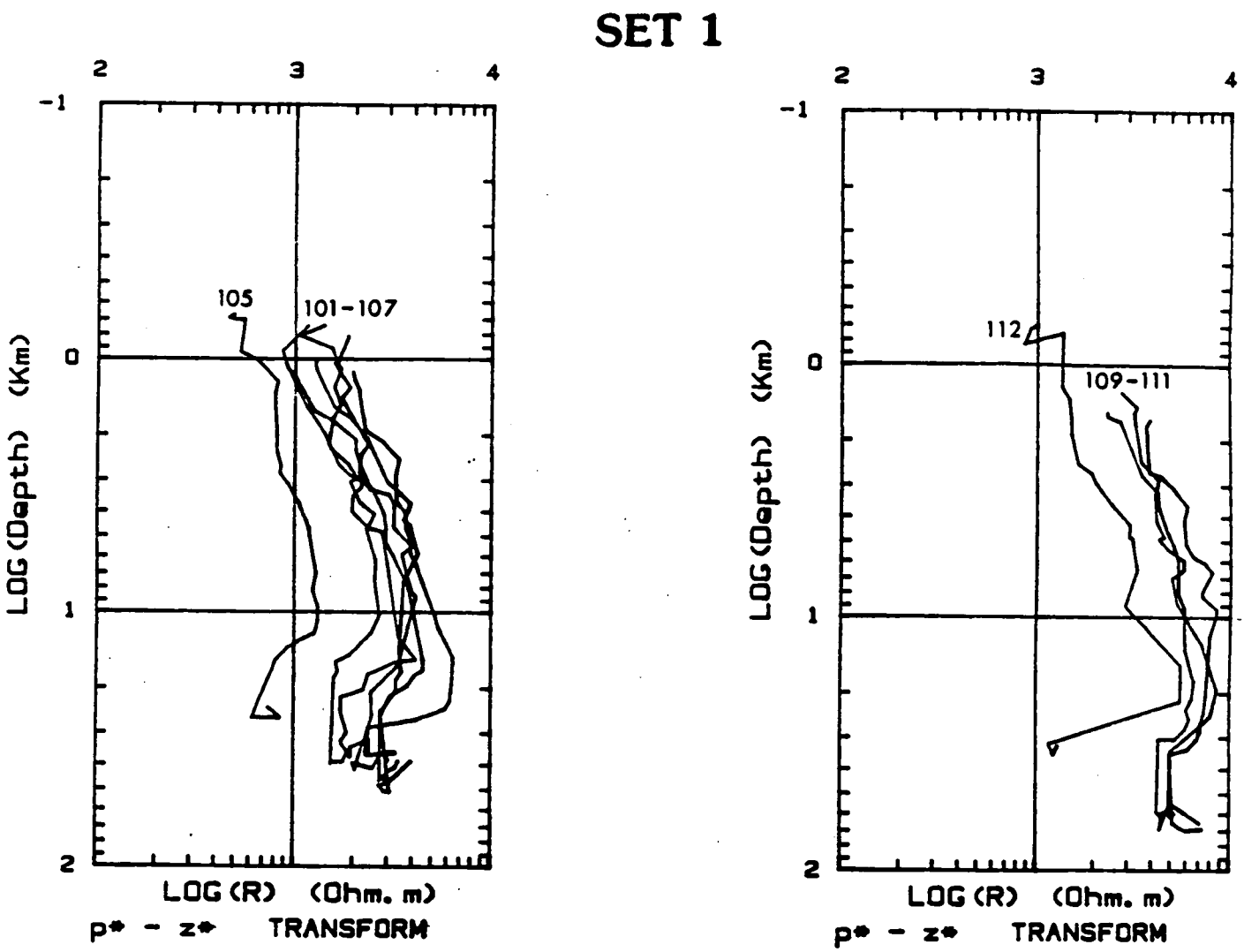

Figure 5.9. Schmucker resistivity/depth transform in usual log-log coordinates for survey data grouped into the standard 3 SETS. (a) SET 1 sites, (b) SET 2 and SET 3 sites. R refers to resistivity.

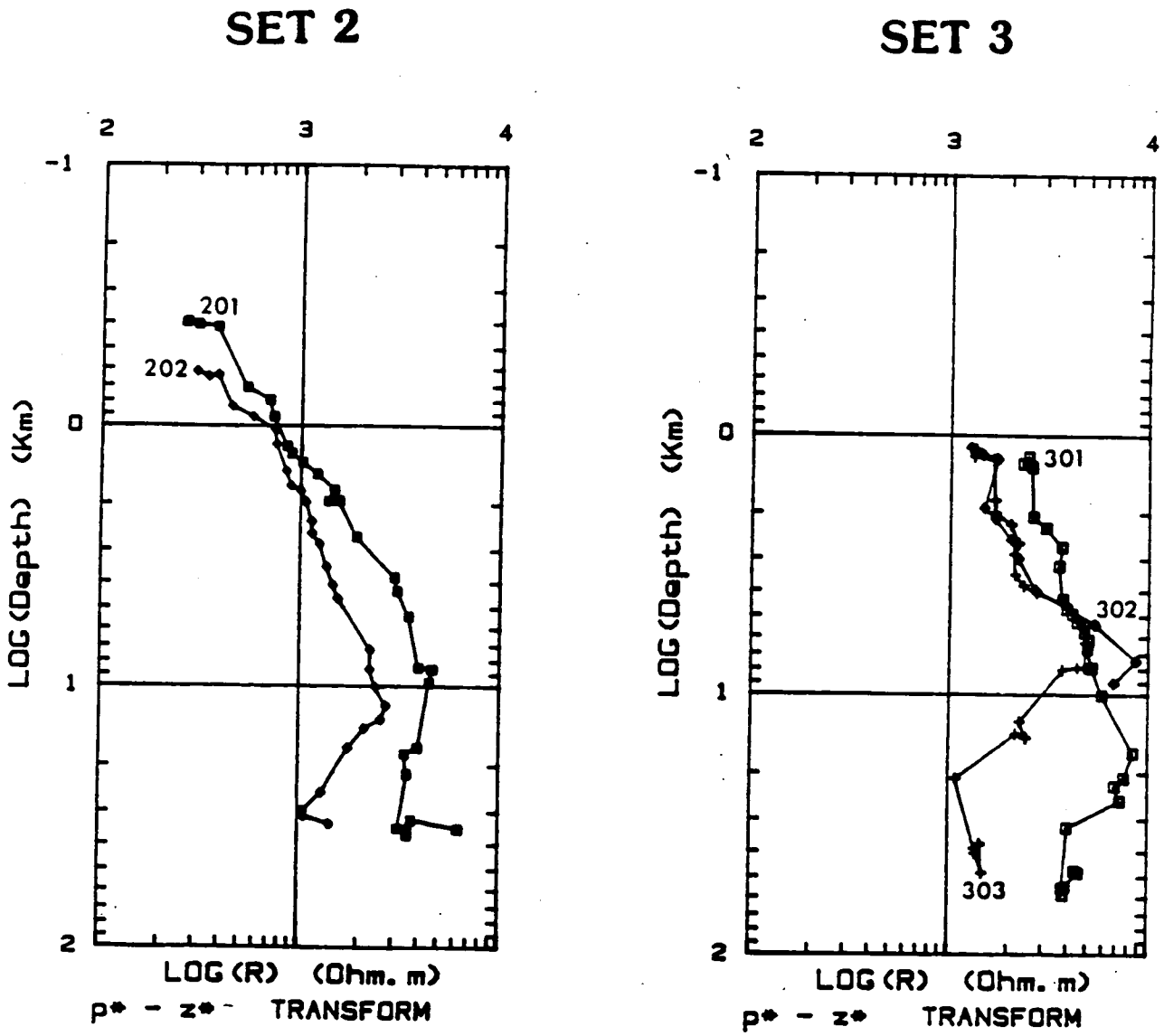

Figure 5.9. Schmucker resistivity/depth transform in usual log-log coordinates for survey data grouped into the standard 3 SETS. (a) SET 1 sites. (b) SET 2 and SET 3 sites. R refers to resistivity.

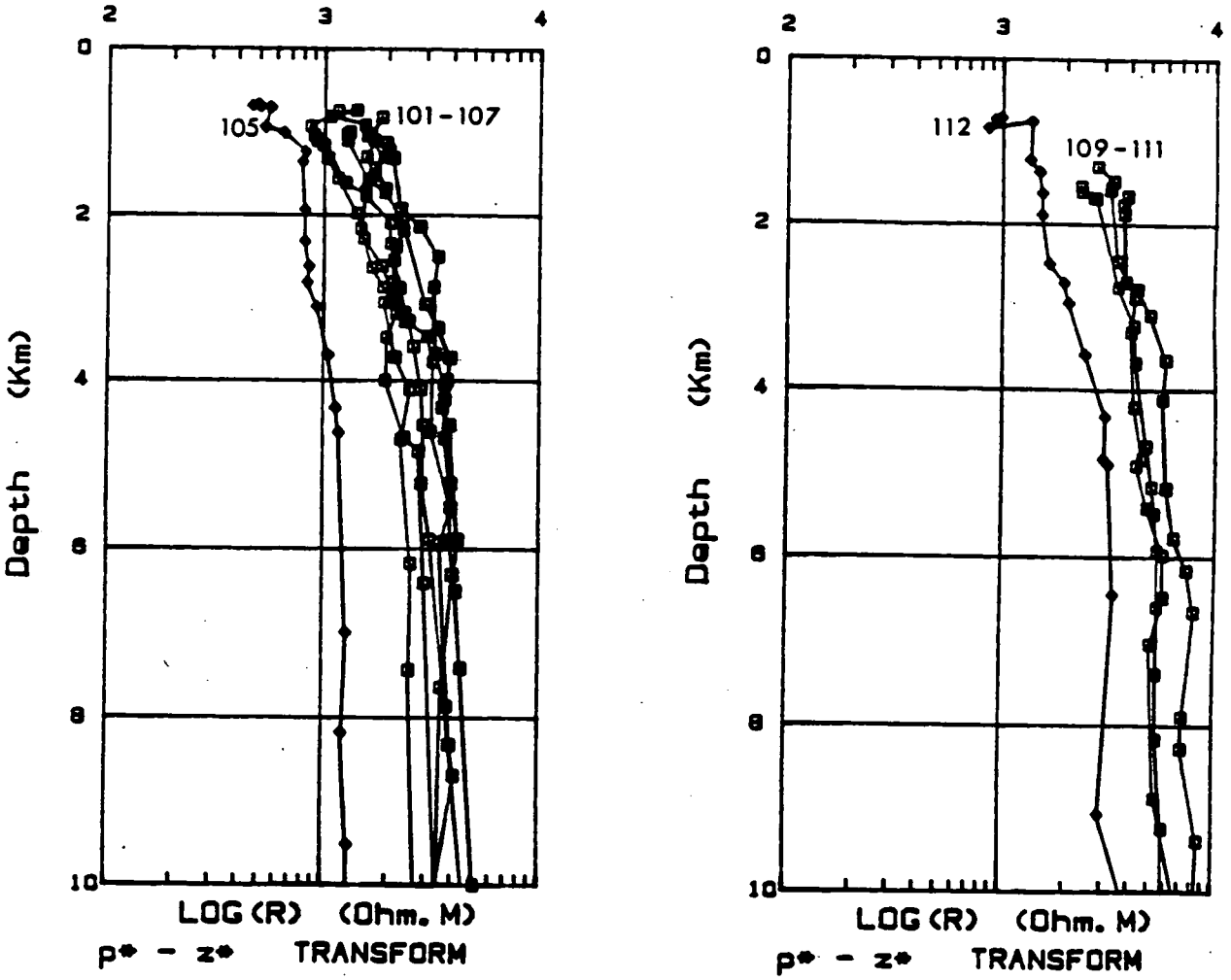

Figure 5.10. Same resistivity/depth transform results as in Figure 5.9 but using linear-depth scale for the upper crustal section. Results grouped into the 3 standard SETS. **(a)** SET 1 sites, **(b)** SET 2 and SET 3 sites.

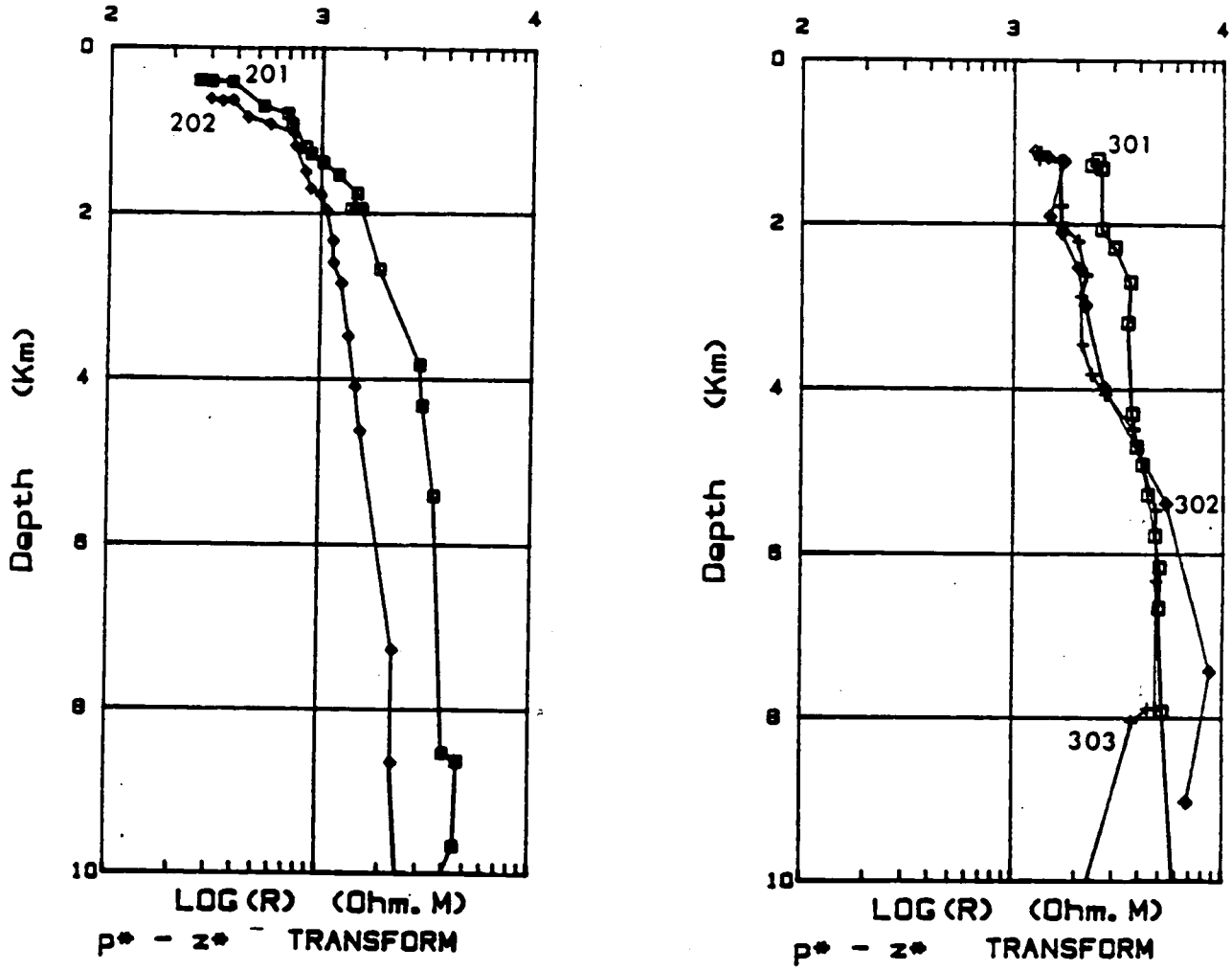

Figure 5.10. Same resistivity/depth transform results as in Figure 5.9 but using linear-depth scale for the upper crustal section. Results grouped into the 3 standard SETS. (a) SET 1 sites, (b) SET 2 and SET 3 sites.

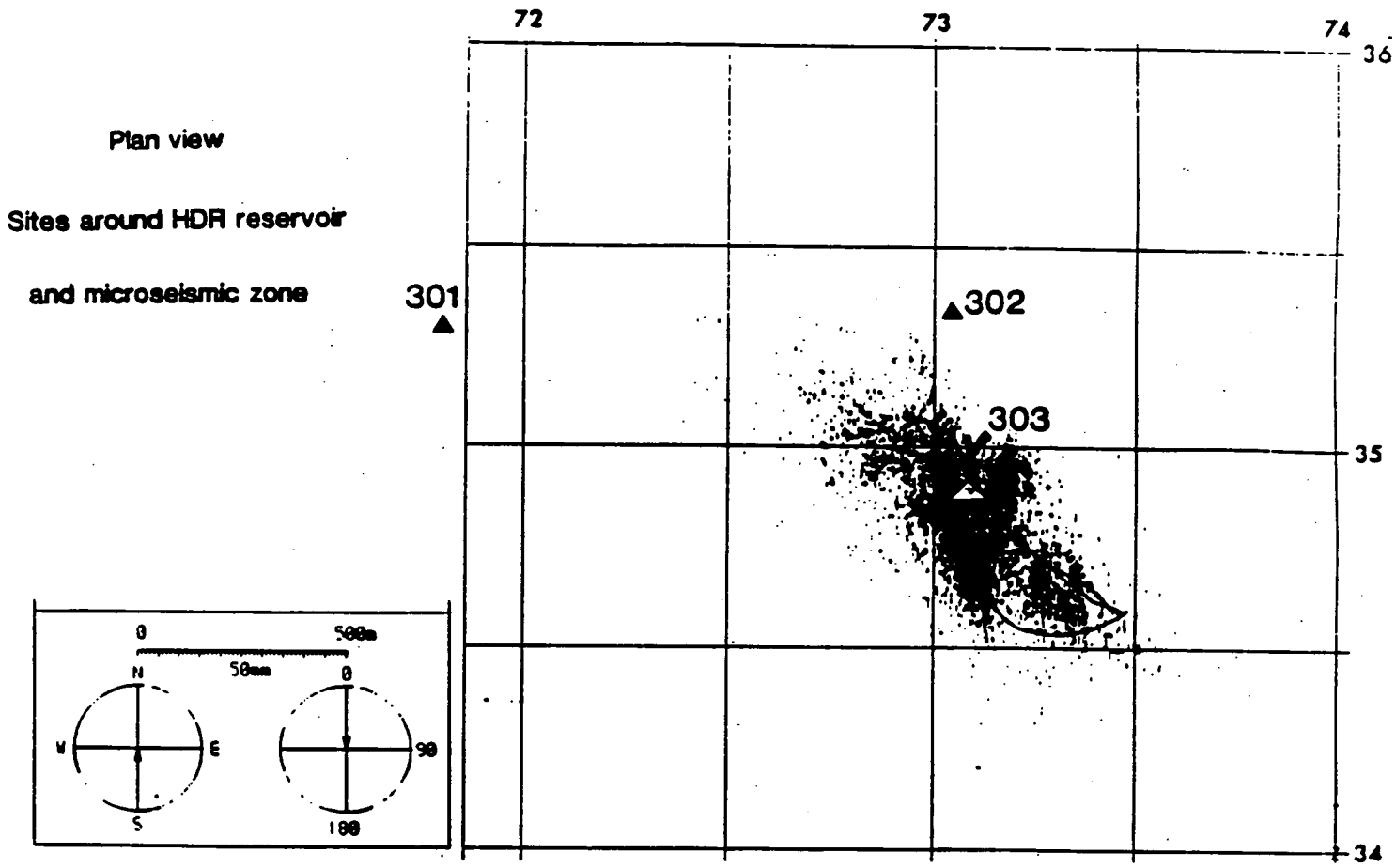

Figure 5.11. Detailed plan view of site locations 301 to 303 in relation to the microseismic zone associated with hydrofracturing of the HDR reservoir.

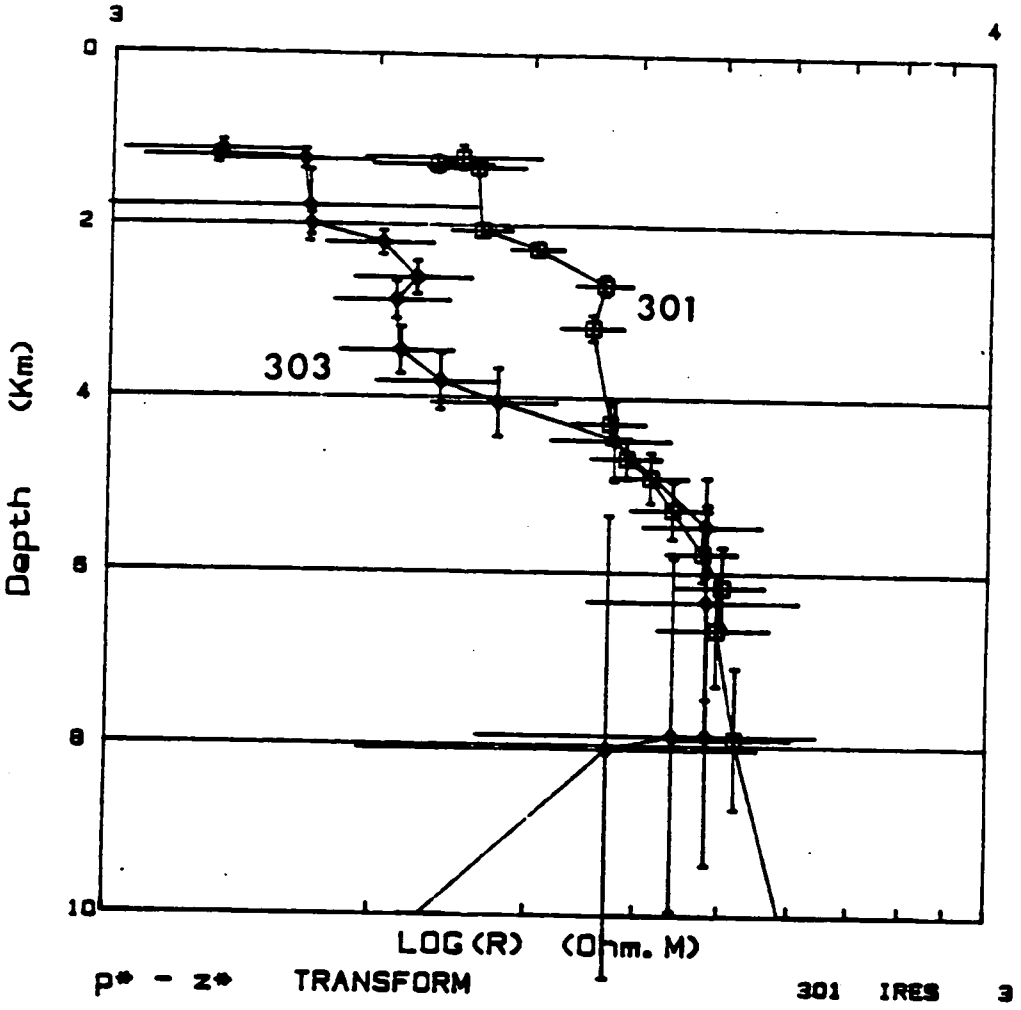

Figure 5.12. Schmucker resistivity/depth transform results at SET 3 HDR sites 301 and 303 showing likely 95% confidence limits. The results at site 302 (not shown) is identical to that at site 303 for the upper 5 km.

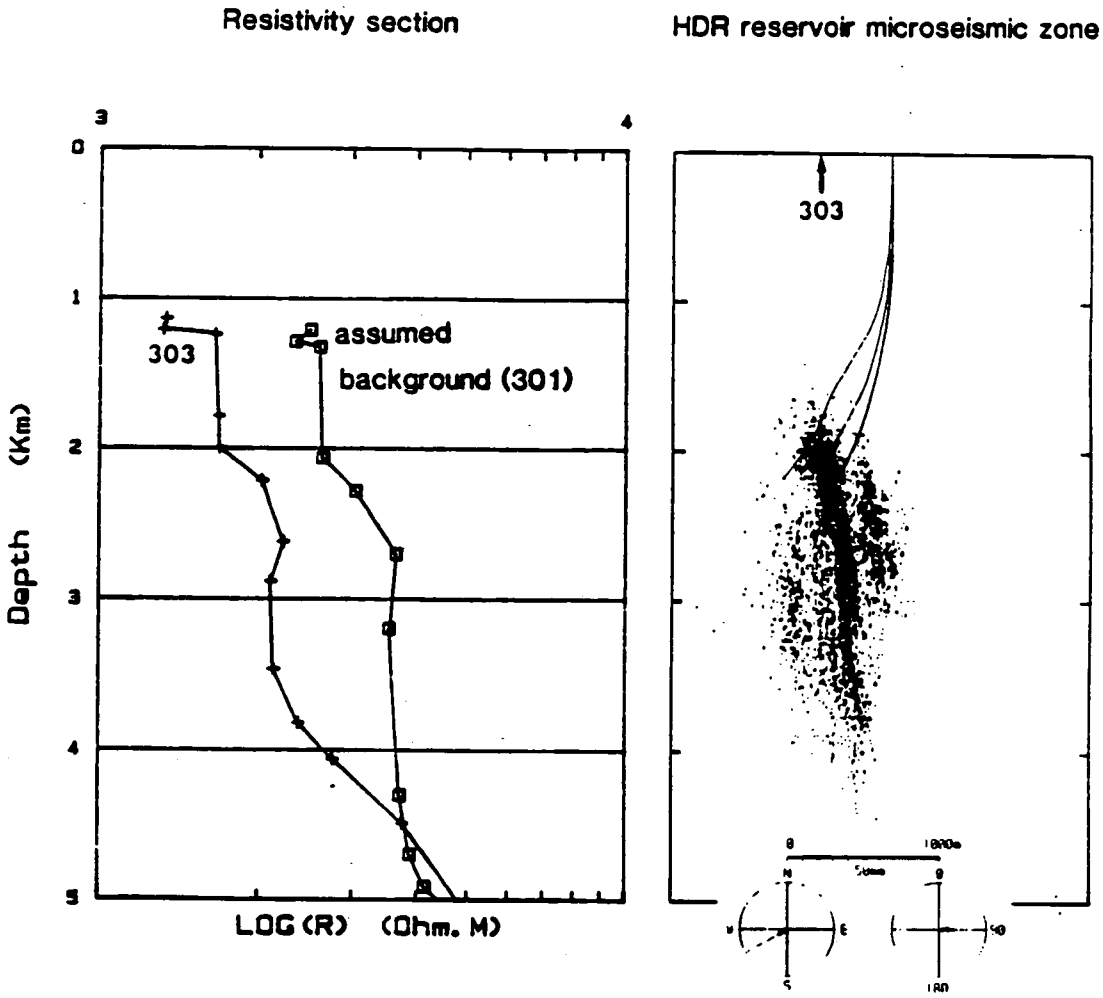

Figure 5.13. Resistivity section for the upper 5 km at sites 301 and 303/303 in relation to the microseismic zone associated with reservoir hydrofracturing. The location of site 303 is indicated.

101-107

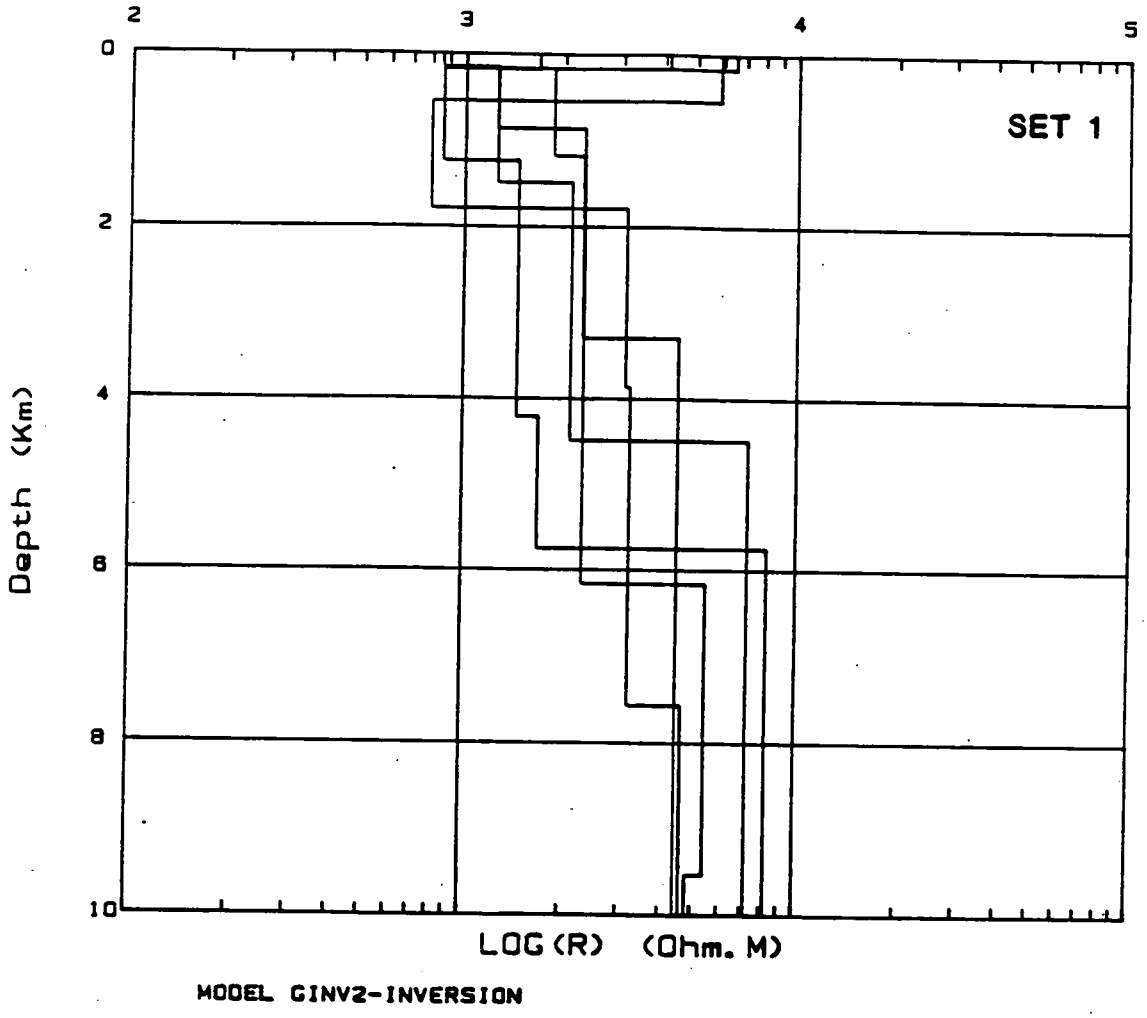

Figure 5.14. Minimum-norm, layered inversion results for survey data grouped into the 3 standard SETS. (a) SET 1, sites 101-107, (b) SET 1, sites 109-112 and (c) SET 2, sites 201-202.

109-112

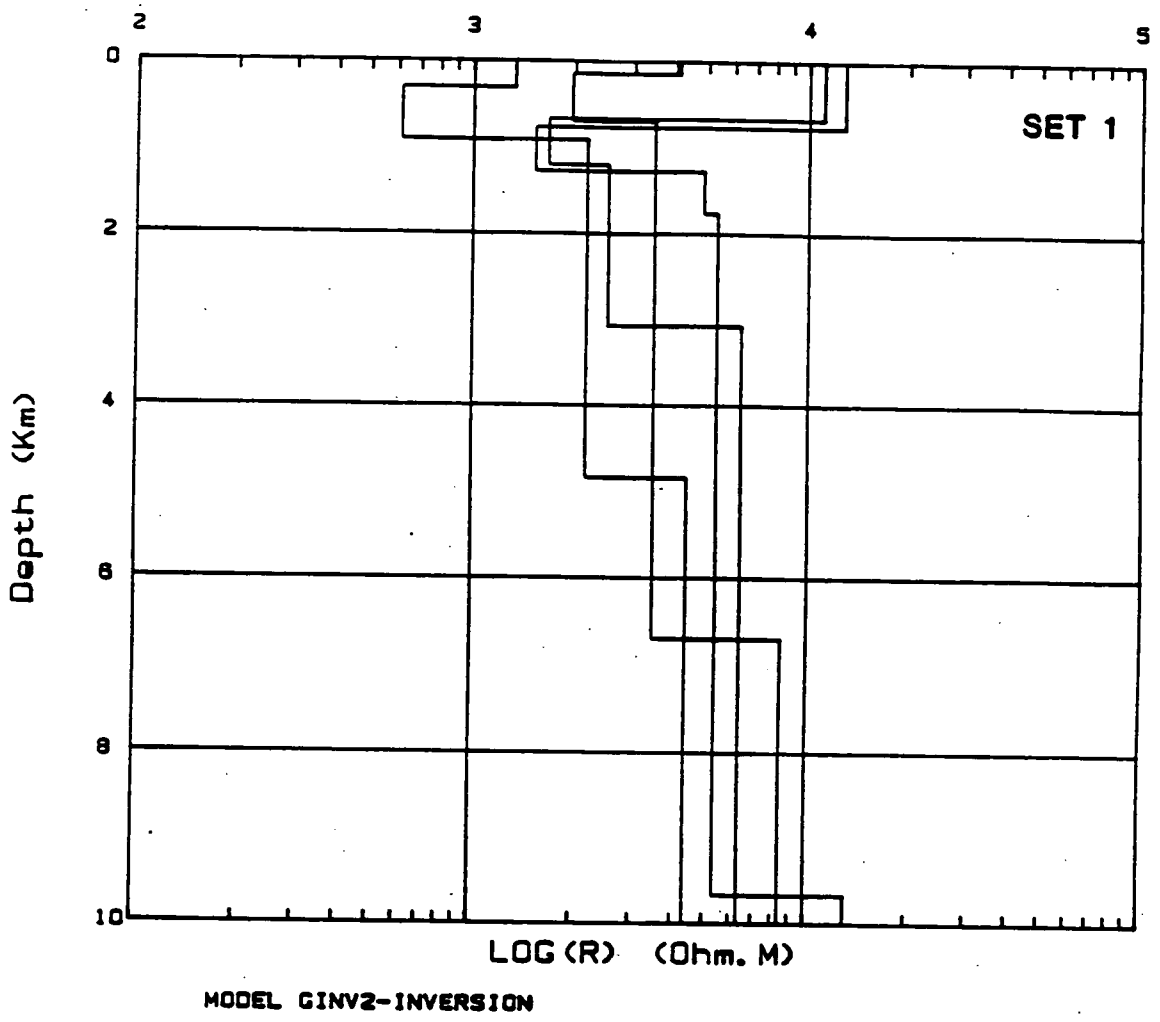

Figure 5.14. Minimum-norm, layered inversion results for survey data grouped into the 3 standard SETS. (a) SET 1, sites 101-107, (b) SET 1, sites 109-112 and (c) SET 2, sites 201-202.

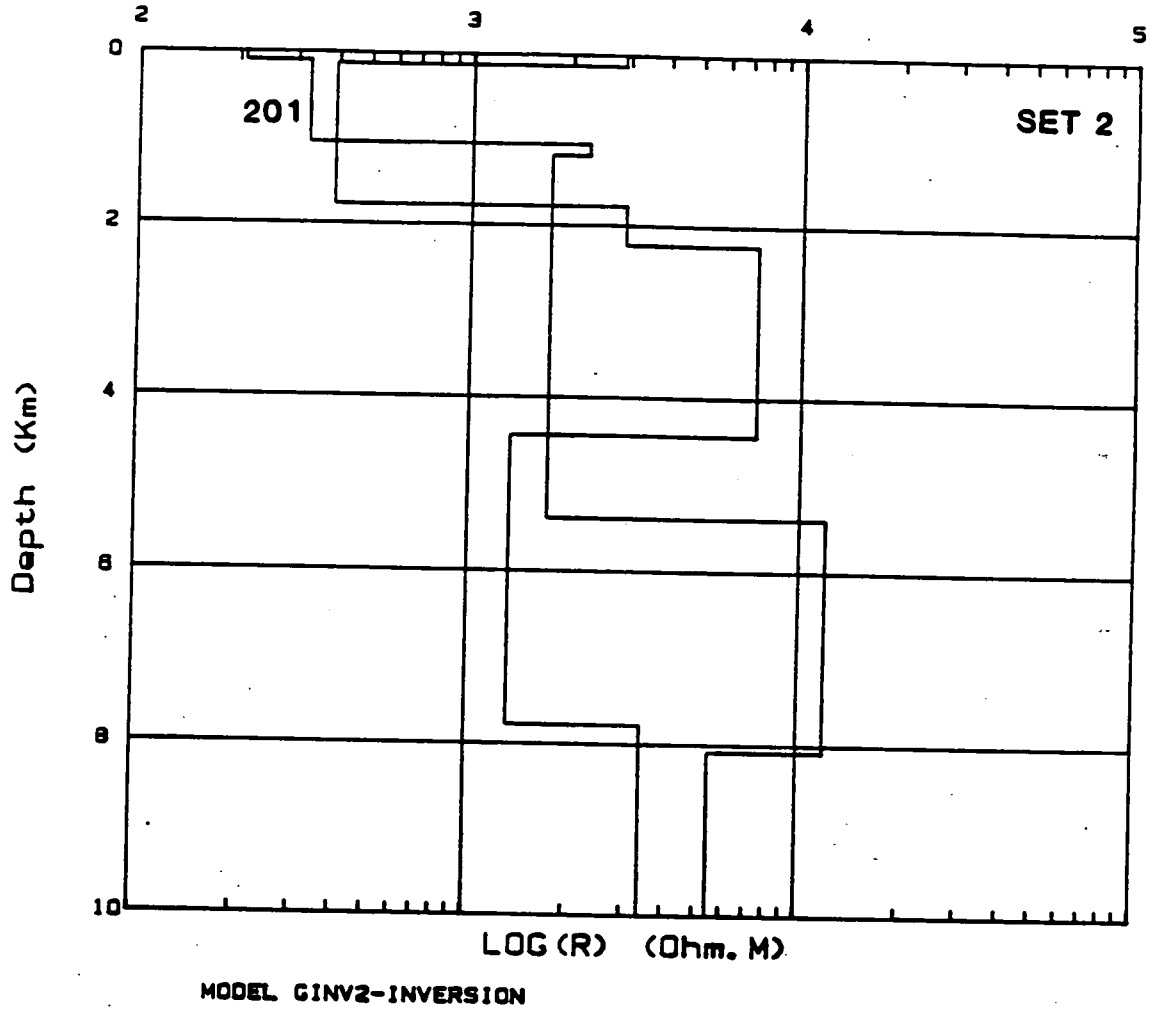

Figure 5.14. Minimum-norm, layered inversion results for survey data grouped into the 3 standard SETS. (a) SET 1, sites 101-107, (b) SET 1, sites 109-112 and (c) SET 2, sites 201-202.

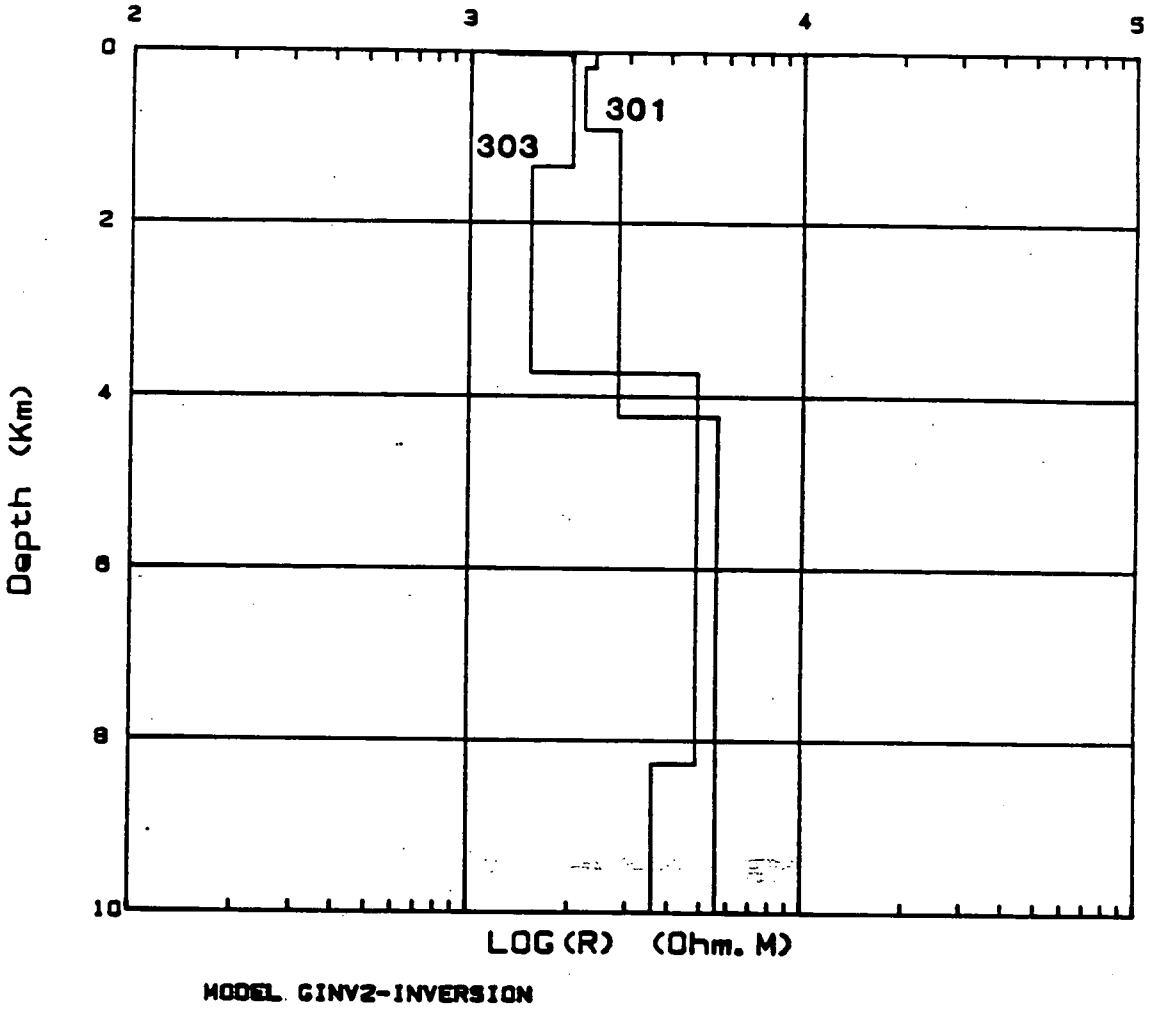

Figure 5.15. Minimum-norm, layered inversion results for SET 3 survey sites 301 and 303.

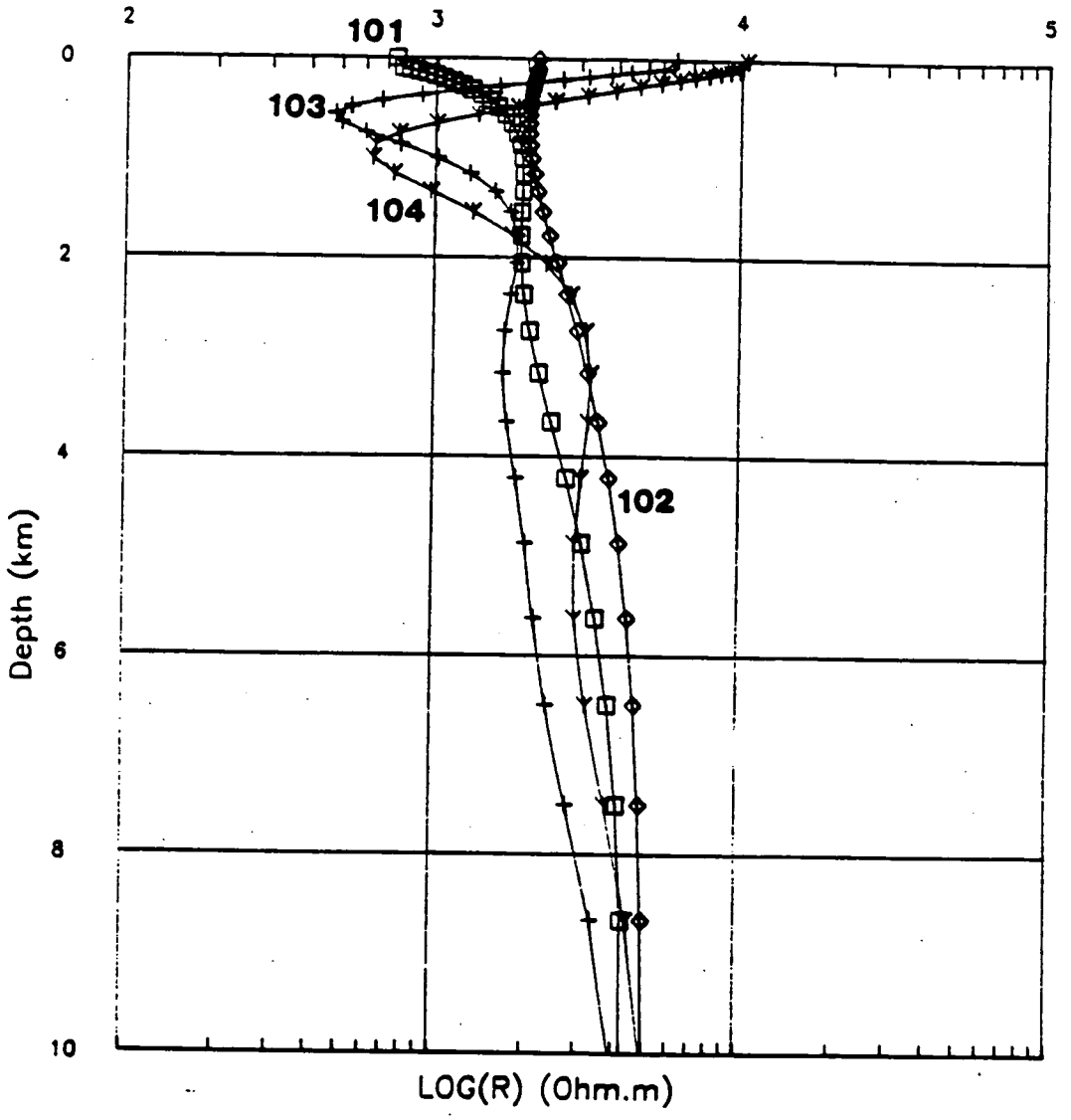

Figure 5.16. Most-smooth inversion results for the SET 1 survey data. **(a)** sites 101-104, **(b)** sites 105-107 and **(c)** sites 109-112.

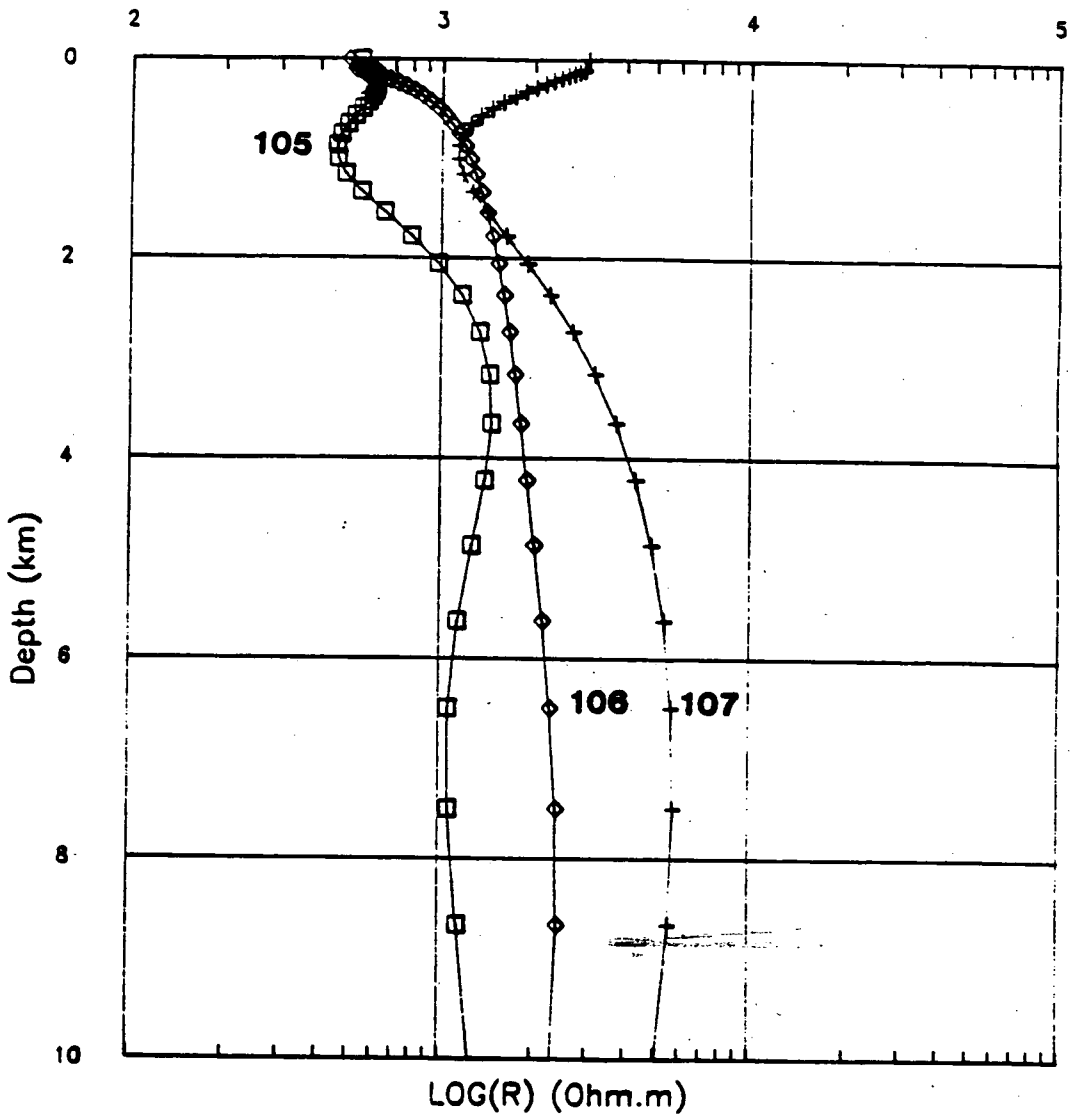

Figure 5.16. Most-smooth inversion results for the SET 1 survey data. **(a)** sites 101-104, **(b)** sites 105-107 and **(c)** sites 109-112.

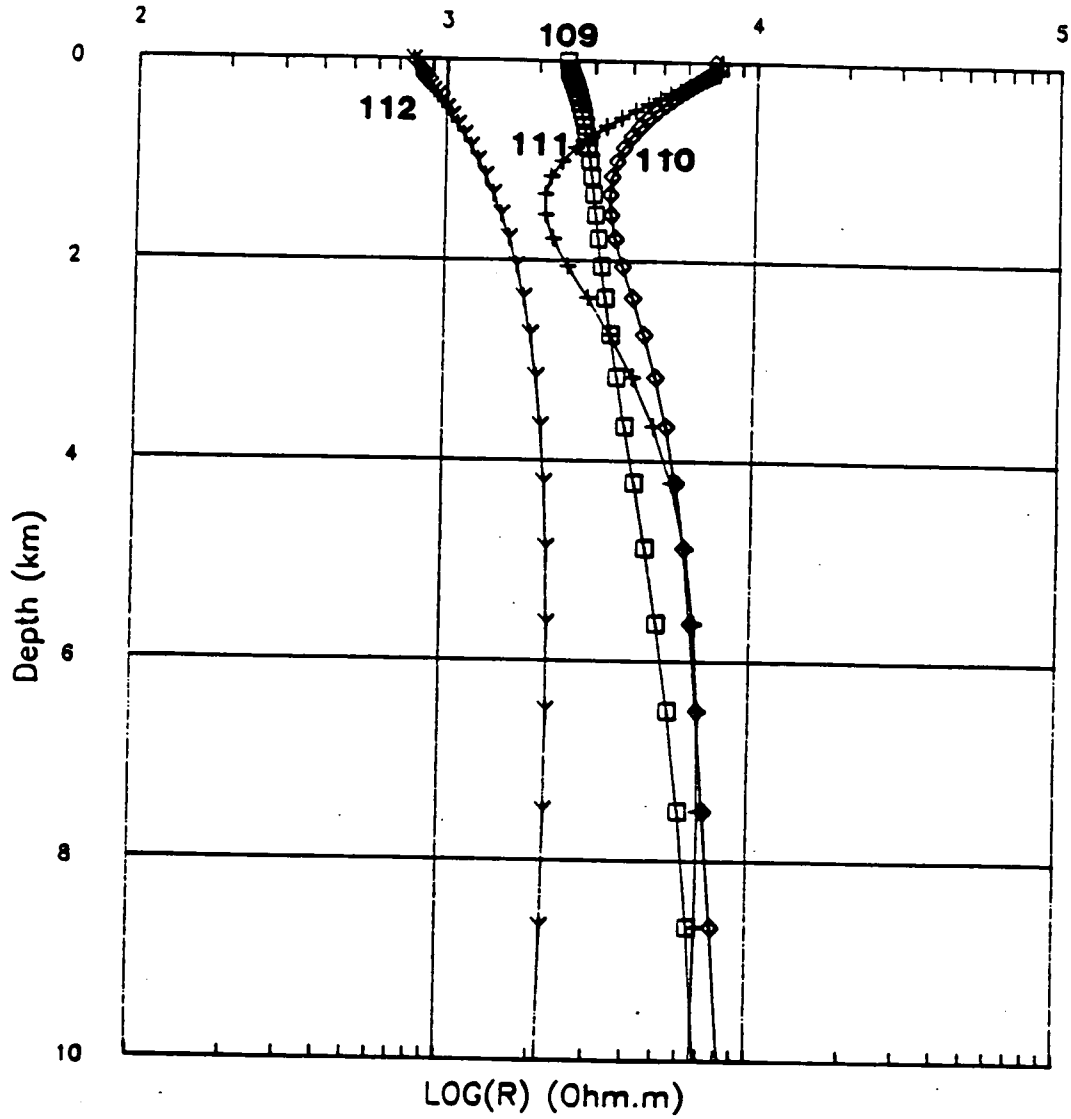

Figure 5.16. Most-smooth inversion results for the SET 1 survey data. (a) sites 101-104, (b) sites 105-107 and (c) sites 109-112.

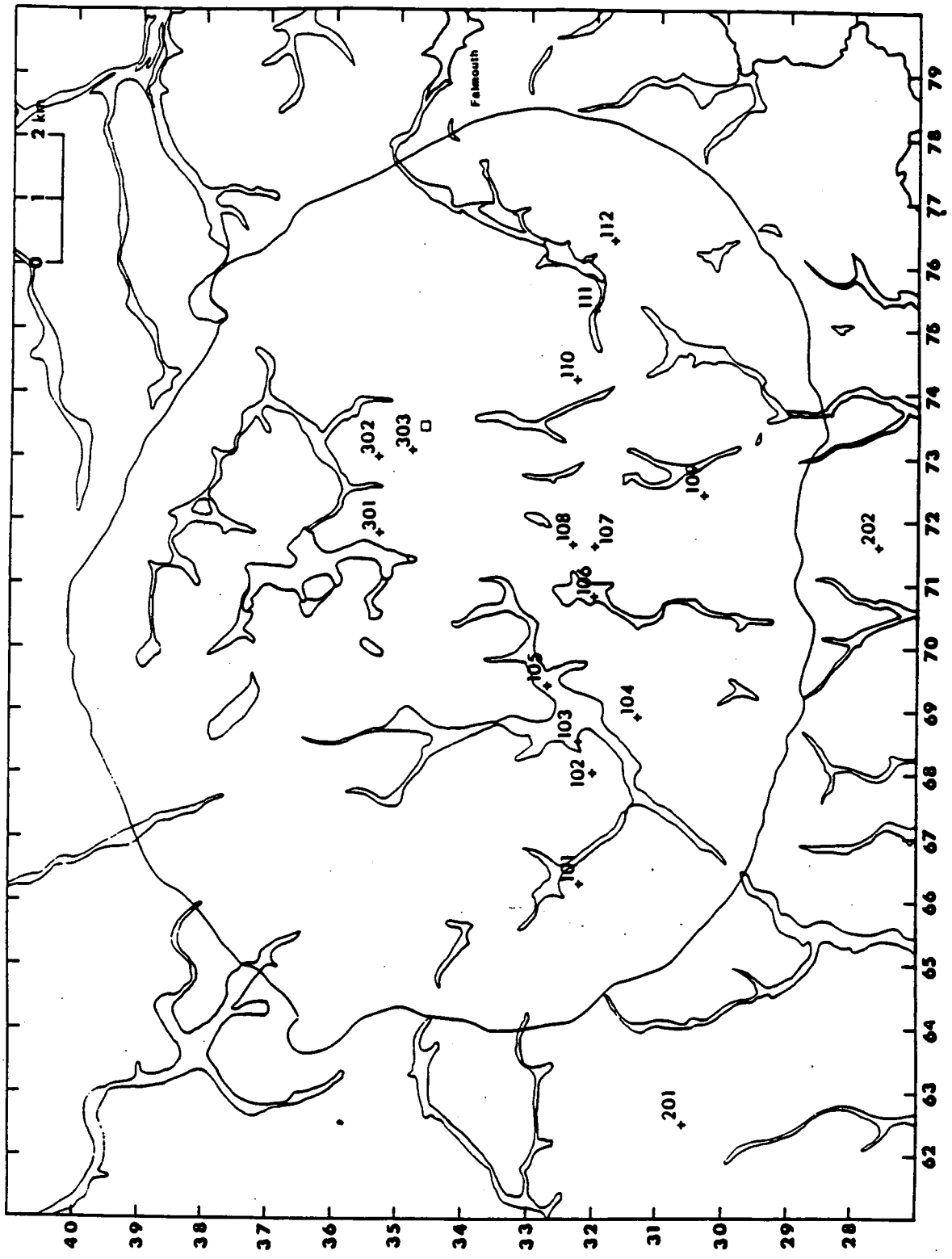

Figure 5.17. Survey locations in relation to the alluviam deposits which also trace the present-day drainage pattern.

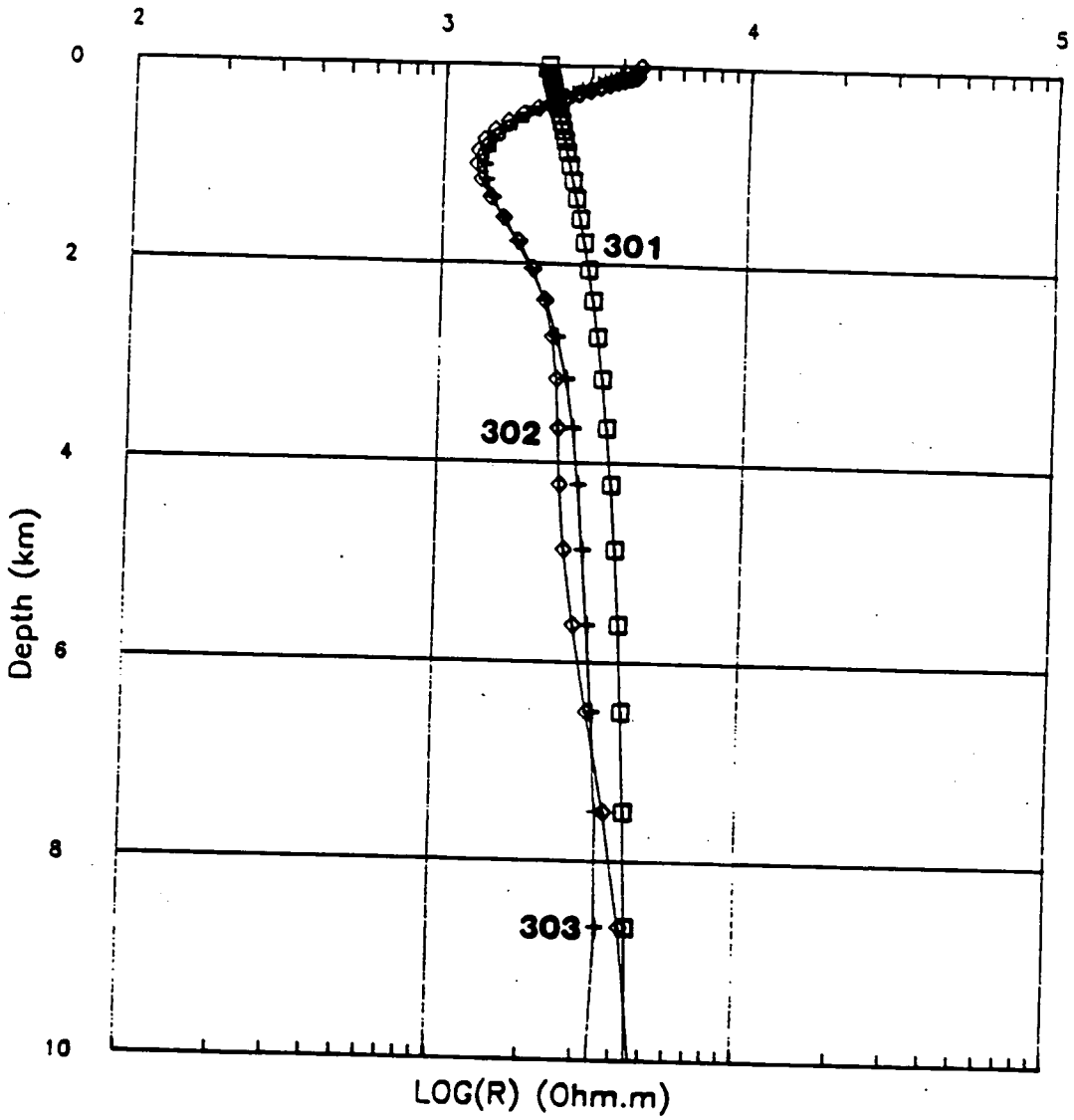

Figure 5.18. Most-smooth inversion results for the SET 3 survey data.

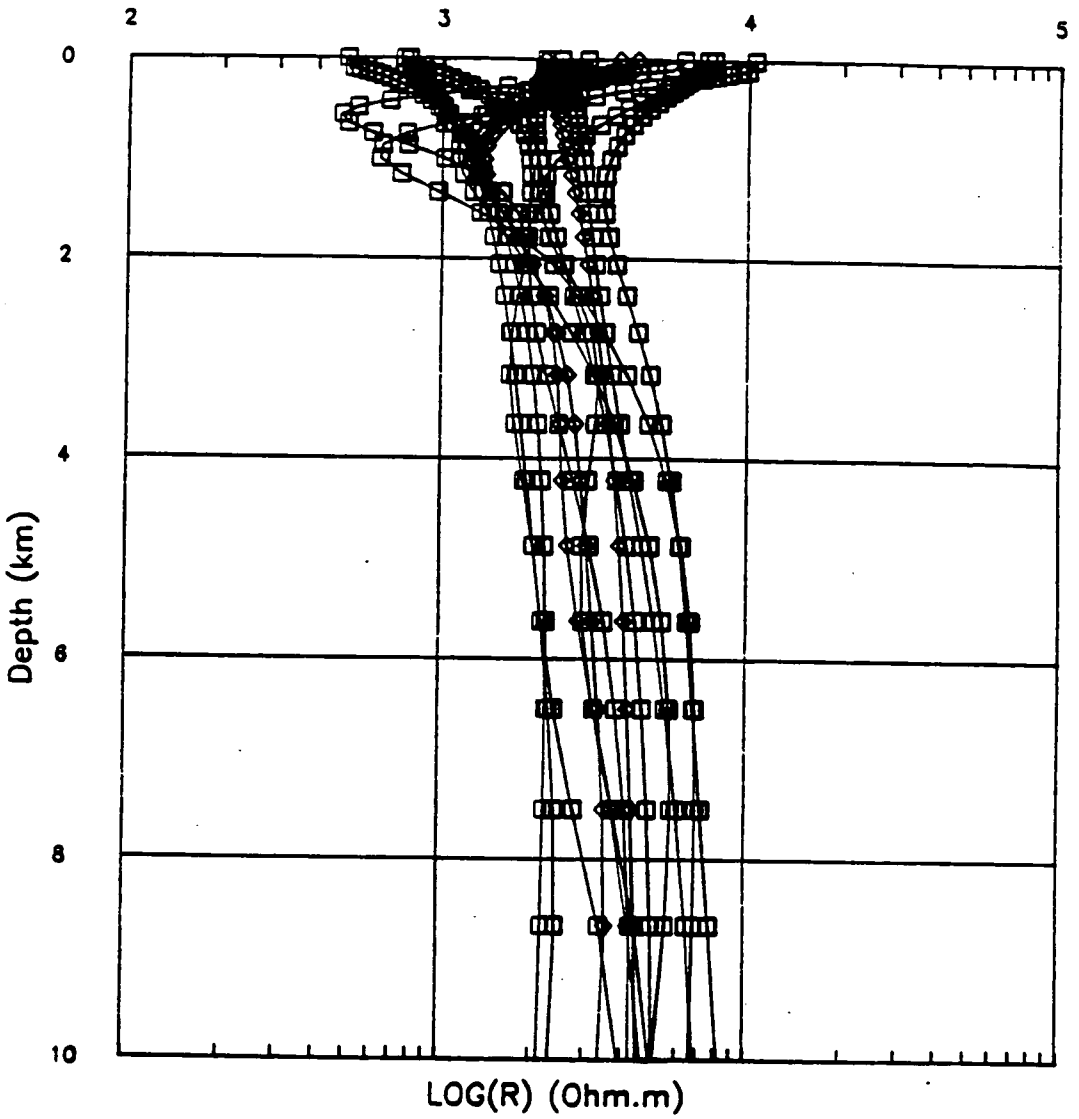

Figure 5.19. Most-smooth inversion results for all sites on the granite but excluding site 105.

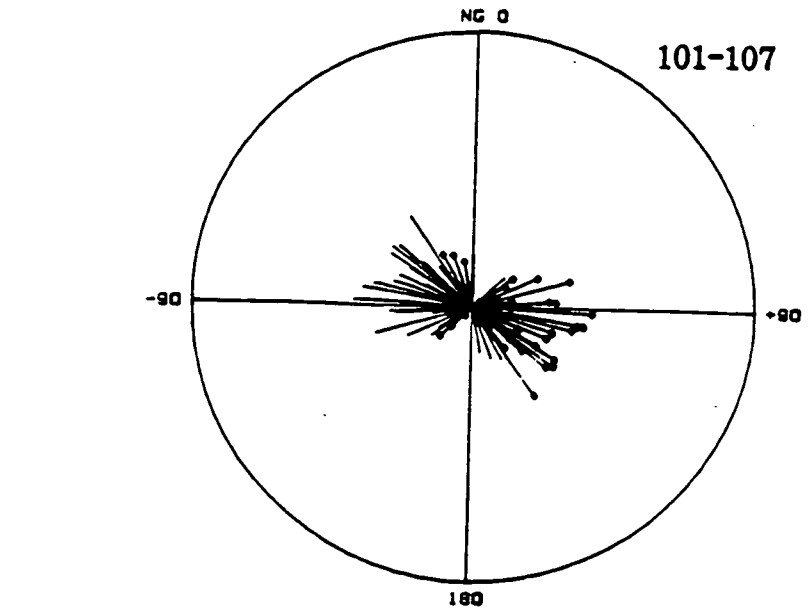

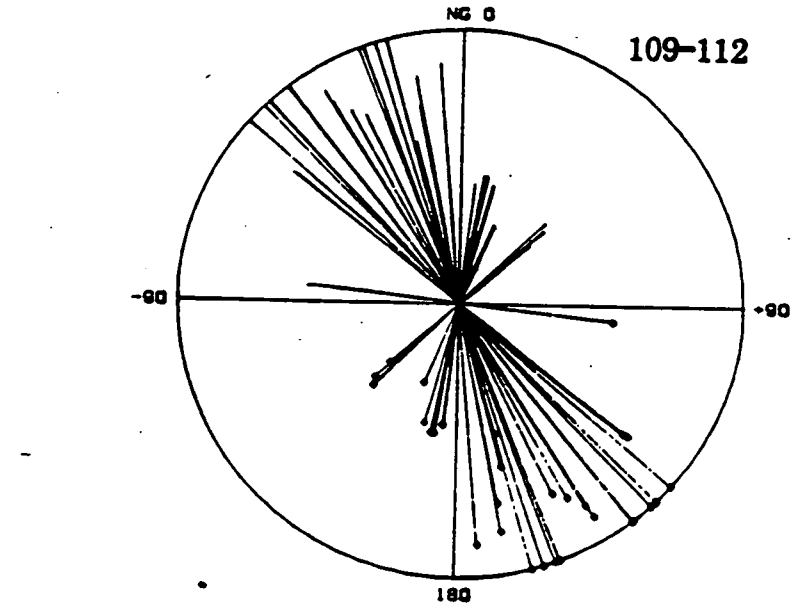

Figure 5.20. Amplitudes and azimuths of real (Gr) and imaginary (Gi) induction arrows for four decades decreasing in frequency. Results are separated into two groups (i) sites 101-107 and (ii) sites 109-112. Real results are followed by imaginary results in each case. Reference circle diameter is 0.5 for real and 0.25 for imaginary. Decades are denoted by IDEC. (a) IDEC=1.real: (b) IDEC=1.imag. (c) IDEC=2.real; (d) IDEC=2.imag. (e) IDEC=3.real: (f) IDEC=3.imag. (g) IDEC=4.real: (h) IDEC=4.imag.

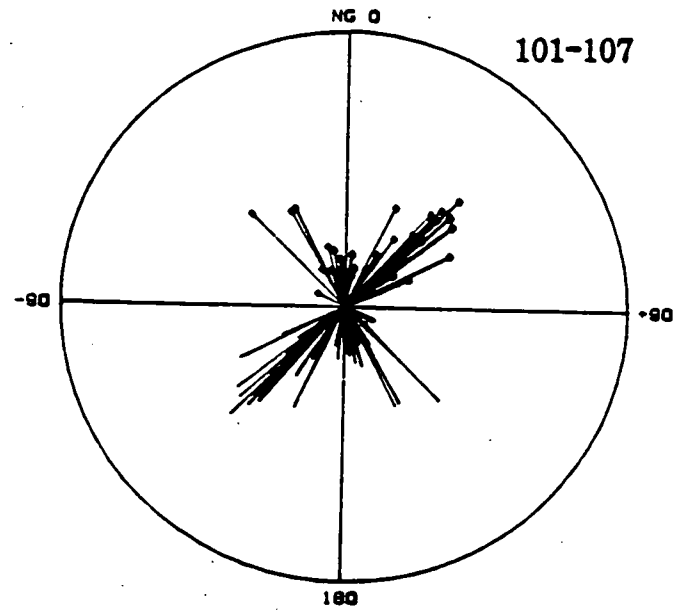

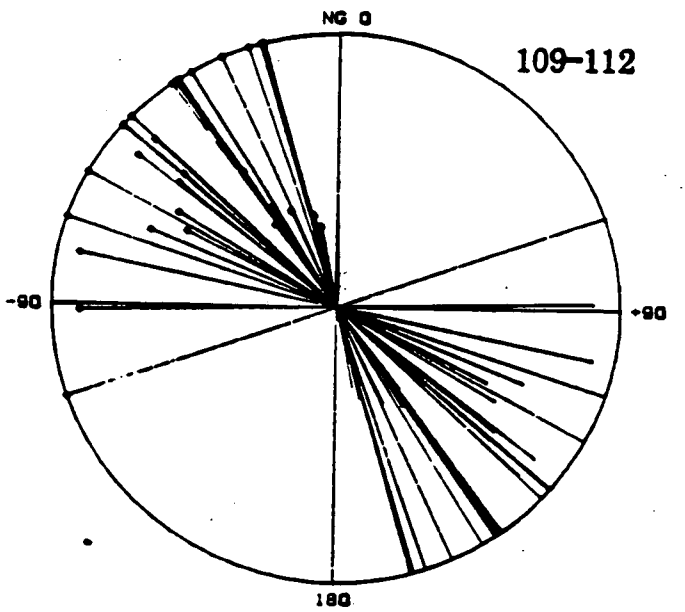

Figure 5.20. Amplitudes and azimuths of real (Gr) and imaginary (Gi) induction arrows for four decades decreasing in frequency. Results are separated into two groups (i) sites 101-107 and (ii) sites 109-112. Real results are followed by imaginary results in each case. Reference circle diameter is 0.5 for real and 0.25 for imaginary. Decades are denoted by IDEC. (a) IDEC=1.real: (b) IDEC=1.imag. (c) IDEC=2.real; (d) IDEC=2.imag. (e) IDEC=3.real: (f) IDEC=3.imag. (g) IDEC=4.real: (h) IDEC=4.imag.

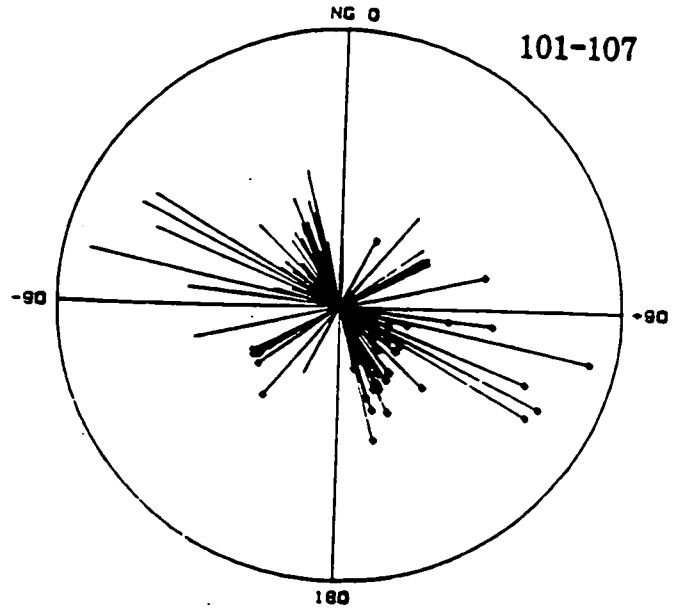

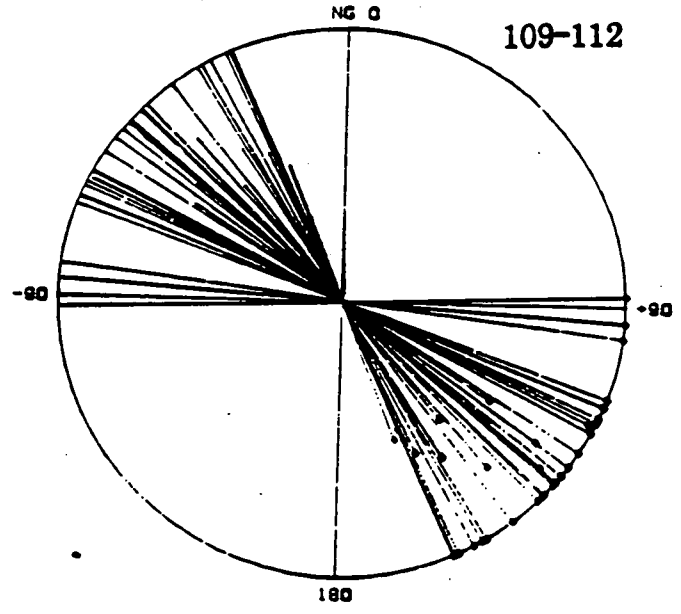

Figure 5.20. Amplitudes and azimuths of real (Gr) and imaginary (Gi) induction arrows for four decades decreasing in frequency. Results are separated into two groups (i) sites 101-107 and (ii) sites 109-112. Real results are followed by imaginary results in each case. Reference circle diameter is 0.5 for real and 0.25 for imaginary. Decades are denoted by IDEC. (a) IDEC=1.real: (b) IDEC=1.imag. (c) IDEC=2.real: (d) IDEC=2.imag. (e) IDEC=3.real: (f) IDEC=3.imag. (g) IDEC=4.real: (h) IDEC=4.imag.

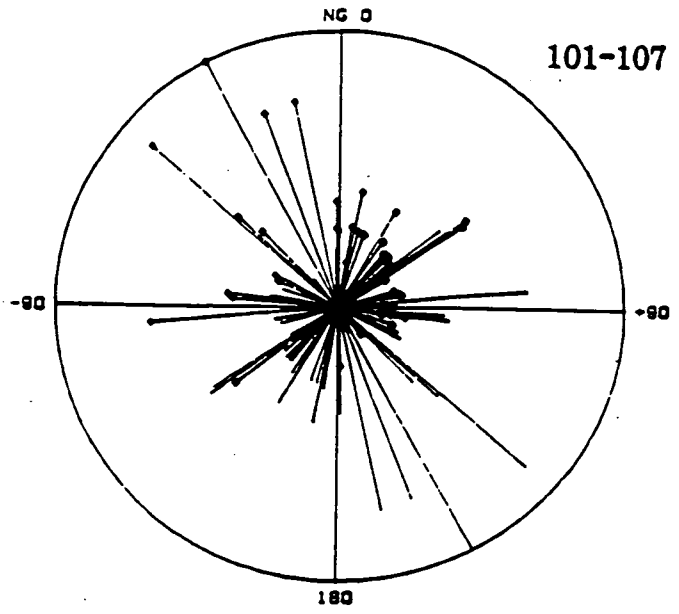

IDEC 2 VERTICAL FIELD TF AZIMUTHS <Gi> DIA 0.25

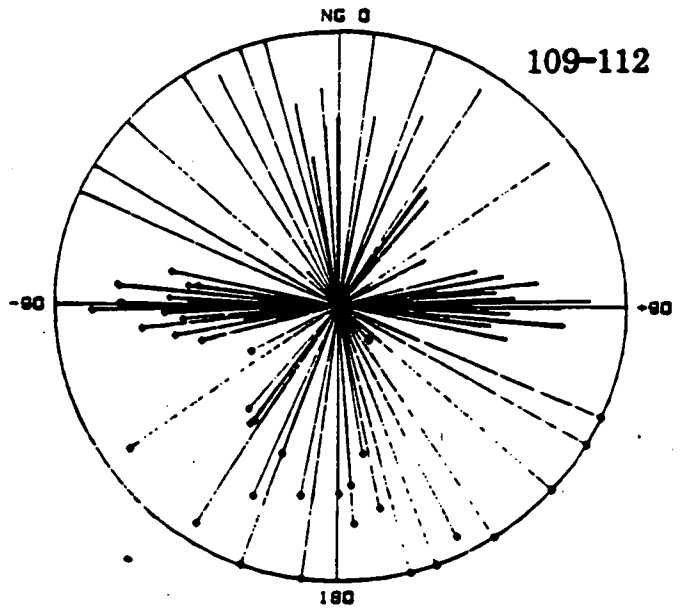

IDEC 2 VERTICAL FIELD TF AZIMUTHS <Gi> DIA 0.25

Figure 5.20. Amplitudes and azimuths of real (Gr) and imaginary (Gi) induction arrows for four decades decreasing in frequency. Results are separated into two groups (i) sites 101-107 and (ii) sites 109-112. Real results are followed by imaginary results in each case. Reference circle diameter is 0.5 for real and 0.25 for imaginary. Decades are denoted by IDEC. (a) IDEC=1.real: (b) IDEC=1.imag. (c) IDEC=2.real; (d) IDEC=2.imag. (e) IDEC=3.real: (f) IDEC=3.imag. (g) IDEC=4.real: (h) IDEC=4.imag.

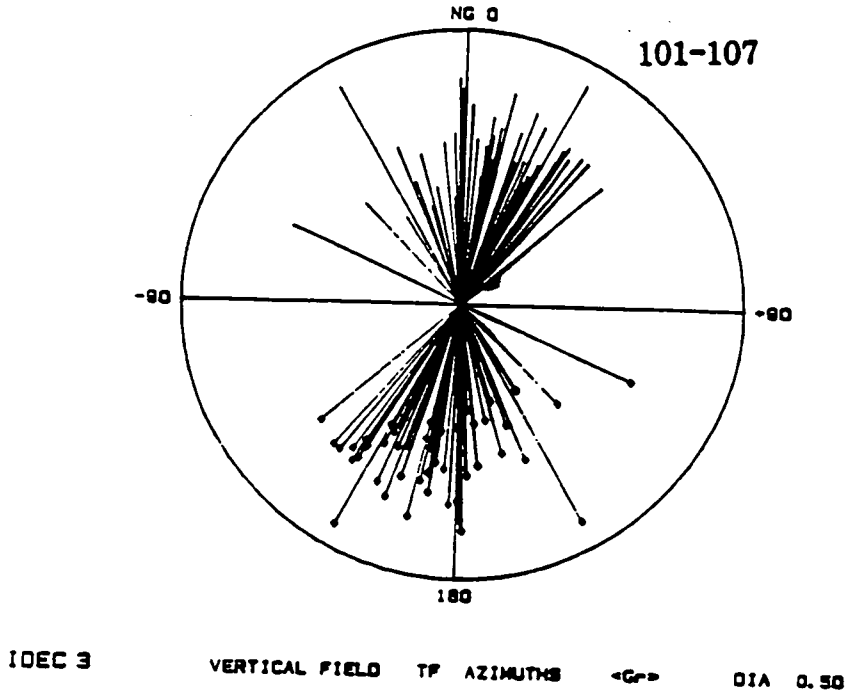

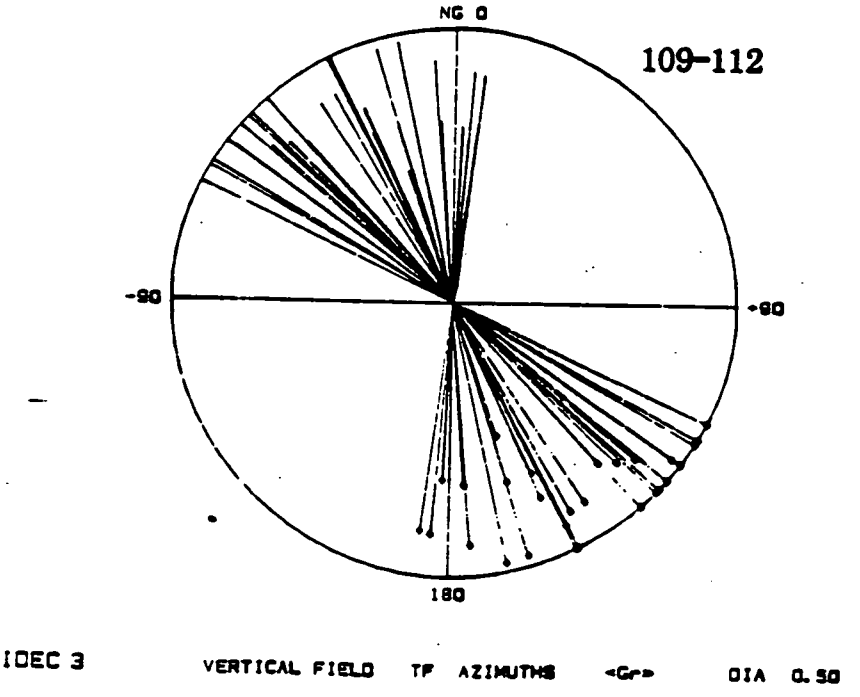

Figure 5.20. Amplitudes and azimuths of real (Gr) and imaginary (Gi) induction arrows for four decades decreasing in frequency. Results are separated into two groups (i) sites 101-107 and (ii) sites 109-112. Real results are followed by imaginary results in each case. Reference circle diameter is 0.5 for real and 0.25 for imaginary. Decades are denoted by IDEC. (a) IDEC=1.real: (b) IDEC=1.imag. (c) IDEC=2.real; (d) IDEC=2.imag. (e) IDEC=3.real: (f) IDEC=3.imag. (g) IDEC=4.real: (h) IDEC=4.imag.

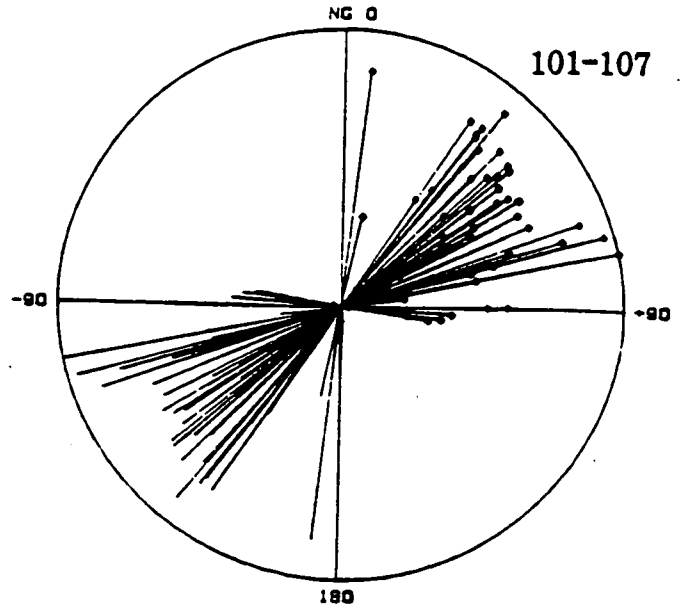

IDEC 3 VERTICAL FIELD TF AZIMUTHS <Gi> DIA 0.25

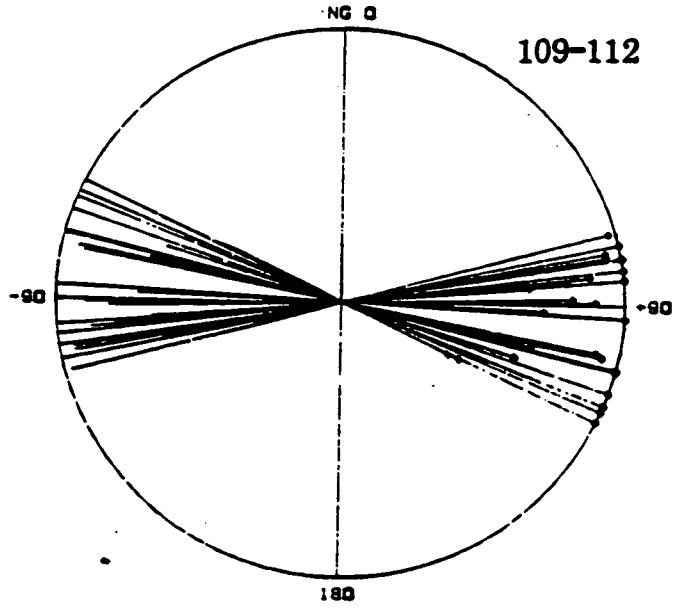

IDEC 3 VERTICAL FIELD TF AZIMUTHS <Gi> DIA 0.25

Figure 5.20. Amplitudes and azimuths of real (Gr) and imaginary (Gi) induction arrows for four decades decreasing in frequency. Results are separated into two groups (i) sites 101-107 and (ii) sites 109-112. Real results are followed by imaginary results in each case. Reference circle diameter is 0.5 for real and 0.25 for imaginary. Decades are denoted by IDEC. (a) IDEC=1.real: (b) IDEC=1.imag. (c) IDEC=2.real; (d) IDEC=2.imag. (e) IDEC=3.real: (f) IDEC=3.imag. (g) IDEC=4.real: (h) IDEC=4.imag.

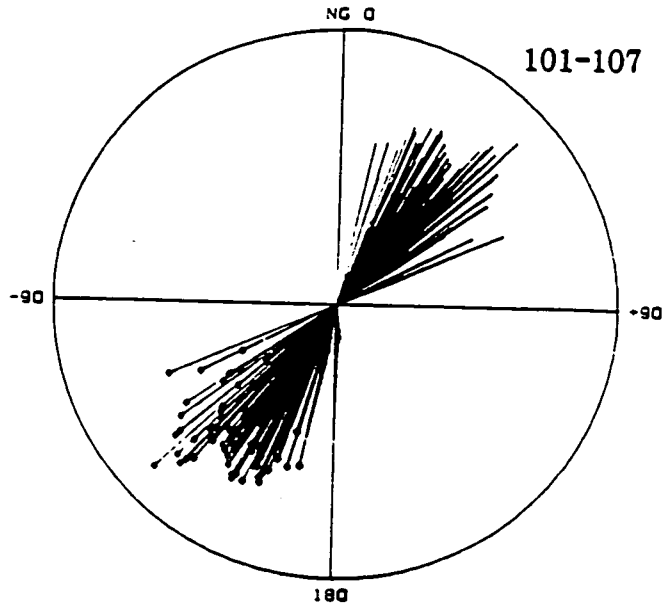

IDEC 4 VERTICAL FIELD TF AZIMUTHS <Gr> DIA 0.50

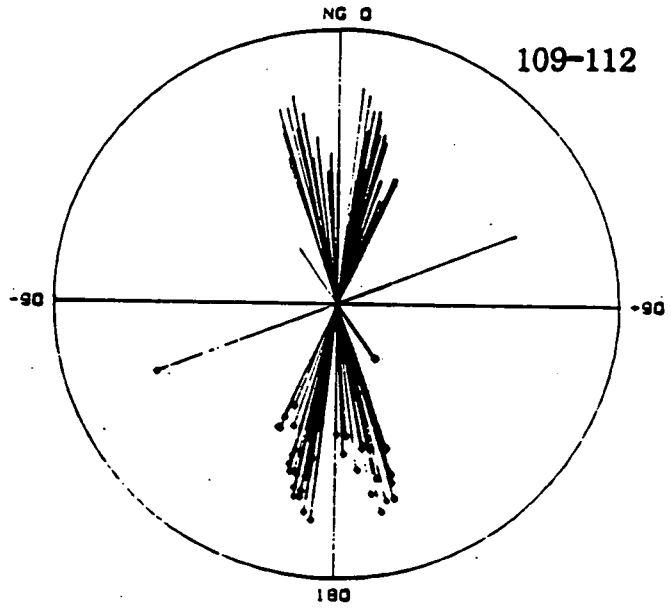

IDEC 4 VERTICAL FIELD TF AZIMUTHS <Gr> DIA 0.50

Figure 5.20. Amplitudes and azimuths of real (Gr) and imaginary (Gi) induction arrows for four decades decreasing in frequency. Results are separated into two groups (i) sites 101-107 and (ii) sites 109-112. Real results are followed by imaginary results in each case. Reference circle diameter is 0.5 for real and 0.25 for imaginary. Decades are denoted by IDEC. (a) IDEC=1.real: (b) IDEC=1.imag. (c) IDEC=2.real; (d) IDEC=2.imag. (e) IDEC=3.real: (f) IDEC=3.imag. (g) IDEC=4.real: (h) IDEC=4.imag.

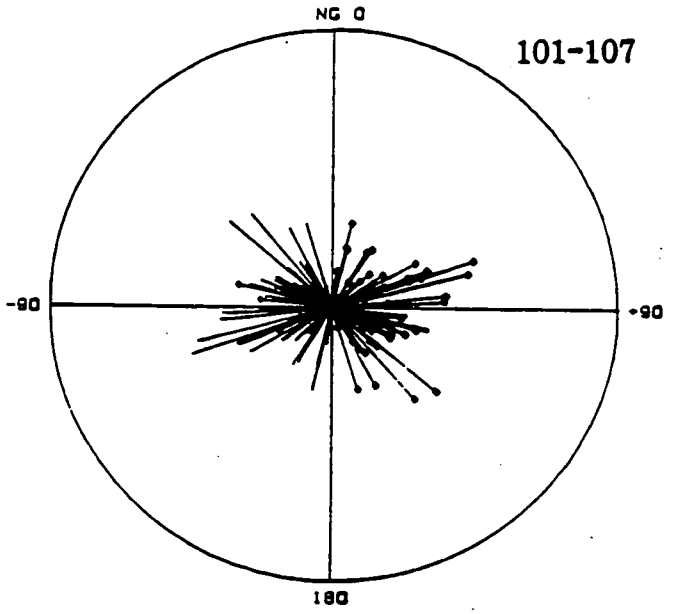

IDEC 4 VERTICAL FIELD TF AZIMUTHS <Gi> DIA 0.25

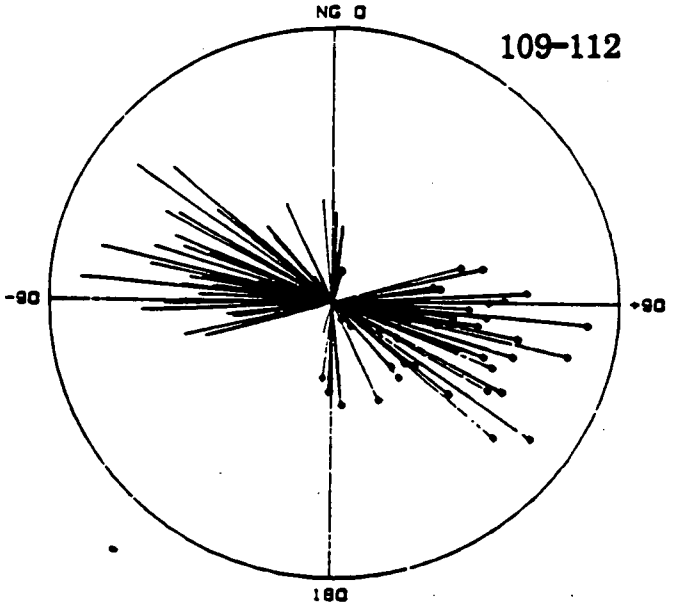

IDEC 4 VERTICAL FIELD TF AZIMUTHS <Gi> DIA 0.25

Figure 5.20. Amplitudes and azimuths of real (Gr) and imaginary (Gi) induction arrows for four decades decreasing in frequency. Results are separated into two groups (i) sites 101-107 and (ii) sites 109-112. Real results are followed by imaginary results in each case. Reference circle diameter is 0.5 for real and 0.25 for imaginary. Decades are denoted by IDEC. (a) IDEC=1,real: (b) IDEC=1,imag. (c) IDEC=2,real: (d) IDEC=2,imag. (e) IDEC=3,real: (f) IDEC=3,imag. (g) IDEC=4,real: (h) IDEC=4,imag.

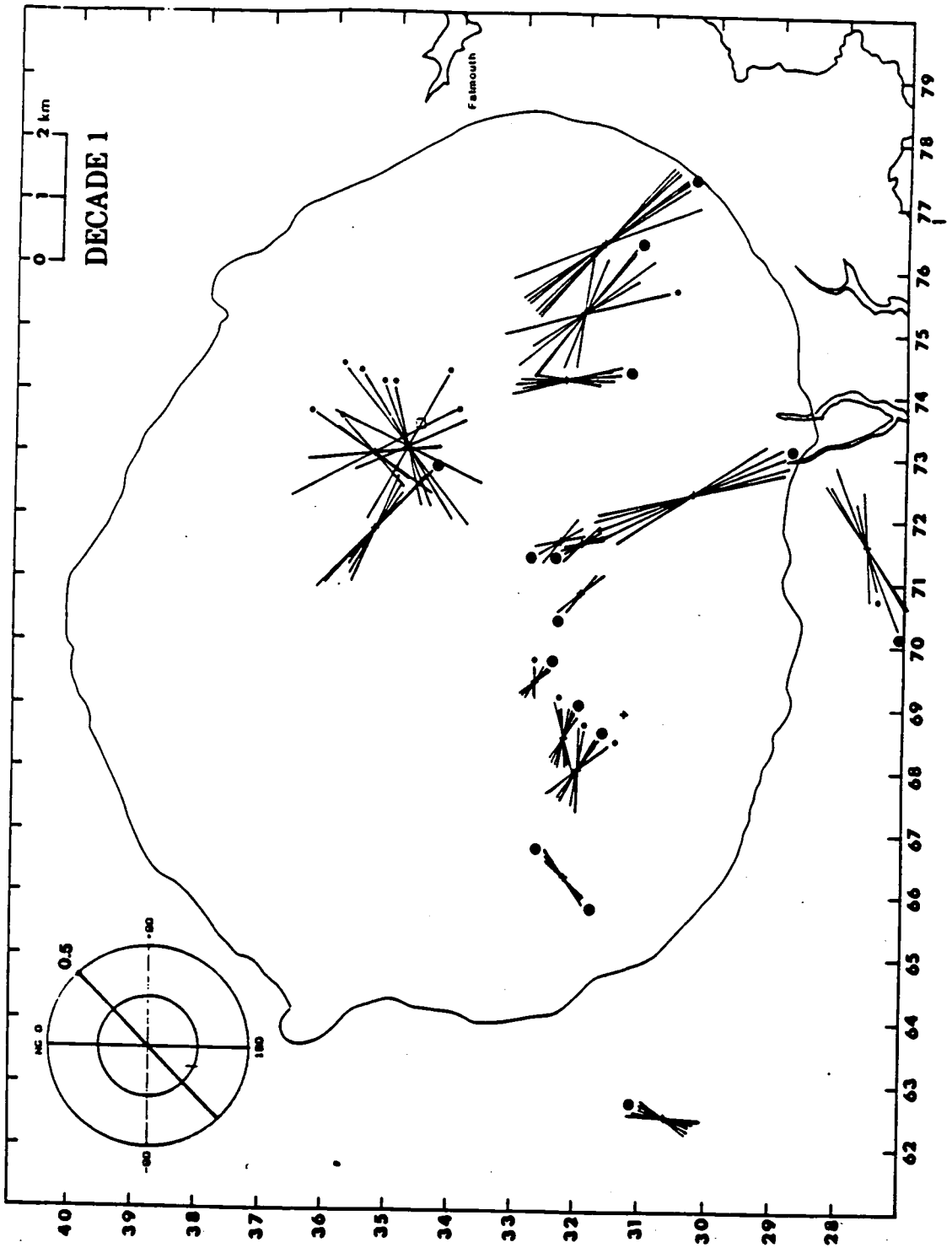

Figure 5.21. Maps of maximum response of vertical magnetic field for four decades decreasing in frequency. (a) Decade 1, (b) Decade 2, (c) Decade 3 and (d) Decade 4. Reference circle diameter is 0.5 throughout. Dots denote azimuthal direction.

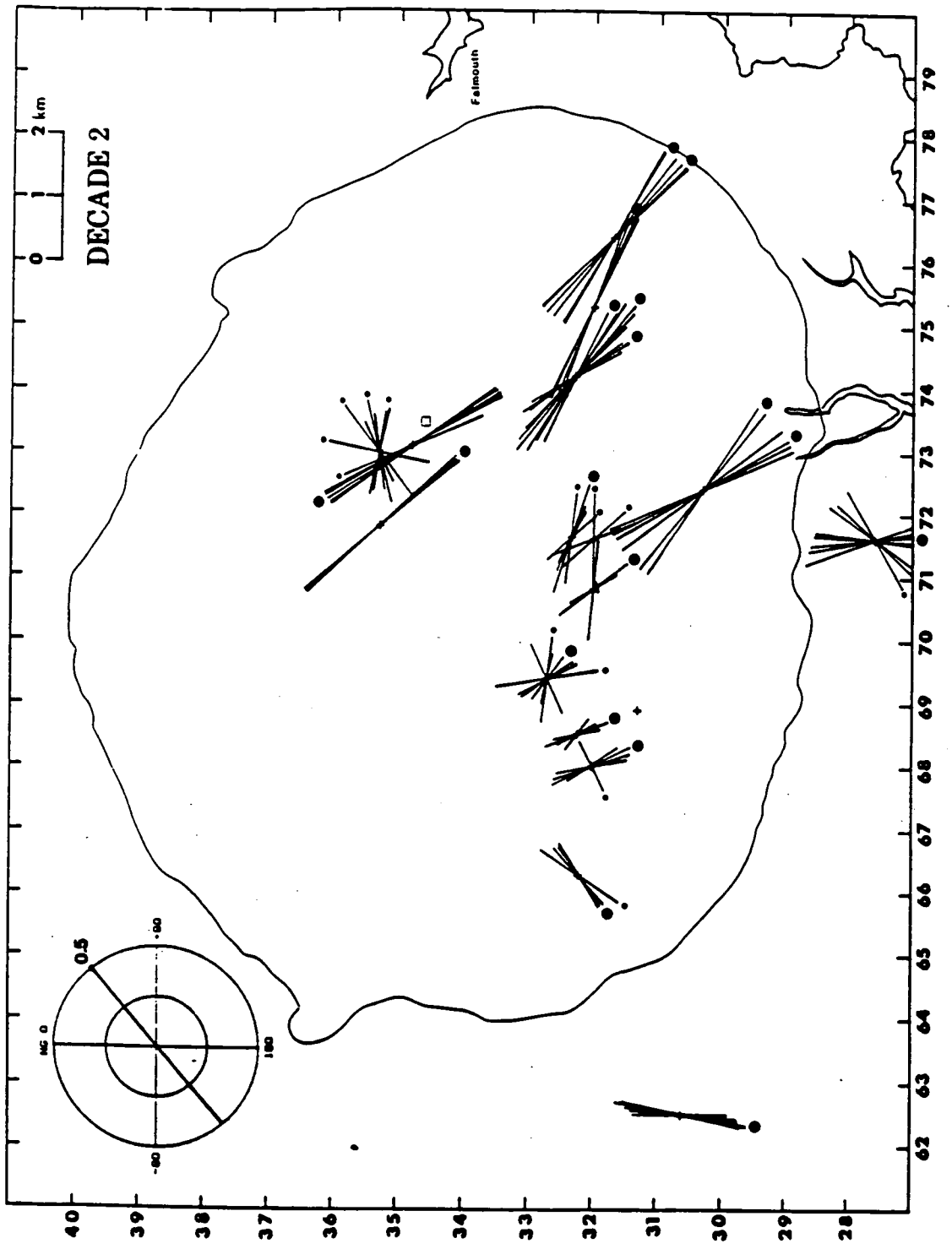

Figure 5.21. Maps of maximum response of vertical magnetic field for four decades decreasing in frequency. (a) Decade 1, (b) Decade 2, (c) Decade 3 and (d) Decade 4. Reference circle diameter is 0.5 throughout. Dots denote azimuthal direction.

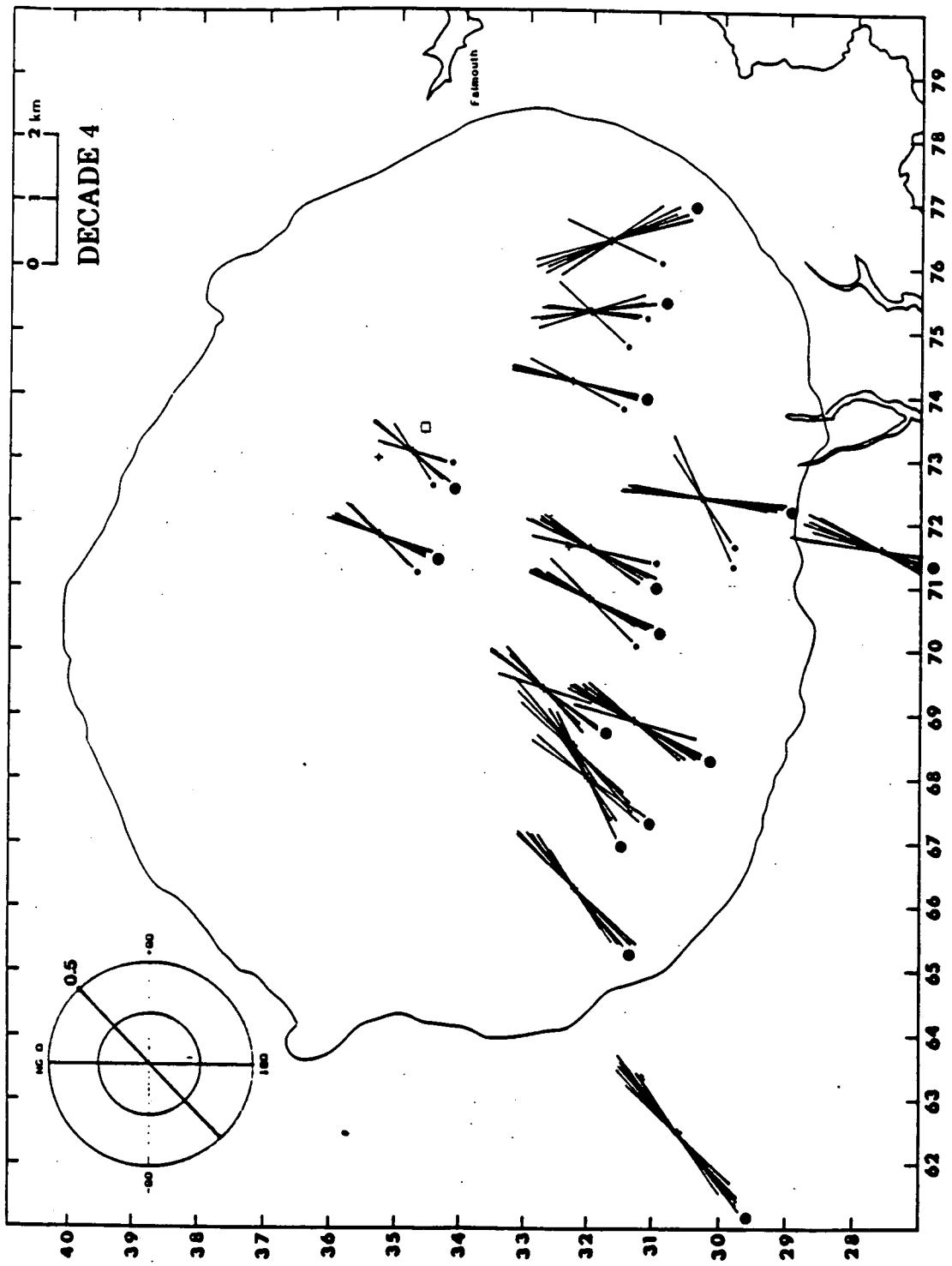

Figure 5.21. Maps of maximum response of vertical magnetic field for four decades decreasing in frequency. **(a)** Decade 1. **(b)** Decade 2. **(c)** Decade 3 and **(d)** Decade 4. Reference circle diameter is 0.5 throughout. Dots denote azimuthal direction.

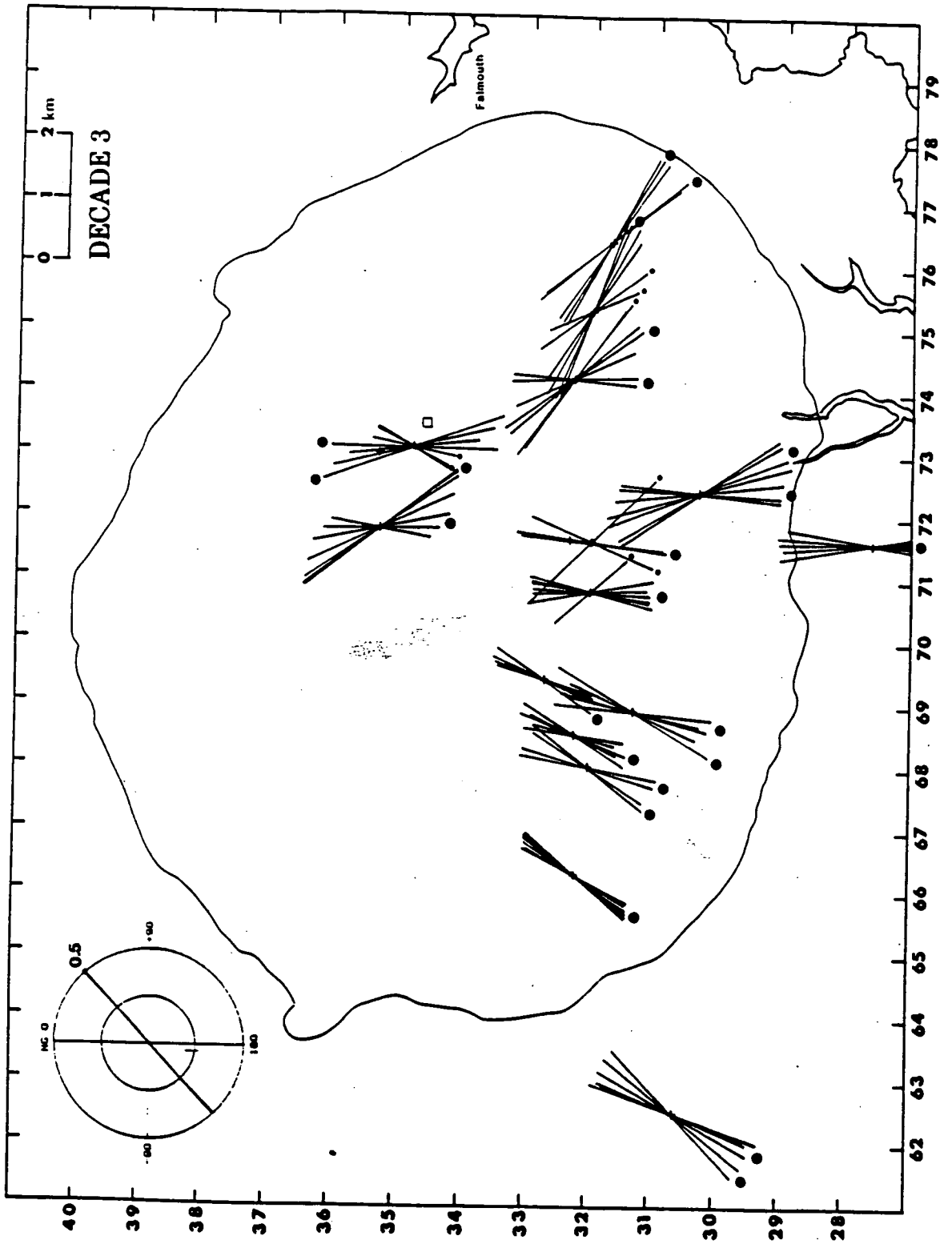

Figure 5.21. Maps of maximum response of vertical magnetic field for four decades decreasing in frequency. **(a)** Decade 1, **(b)** Decade 2, **(c)** Decade 3 and **(d)** Decade 4. Reference circle diameter is 0.5 throughout. Dots denote azimuthal direction.

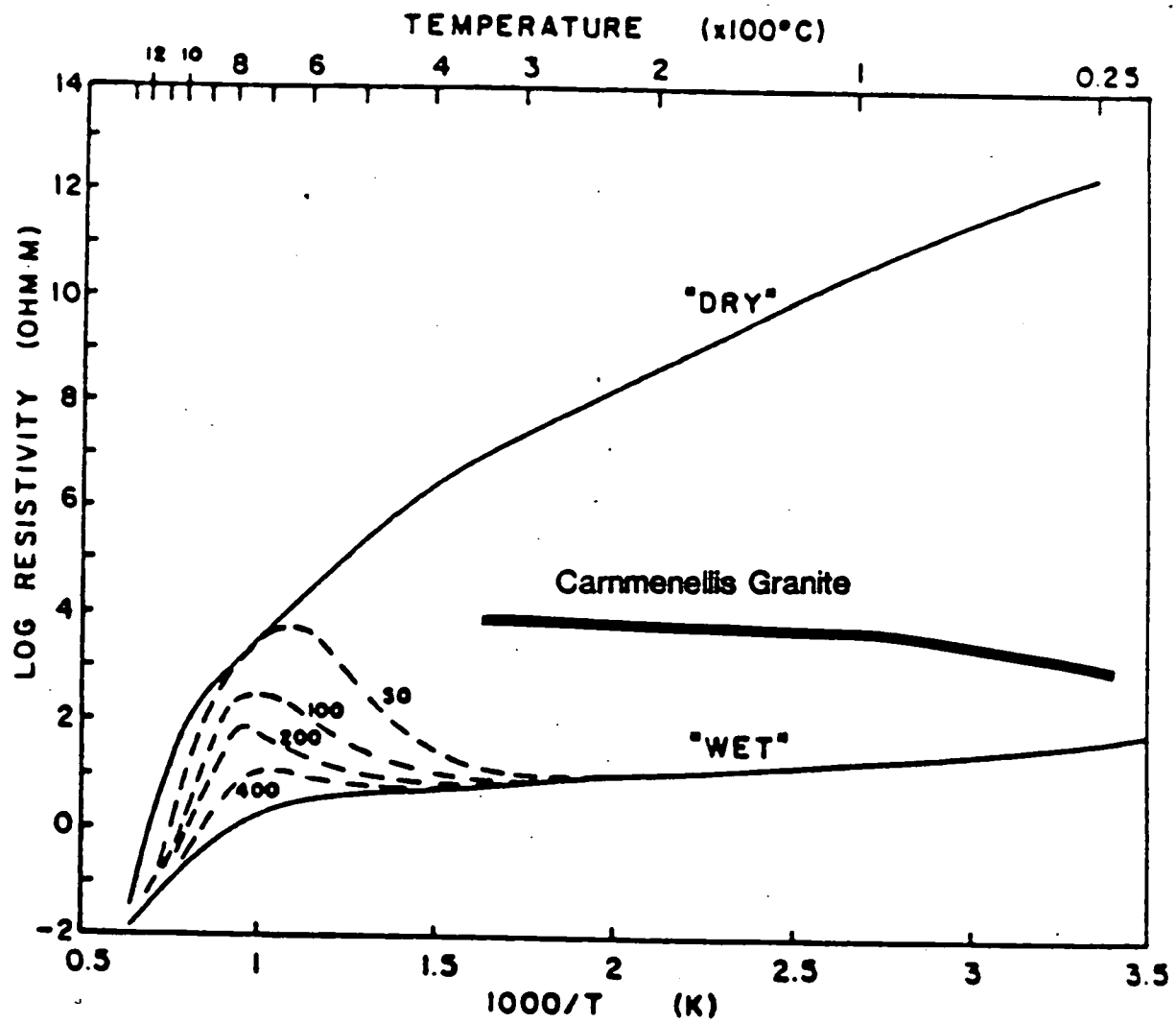

Figure 6.1. Typical variation of granite resistivity with temperature after Olhoeft (1981). Summary plot showing bounding 'dry' and 'wet' curves to indicate water content (i.e. degree of saturation). The dashed lines are for various water pressures in MPa for water salinities less than 0.1 molar NaCl. Also shown is the mean resistivity variation for the Carnmenellis granite down to 10 km (about 360 degrees C).

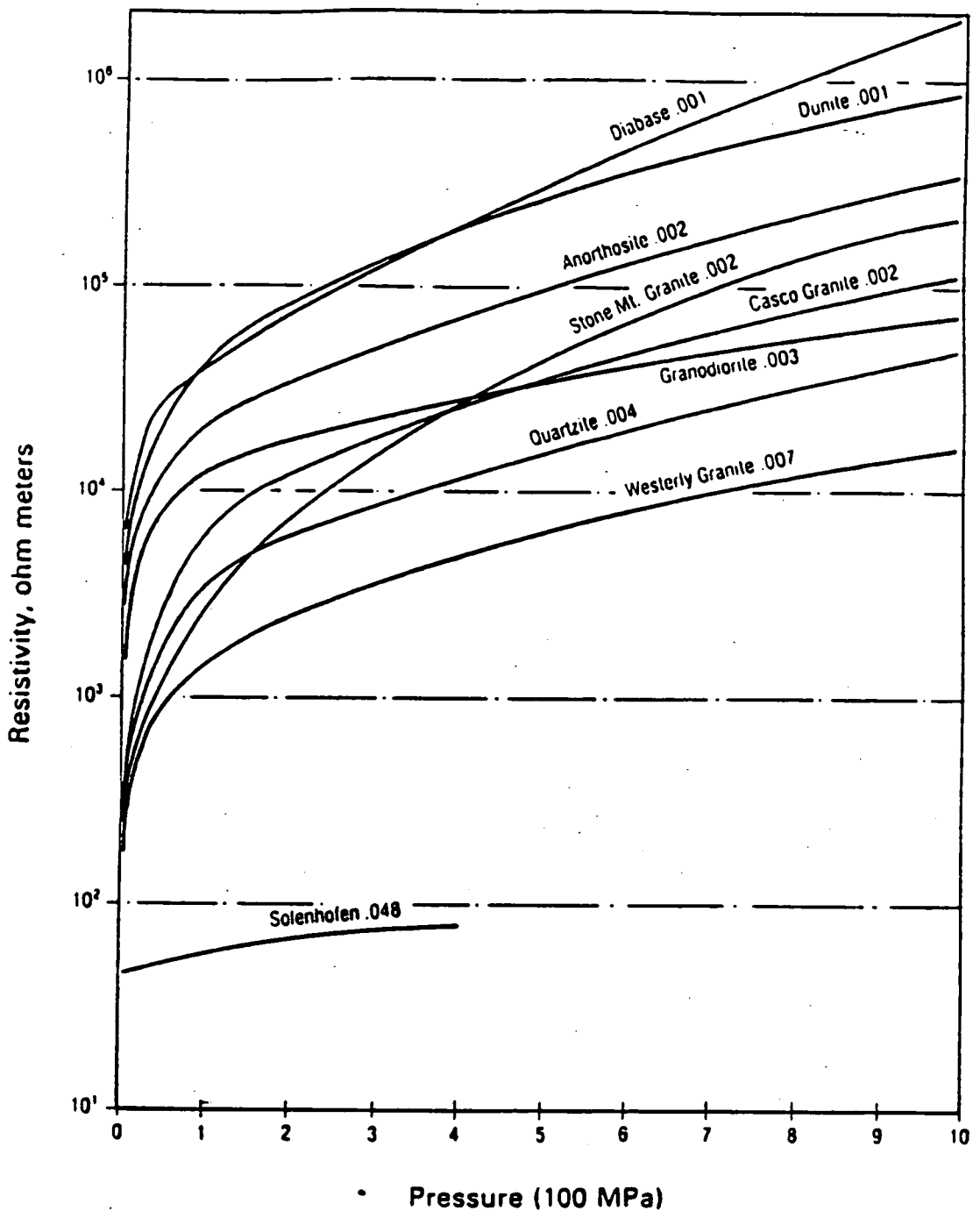

Figure 6.2. Resistivity as a function of pressure in 0.3 ohm.m NaCl, after Brace et al. (1965). The numbers refer to the values of the pore porosity at zero pressure. Pressure in uits of 100 MPa (100 MPa = 1 kbar).

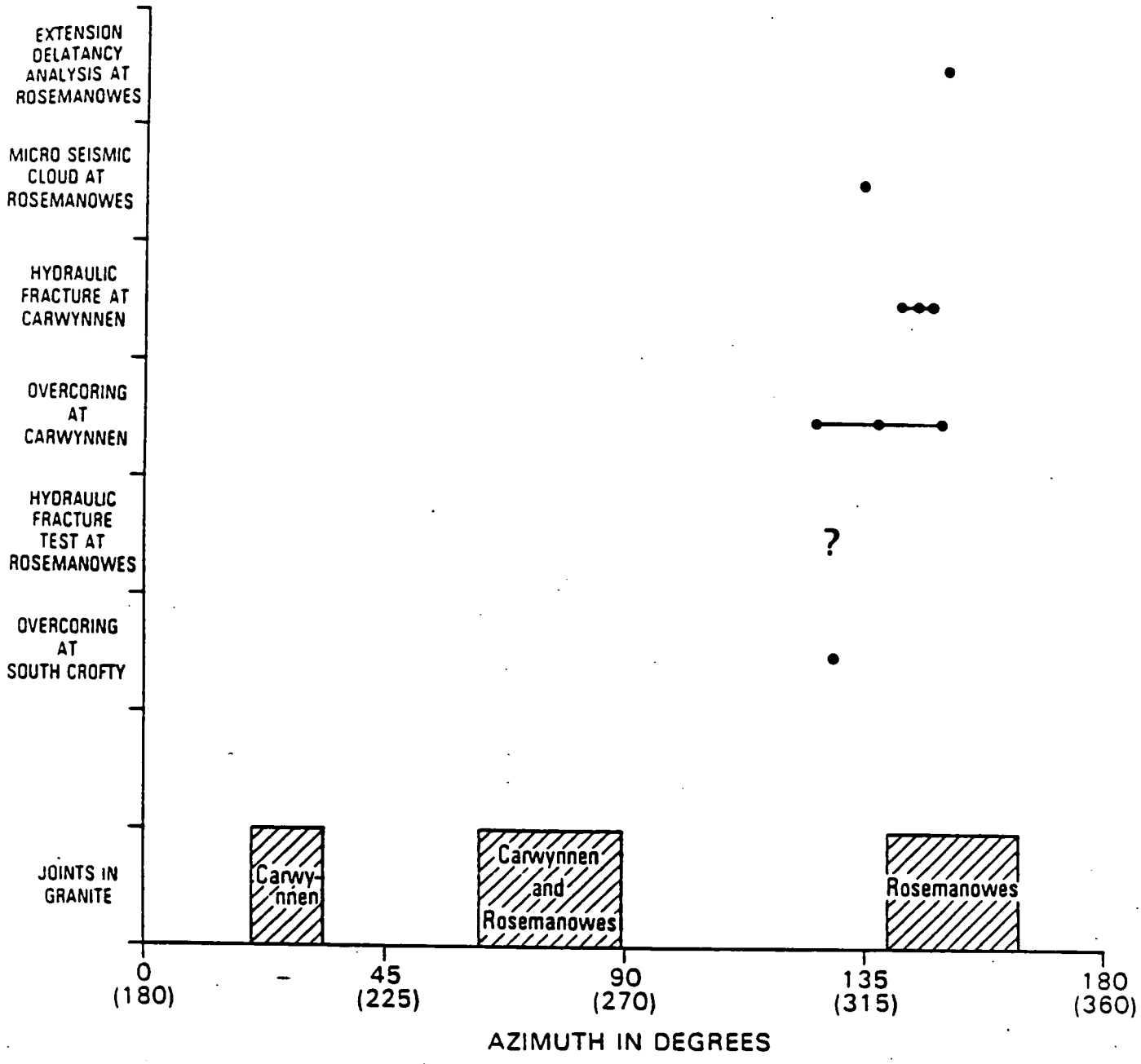

Compilation of all available stress indicators from Cornwall Batholith.

Figure 6.3. Compilation of all available stress indicators from the Cornubian batholith. From Evans (1987).

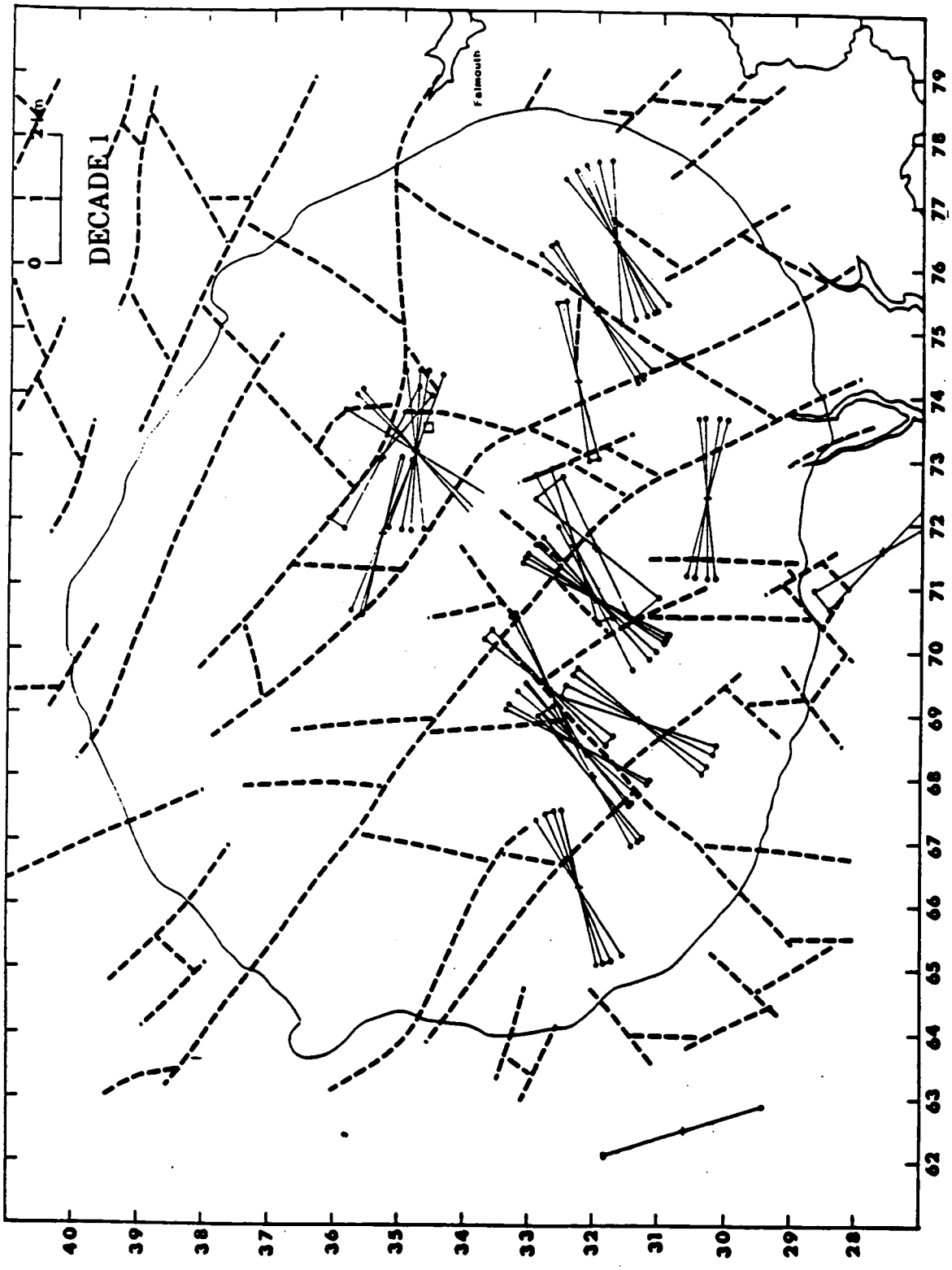

Figure 7.1. Map of azimuths of maximum resistivity for Decade 1 (from Figure 5.8a) and major fracture lineations from Figure 3.4.

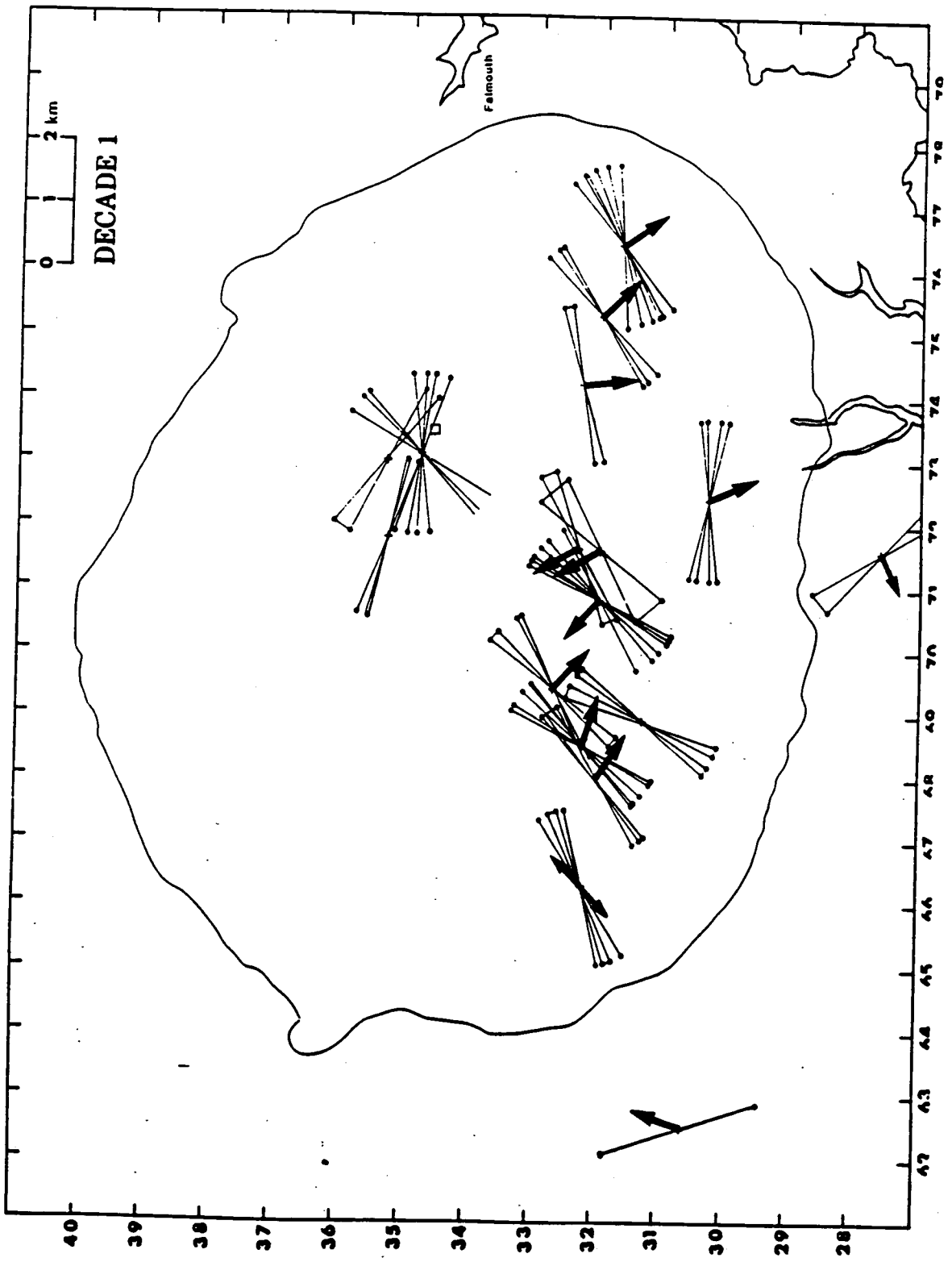

Figure 7.2a. Map of azimuths of maximum resistivity for Decade 1 and azimuths of the maximum response of the vertical magnetic field, again for Decade 1.

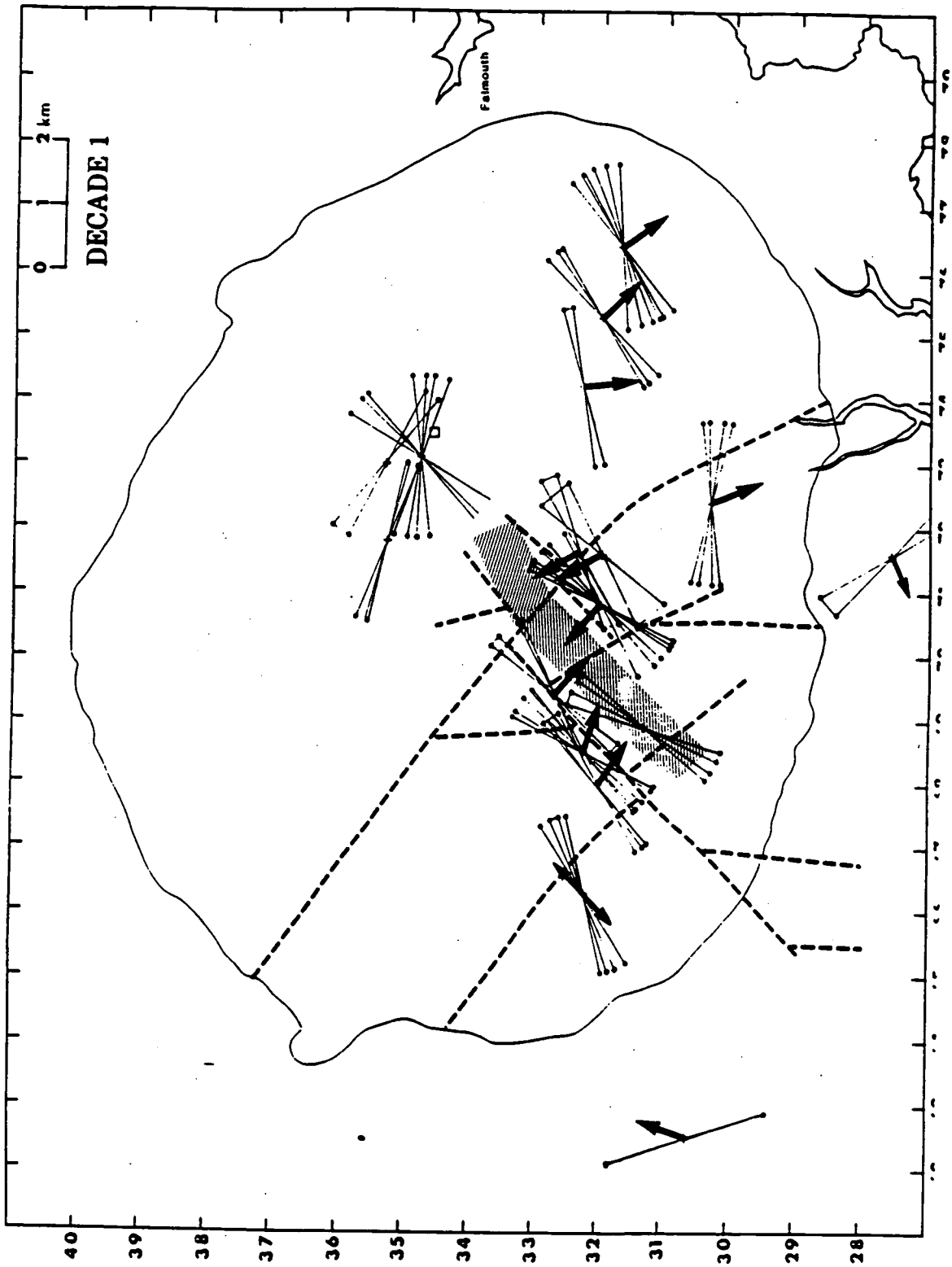

Figure 7.2b. Same information as in Figure 7.2a but includes lineations in the vicinity of the vertical field 'reversal' and indicates approximate location of a conductive zone (shaded).

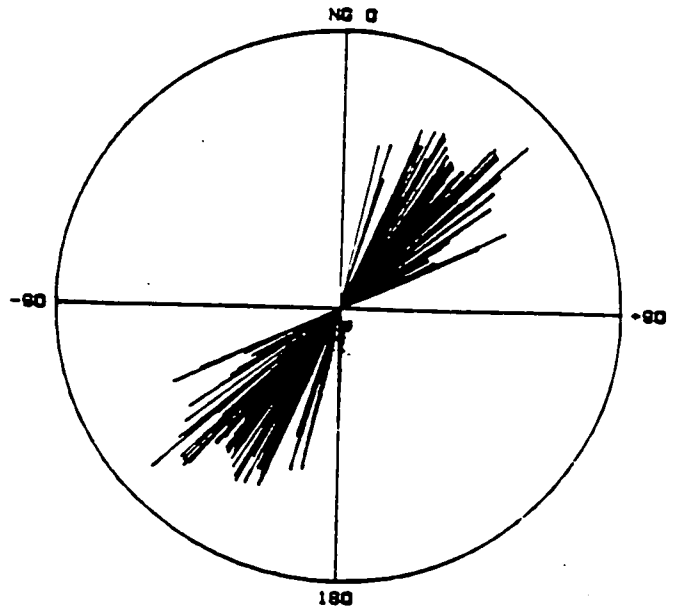

IDEC 4 VERTICAL FIELD TF AZIMUTHS <Ge> DIA 0.50

SITES 101-107

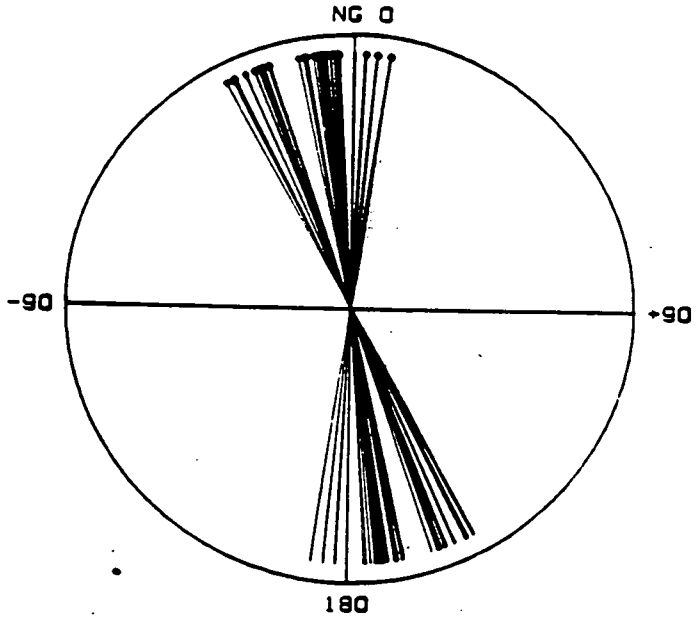

IDEC 4 MAXIMUM STATE TENSOR AZIMUTHS -E- FIELD <GE>

Figure 7.3. Low-frequency (Decade 4) azimuthal orientations of maximum response of vertical magnetic field and maximum resistivity. (a) sites 101-107 and (b) sites 109-112.

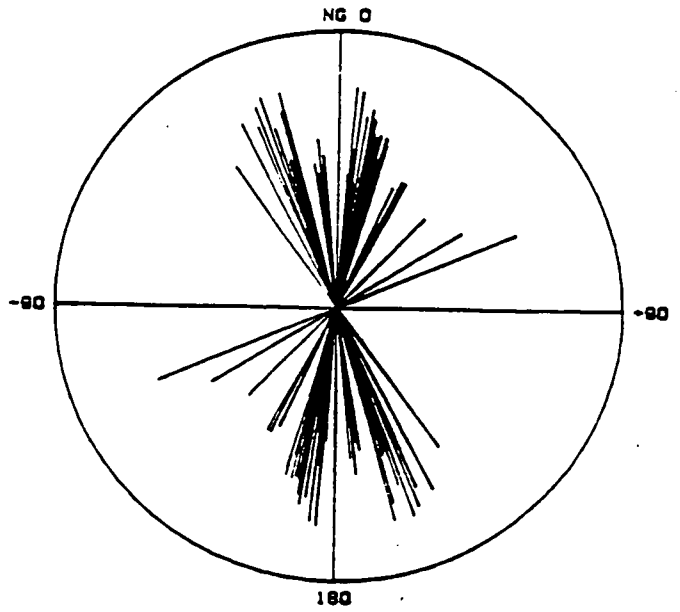

IDEC 4 VERTICAL FIELD TF AZIMUTHS <Ga> DIA 0.50

SITES 109-112

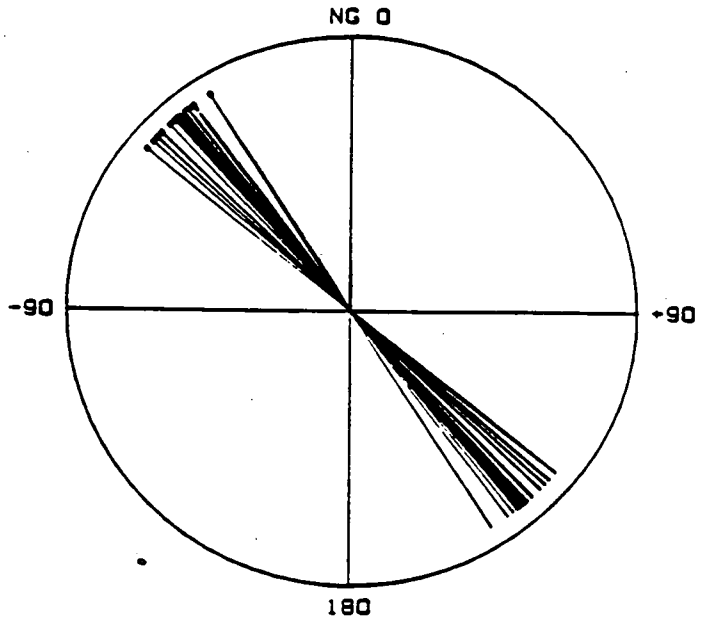

IDEC 4 MAXIMUM STATE TENSOR AZIMUTHS -E- FIELD <GE>

Figure 7.3. Low-frequency (Decade 4) azimuthal orientations of maximum response of vertical magnetic field and maximum resistivity. (a) sites 101-107 and (b) sites 109-112.

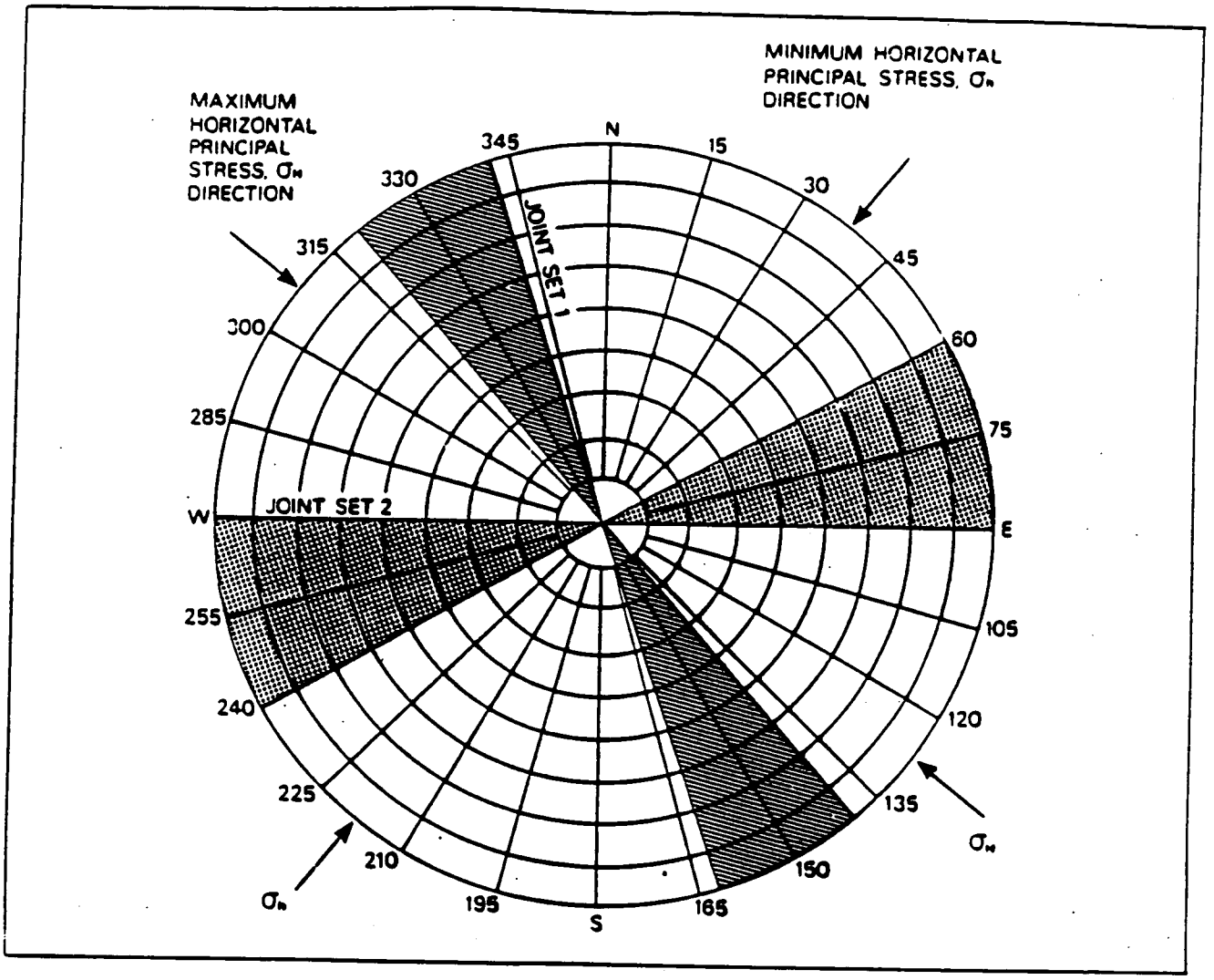

Figure 9.1. Directions of the two principal surface joint sets (JOINT SET 1 and JOINT SET 2, both shaded) and maximum and minimum principal horizontal stress directions (arrowed). From Green et al. (1987).

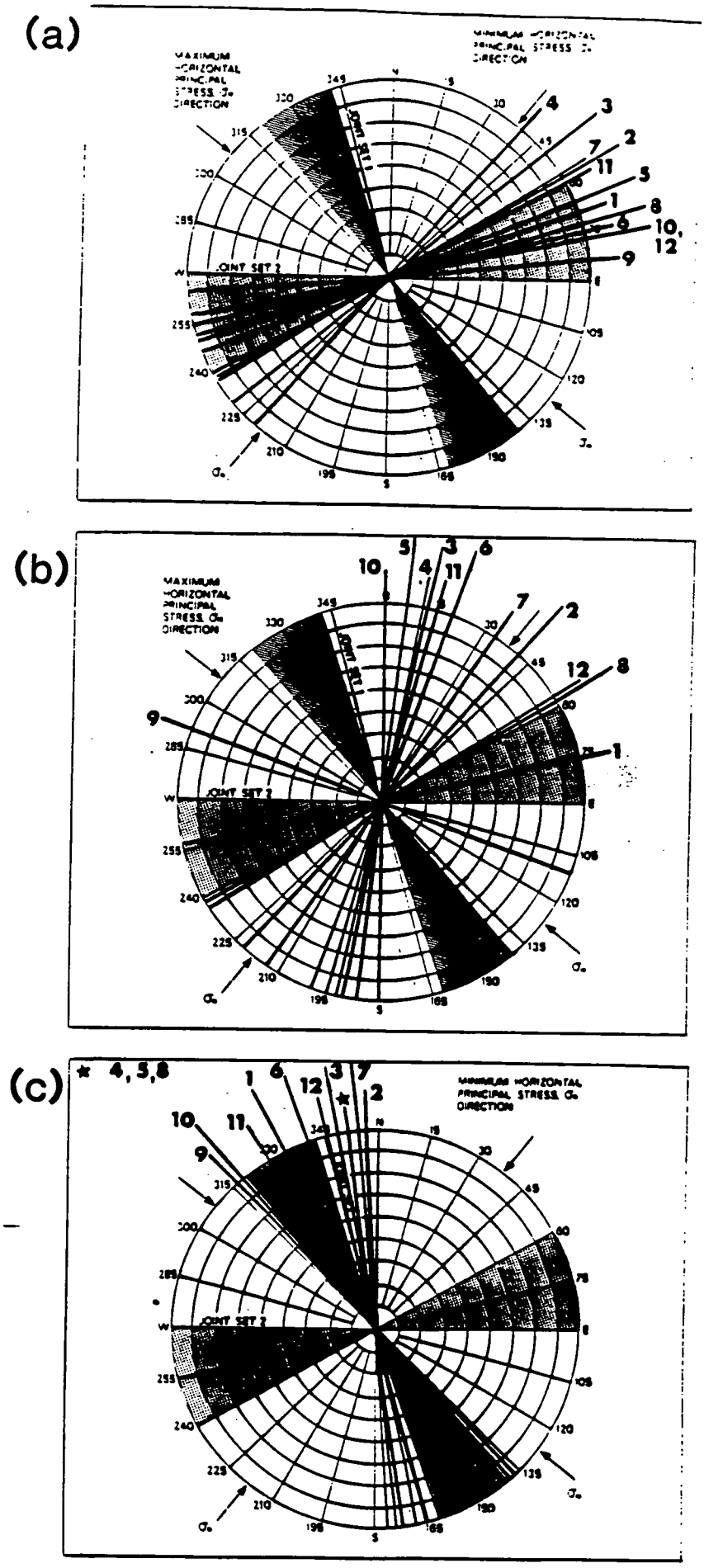

Figure 9.2. A comparison of the joint and stress directions (Fig. 9.1) with the azimuths of maximum resistivity for the twelve sites (101-112) on the main E-W profile. Site 1 = 101, Site 12 = 112 etc. (a) Penetration depths from 832 to 1686 m. Frequency = 89.5 Hz. (b) Penetration depths in the range 3 to 6 km. Frequency = 8.95 Hz. (c) Penetration depths greater than 25 km. Frequency = 0.089 Hz.

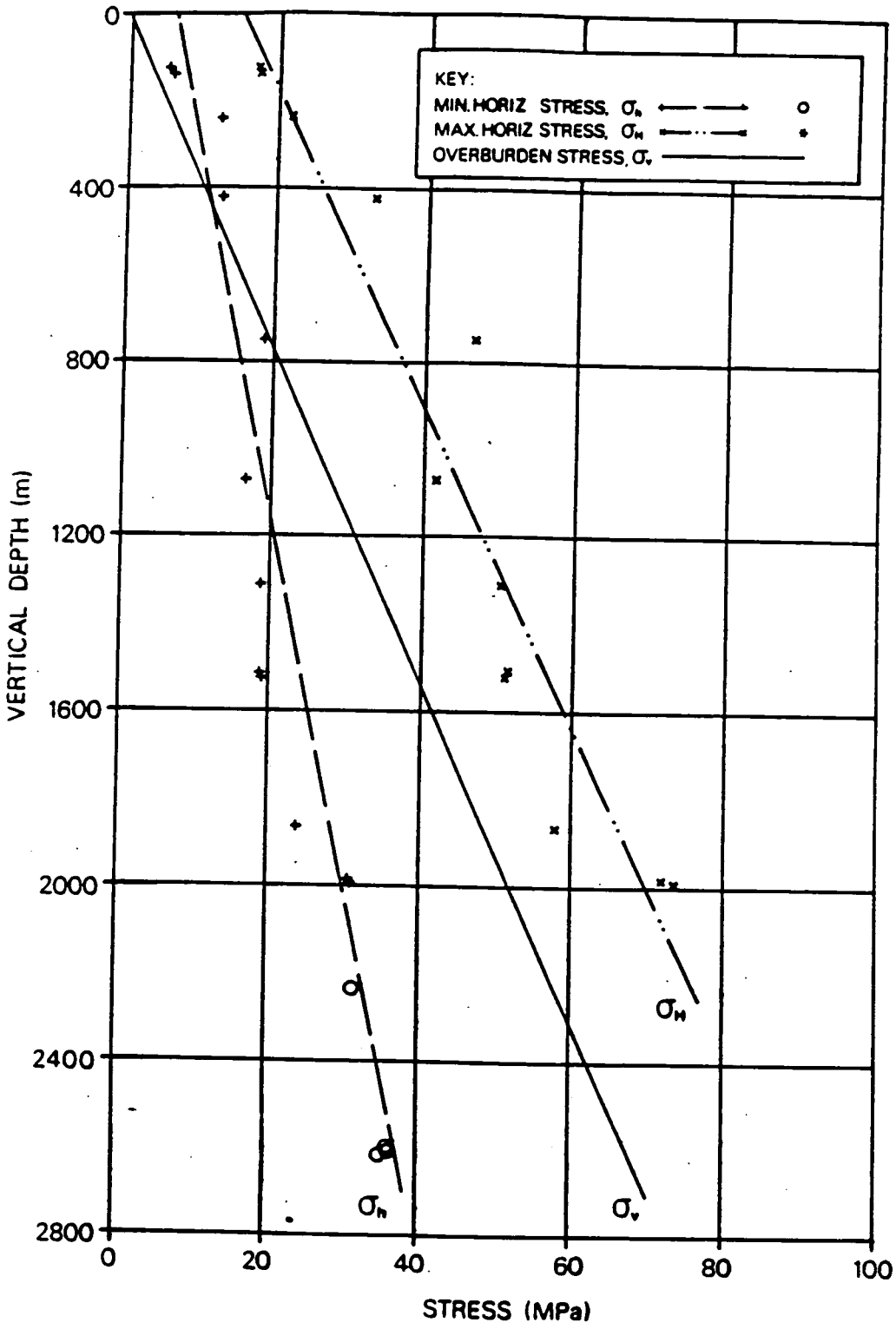

Figure 9.3. Inferred magnitudes of the three stress components as a function of depth. From Green et al. (1987).